

8.1 General

8.1.1 Hardware Return from Space

The low Earth orbit (LEO) environment is defined as that region of space between 200 and 1000 km (124 and 621 miles) above the Earth. It was reasonably well characterized in the 1950s, during the prelude to the race into space, by means of sounding rockets equipped with monitoring devices for recording air pressure, temperature, and gaseous composition. Many of the data obtained from those early space flights are suitably accurate for today's calculations and have been discussed in Chap. 2 and compiled into Table 2.3. In just one decade, the 1960s, human beings began to extend their physical boundaries by initially venturing into LEO and then progressing to explore the mountains and valleys of the Moon. The first human to orbit the Earth was cosmonaut Yuri Gagarin in the Vostok 1 spacecraft on the 12th April 1961. Since then, manned spaceflight included the Mercury (Atlas ELV) missions, the Gemini (Titan ELV) missions, and the Apollo (Saturn ELV) missions that gave 12 human beings the opportunity to walk on an extraterrestrial surface, with the first manned landed on the Moon in 1969 with Apollo 11, and the final Moon-landing in 1972 with Apollo 17. The 1970s saw the launch of several Salyut space stations and three Skylabs, followed in the 1980s and 90s with the Mir station, the Kvant module, and the many Space Shuttle launches (for the placement of satellites into orbit, ejection of probes into space, retrieval of spacecraft, and utilization of Spacelab which remained attached to the Shuttle's cargo bay). At the time of writing, it is the International Space Station (ISS) that continues to be the most newsworthy space activity. This is the biggest construction to fly in space and can be readily seen from the ground as it completes 16 orbits per day. Huge solar panels, totaling approximately one acre are attached to the central truss of ISS—the dimensions are equivalent to the length of a football field, the habitable volume is as large as a six-bedroom house and the total mass

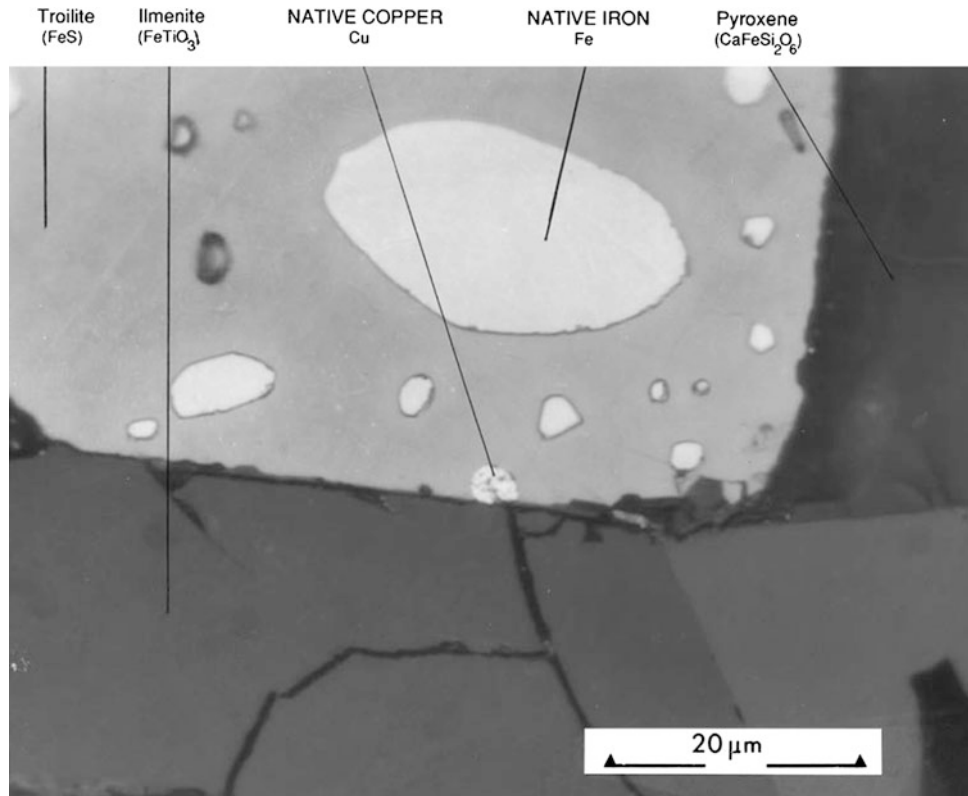
is just over 450 metric tons (tonnes). Awe-inspiring, as ISS was built by astronauts and cosmonauts, 216 have lived there, bringing each part of the construction from Earth by Shuttles and various other cargo-vehicles (2015 data).

The space missions referred to above have all involved the launch, exposure to space (in particular the LEO environment), and the final return of some form of space hardware to Earth. Once the mission tasks had been completed there was little reason to spend extra effort into performing post-space flight analyses of the materials used to construct the spacecraft. Some post-flight observations have been documented, such as those related to impacts by micrometeorites during the mission, the degradation of thermal control surfaces due to discoloration from exposure to ultraviolet radiation and, of most importance, the effectivity of the re-entry protective shield. However, the external surfaces of those spacecraft were constructed from materials that were little affected by the space environment, such as anodized aluminium alloys, titanium alloys, passivated stainless steels, and fused silica glass. The re-entry shields were either of the ablative type that burnt and shed material during their hypersonic velocity passage into the oxidizing atmosphere or, more recently, of the lightweight silicon-based ceramic tile-types which have a good resistance to high-temperature oxidation, air turbulence, and shock during descent.

8.1.2 Raw Materials from the Moon

The number of documented post-flight examinations of spacecraft materials are probably now equal to the several hundred papers in which the results of Moon-rock analyses were published since 1967. Although the scientific yields from the observations of the astronauts on early Apollo missions were of great importance, they were later overshadowed by the investigations of land-based scientists who studied the lunar samples. These studies included a determination of the abundances of all the elements, their

Fig. 8.1 Micrograph of Moon rock returned by US Apollo 11 astronauts, July 1969



isotopes, and the nature of their coexistence in the various phases making up the lunar material. The lunar samples brought back by the US (manned Apollo) and Soviet (Luna automated soil collection and return to Earth) space programmes revealed that the Moon's surface is rich in non-volatile, low atomic mass elements. Lunar rock and soil samples (termed "regolith") were distributed to laboratories worldwide for analysis. One particularly interesting rock was prepared by standard metallography and is shown in Fig. 8.1. This micrograph is typical of the Apollo 11 regolith in that it is basaltic and contains a large amount of ilmenite. The rock also contains phases of metallic iron and a small amount of metallic copper. Iron-nickel alloy, native iron and native copper have also been identified during quantitative optical and electron-probe studies of lunar samples at the Institute of Geological Sciences, London (Simpson and Bowie 1970). The location of metallic iron has been stated to bear a relationship to the lunar magnetic properties and many possible sources of this metal have been postulated (Adler 1988). It would appear that the existence of native copper, present as a small 4 μm diameter sphere in Fig. 8.1, is uncommon because chemical analyses of core samples, collected at any of the other eight Apollo sampling sites, showed that this metal is generally only present as a trace element in the order of 10 ppm. Oxygen is particularly abundant in the form of oxides of silicon, titanium, iron, and magnesium at the lunar mare site visited by Apollo 11. By

comparison, the rocks retrieved from the lunar highlands by later Apollo spacecraft were relatively enriched in oxides of aluminium and calcium (with low Mg and Fe contents).

The use of the Moon and lunar materials has often been suggested by scientists as the stepping-stone into an industrialization of space. Certainly there exists a wealth of minerals, a strategic location, and a reduced gravitational force. It should be possible to manufacture a range of structural materials on the lunar surface; oxygen in the form of oxide is present, but three of the most vital elements were thought missing: carbon, nitrogen, and hydrogen, and without these there can be no indigenous life-support systems. In recent years scientists have suggested that water ice and other frozen gasses (or volatiles) may be trapped on the perpetually shaded polar regions of the Moon. If long-term support is to be given to human activities on the Moon or Mars it seems essential that a base will have to be built on the Moon's surface. Both NASA (Mueller 2014, 2015) and ESA (Ceccanti 2010) have considered the requirements for a lunar base to house people and offer protection from meteorites, solar- and gamma-radiation and high temperature fluctuations—several attempts on Earth to construct dwellings from lunar regolith simulant have been successful (see also Sect. 8.2.2). The ultimate success of a permanent lunar base is expected to depend on how man uses the in situ resources. If it is possible to manufacture propellants on the Moon it will relieve astronauts of the need to transport

'return propellants'. The lunar surface appears to contain 45 weight percent oxygen, most in the form of silicates and other mixed metal oxides. With the use of solar, nuclear power and focused mirrors, it has been proposed (Hepp 1999) that regolith can be heated and modified to release oxygen and precipitate metals and alloys of aluminium, silicon, iron and titanium. These metallic powders would then be burnt in a combustion chamber and the simultaneous release of hot gasses gas through a nozzle would provide a form of propulsion!

8.1.3 Recent Investigations Using Retrieved Materials

The ISS was gradually constructed over a period of 12 years. This started in 1998 when the first module, Zarya, built by Russia, was launched in 1998. This permanent space station in LEO has been continuously occupied since 2000. The present architecture is seen in Fig. 3.1b. Plans are to prepare the station for commercial use and two international docking adaptors will be added to the structure and utilize the station until at least 2020. Alongside the operation of ISS has been a continual series of materials tests, such as the MISSE experiments, where samples of a wide range of material-types and components are exposed to the harsh environment of space for long periods of time. The data that has been generated from tests performed on materials that were retrieved from long-term space satellite experiments, from the return of functioning space hardware, and from relatively short-term Space Shuttle flights is the subject of many space symposia. Some data have been generated from ground tests in which attempts are made to replicate the LEO environment in laboratory chambers. The majority of the materials exposure data has originated from space missions such as Salyut-6 (5-year exposures), Salyut-7 (9-year exposures), Mir station (experiments of 3-year duration), the Long Duration Exposure Facility (LDEF) launched and retrieved by Space Shuttles (STS flights) after nearly six years in LEO, and the European Retrievable Carrier (EUR-ECA), similarly launched and collected after nearly one year in orbit. Short-term materials exposures were made on STS-5, STS-8, and STS-46 (for instance, the 58 h Evaluation of Oxygen Interactions with Materials III (EOIM-III) flight experiments). Retrieval of the Solar Max spacecraft provided some data, as did the post-flight investigations performed on the Hubble Space Telescope solar array that was retrieved after about four years in LEO (during the first HST Servicing Mission in December 1993; the second service mission took place over a 10-day period in 1997). The most recent test exposures include the European MEDET rig and the previously stated MISSE project; all are currently being examined in a 1500 sample test programme.

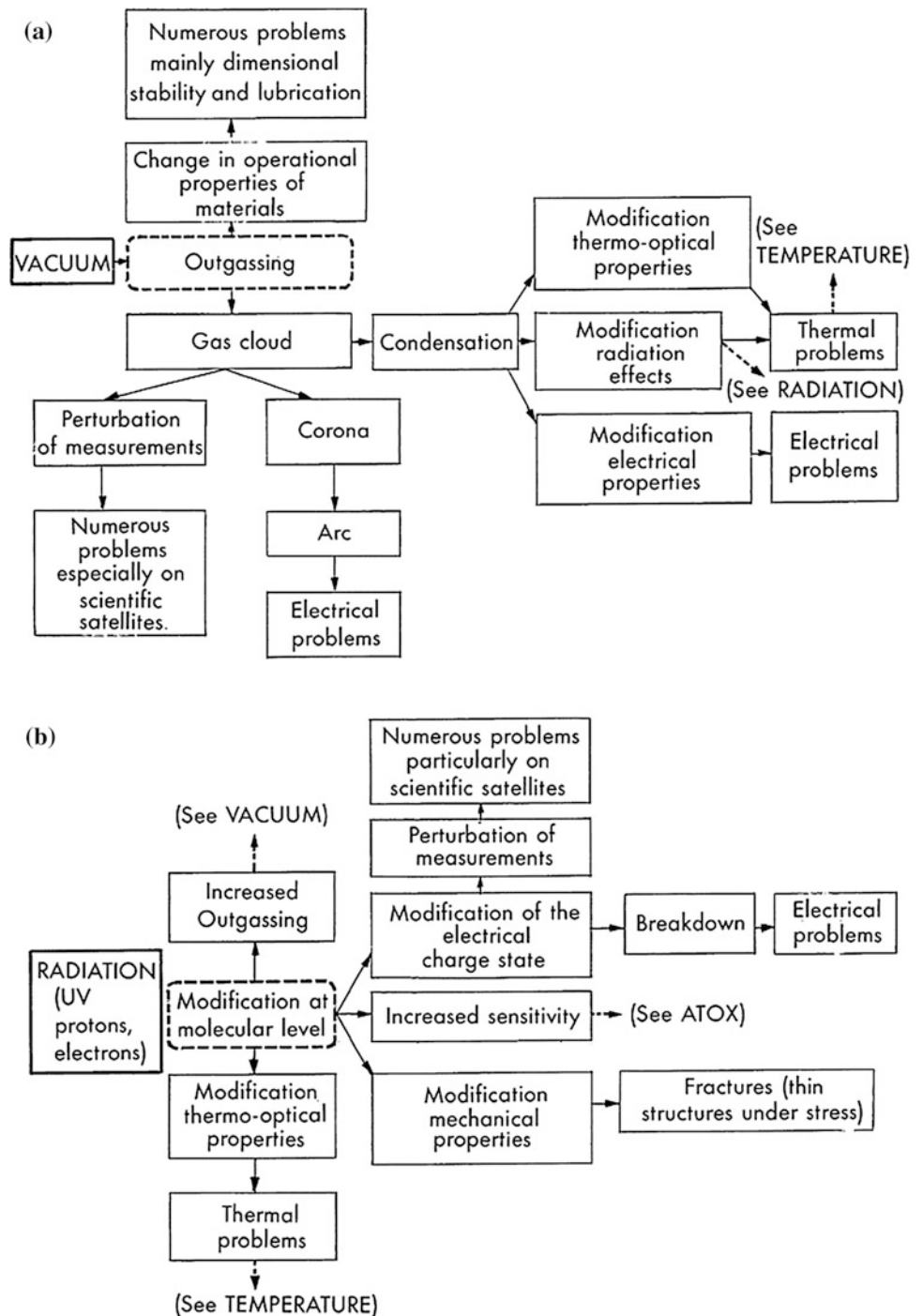
The purpose of the following sections to this chapter are to present some of the findings from recent experiments and observations of returned hardware. As well as recording some predictable modes of degradation, data has also identified unusual phenomena likely to either enhance or reduce the durability of spacecraft mechanisms, structures, and their materials. Some end-of-life properties have been established and these are of great importance to design engineers. Only those references considered to be of major importance will be cited by the author. The remaining information either originates from his own work, or has been recorded at early specialist meetings on space materials (Levine 1993, Flury 1993, Anon 1994, Guyenne 1994, Gerlach 1995). More recently, some data has been published concerning the MEDET results (Tighe 2010). The following sections will also describe property changes to materials brought about by their exposure to LEO environments. The main effects are due to each material's exposure to vacuum, radiation, temperature cycling, micrometeoroids and space debris, atomic oxygen, the re-entry environment, and operation within a manned volume. The space environment effects are illustrated by the block diagrams in each section. There can be a strong synergistic influence between these effects as inferred by the diagrams (Dauphin et al. 1991). This information will be of interest to those engineers responsible for scrutinizing the materials selection process for future missions, some of which are destined for relatively low orbiting altitudes (~ 350 km) in high densities of atomic oxygen.

8.2 Space Environmental Effects from Vacuum and Radiation

8.2.1 Organic Materials and Lubricants

Screening tests are continually performed during the selection of organic materials for space applications. Approximately 100,000 test results are available from NASA and ESA sources based on the test method specified in ASTM E-595. The provision is that materials, when tested in vacuum at 125 °C for 24 h, shall not have a recovered mass loss (RML) greater than 1 %, or a collected volatile condensed material (CVCM) content of more than 0.1 %. This, and other test methods for organic materials, have been described in Sect. 2.5. Some examples were given for lubricants in Table 5.2. If these requirements are neglected there is a danger that spacecraft will become contaminated by the outgassing species (the effect of outgassing/condensation can be seen in Fig. 5.12). Vacuum exists everywhere in space except in pressurized modules. Vacuum may change from 10^{-14} torr in free space to 10^{-4} or 10^{-3} torr in poorly vented spacecraft subsystems. The chain of dangers that result from outgassing products is depicted in Fig. 8.2; gas

Fig. 8.2 Space environment effects: **a** vacuum; **b** radiation

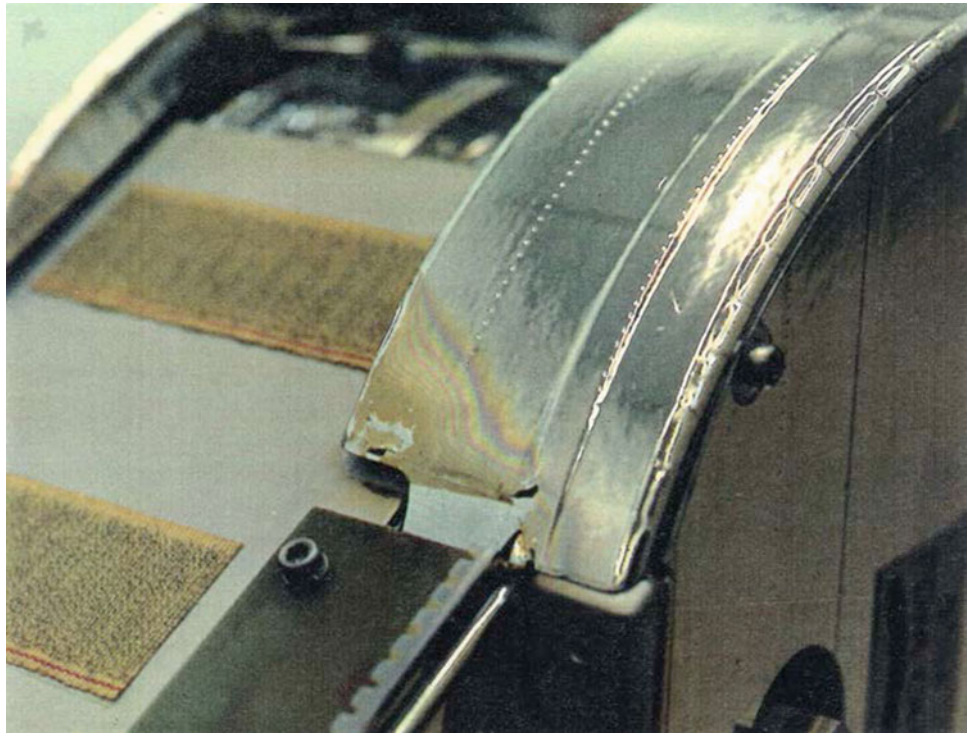


clouds can produce corona and arcing, or may condense onto surfaces and so modify them to produce thermal and electrical problems.

A major finding from the recent post-flight materials experiments concerns the use of silicone products that were previously considered to have been suitably screened by the outgassing test. Another, concerns the 24 h vacuum bake at 125 °C that has become a standard practice in history for cleaning polished mirrors and other hardware, so benignly

removing molecular contamination which would otherwise have migrated to contaminate sensitive spacecraft surfaces when in orbit. Cleaned hardware is best maintained under vacuum or, at least, sealed in appropriate bagging material, preferably under an ultrapure gas such as nitrogen. A comparison of identically produced samples that were either pre-cleaned by the standard practice, or exposed to the vacuum of space has been performed. The results found that the ground-based material conditioning process “125 °C

Fig. 8.3 Thermal cover showing ‘fringe pattern’ of condensed contaminant on exposed Kapton tape (returned from Hubble Space Telescope)



vacuum bake for 24 h” is equivalent to holding an article in a space environment at an ambient temperature of 20 °C and a pressure of 10^{-6} torr for a period of one year. There are two provisos—that this practice does not hold true for either silicone products or Teflon FEP materials. Recent tests with approved silicone products caused outgassing and contamination in LEO. Even very thin layers of contaminant (about 400 Å), together with the presence of ultraviolet (UV) radiation and atomic oxygen, caused significant degradation of thermal control surfaces (Babel et al. 1994). In a similar manner, Teflon FEP can degrade with the formation of a volatile product that is mainly perfluorocarbon, but can include chemically active species containing fluorine, and these have been seen to chemically etch the surfaces of polished metals and glass (van Eesbeek et al. 1994). Teflon FEP originating from samples mounted on LDEF for 5.8 years, was compared to samples of the same materials exposed to LEO on the Hubble Space Telescope (HST) for both 3.6 and 8.25 years (periods for the service missions). All AO (atomic oxygen) exposed samples became mechanically embrittled and had lower strength properties when compared to reference ground-stored sheet (Fink 2006). The HST solar array bellows and the multilayer insulation (MLI) items were severely damaged and cracked, being worse for the longer exposure. Samples taken from LDEF material exposed to the RAM direction (AO: 8.17×10^{21} atoms/cm²) became more damaged than samples in the WAKE direction (AO: 9.32×10^4 atoms/cm²). In general Teflon FEP is not used on the ‘external’ surfaces of

spacecraft with the exception of its application as an insulation material for wires and cables.

Further inspections of the returned HST solar array revealed several surfaces to have been contaminated by the condensation of outgassing products. Figure 8.3 is included, as it highlights a condensation layer having a variable thickness and is clearer to photograph than surfaces that have been uniformly discoloured. Silicone contamination has been identified on the HST samples, by analysis of collected spectra, to be the main contaminant along with dicyandiamide, which is an outgassing produce from CFRP materials. All items manufactured from Delrin material, namely the primary deployment cable and the ‘boom end’ cotton reels, changed from a white colour to yellow-brown on their sun-pointing sides. All surfaces covered with the atomic oxygen protective coatings (CV1144-1, DC93500, and RTV S691) became darkened in colour from straw to dark brown—the more exposure to the Sun’s radiation the darker the colour (see Fig. 8.4). They are expected to cause an increase in temperature at these locations.

None of the traditional lubricants based on vacuum-distilled silicone oils and greases were seen to degrade during exposure to service life in space. Some were noted to have ‘crept’ from bearing races onto adjoining surfaces. Rotating surfaces that had been lubricated with thin lead coatings survived their designed lives.

Concern was raised when three critical pump motors failed in close succession following five months of successful operation in LEO. On returning to Earth, the motors

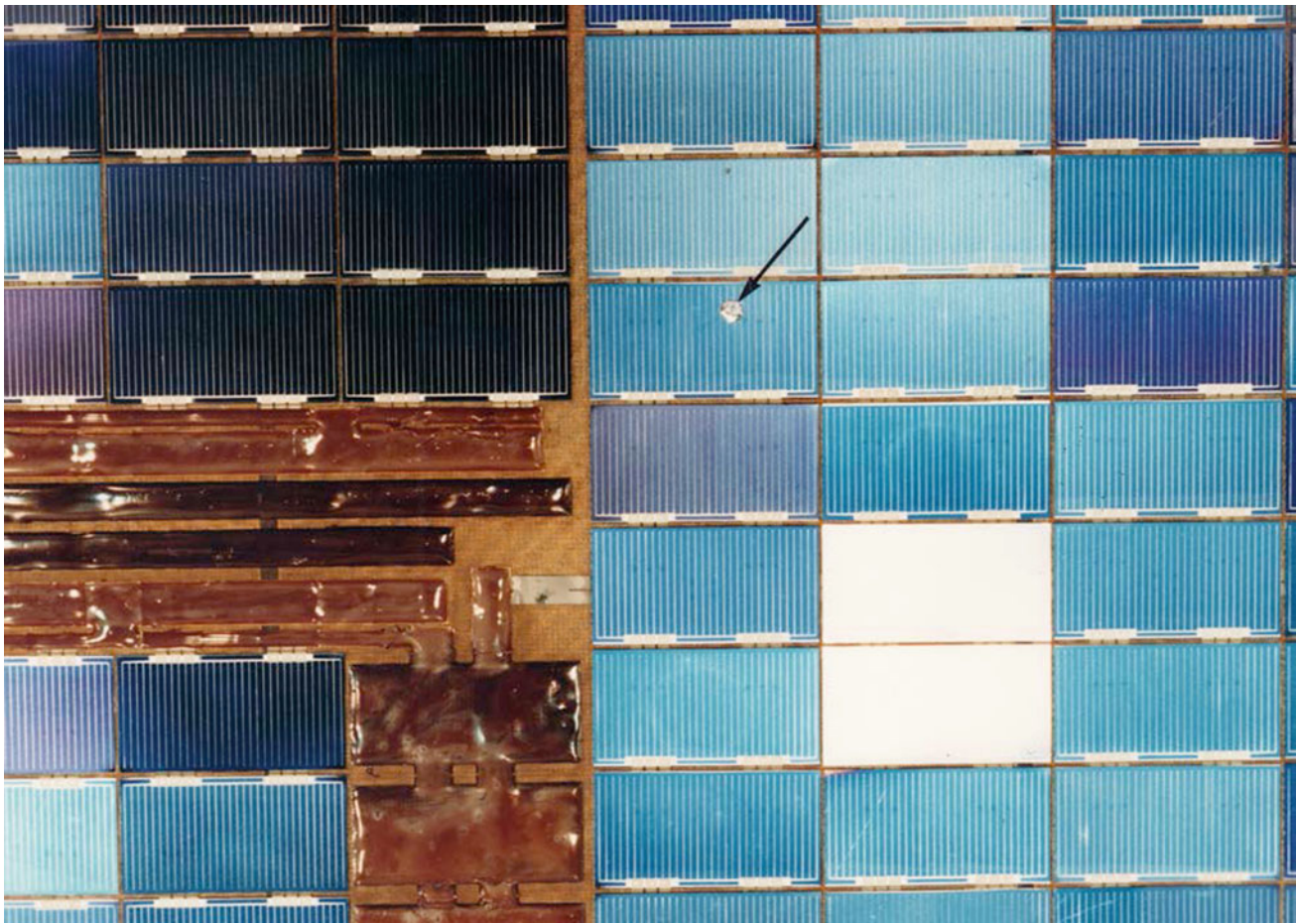


Fig. 8.4 Part of the HST solar array showing the ATOX protection silicone coatings to have become darkened after exposure to the Sun's radiation. One micrometeoroid impact is also visible (*arrowed*) (see also Fig. 4.63)

were stripped down to reveal their brushes, commutators, and armatures. Large quantities of brush debris were noted—associated with the full wear-out of the graphite brush lengths. The small stubs of brush material that remained were analysed and found to contain only carbon (graphite) and copper with no additional elements. The absence of any so-called adjuvant materials within the microstructure of these flight brushes were extremely important. It is known that adjuvants such as molybdenum disulphide (MoS_2) or barium fluoride are essential components for brushes needing to operate under vacuum. Investigations found that these motors had been qualification tested prior to launch in laboratory air. This air contained moisture, an essential ingredient for graphite brushes that enables them to run for extensive periods with very little friction and wear. The flight brushes had absorbed sufficient amounts of moisture so that they behaved correctly when operated for a short period in dry nitrogen, and correctly when launched into

space. However, once the water content of the brushes had diminished sufficiently by outgassing under vacuum, the friction and wear rates would be markedly increased, so producing these early pump motor failures. Some alternative brush materials have been described in Sect. 4.8.2, but it is essential to perform any qualification tests in vacuum rather than dry nitrogen.

More recently with respect to tribology, tungsten carbide alloyed with MoS_x thin films (deposited by magnetron sputtering) has been prepared and tested under vacuum and LEO. Ball-on-disc samples were evaluated on the ESA Tribolab (installed in the European Technology Exposure Facility fixed to the Columbus module of ISS). These tests (Brizuela 2009) have indicated $\text{WC} + \text{MoS}_x$ to be a novel, highly suitable material for operation in LEO and comparable to conventional MoS_2 films. Very low extraterrestrial friction levels of 0.04 were reached during more than 1 million wear cycles on the ball-on-disc set-up and loading at 0.75 GPa.

Table 8.1 Components of the natural space radiation environment

<i>Solar-particle events</i>
Occur sporadically; not predictable
Energetic protons and alpha particles
Solar-flare events may last for four or more days
Dose very dependent on orbital altitude and amount of spacecraft shielding material
Presently under study by the SOHO spacecraft
<i>Galactic cosmic rays</i>
Typically 85 % protons, 13 % alpha particles, 2 % heavier nuclei
Integrated yearly fluence:
1×10^8 protons/cm ² (approximately)
Integrated yearly radiation dose:
4–10 rads (approximately)
<i>Geomagnetically trapped radiation</i>
Primary electrons and protons
Radiation dose depends on orbital altitude
Manned flights below 300 km altitude avoid Van Allen belts

For solar particle radiation see Table 2.4

8.2.2 Radiation Effects

The term radiation (Table 8.1) covers a wide range of emissions of energy from the Sun in the form of electromagnetic waves (the range passes from X-rays to UV and visible light, to radiowaves) and particles which are trapped in the Van Allen belts (protons and electrons) that surround parts of the Earth. A second region that traps highly charged particles band is known as the South Atlantic Anomaly, its location is seen on Fig. 8.5, and this presents a significant hazard to spacecraft in low altitude, low inclination orbits (Mikaelian 2001). Other particles originate from deep space, such as cosmic rays, and reach the Earth from all directions, with high energy and great penetrative power. Radiation at the levels existing in space (generally about 10^7 rads per year) do not modify the bulk properties of metals. Even the largest doses of radiation that occur in the Van Allen belt have no effects on metals. It is only the combination of contamination layers together with radiation (see Fig. 8.2b) that can severely change the surface properties of metals and this may lead to an increase in solar absorptance and a reduced hemispherical emittance. Materials such as coatings and paints are progressively damaged by solar radiation becoming embrittled by both particle and UV radiation (Dauphin 1993). White paints were modified to have more absorptive properties

whilst black paints tended to bleach. The white paints with an inorganic base and a silicate binder were found to be more stable than any of the organic-based paints. Spacecraft adhesives, thermosetting resins, and lubricants are unaffected by the low dosage of radiation from space, and these are usually well protected by metallic foils or are present within electronic black boxes. Some inorganic glasses are quickly damaged by radiation, and even as little as 10^3 rad can cause a loss of transparency to some wavelength ranges (Dauphin 1993). Plastic glasses and optically transparent silicone coatings are also damaged by a general ‘yellowing’ during exposure to solar radiation as seen in Fig. 8.4.

Microelectronic semiconductors are also damaged by solar particle radiation. These are usually split into two categories: cumulative effects due to prolonged exposure to radiation, and single-event effects caused by transient high levels of cosmic or high energy proton exposure that can lead to worst-case damage to spacecraft electronics.

For instance, the thin gate oxide in metal-oxide-semiconductor devices (e.g. MOSFETs) is degraded to cause leakage currents. As the line width of conductors on such devices becomes smaller, so the sensitivity of the various semiconductor Si–SiO₂ interfaces to radiation becomes greater. The ionizing radiation creates electron/hole pairs and charging of the oxide to produce leakage current perturbations. Irradiation will also cause deep-level defects in the bulk silicon lattice. This can cause gain degradation of an npn or pnp transistor, or increased leakage current in a diode. Experience has shown that LEO spacecraft have not often suffered from electronic component damage due to radiation. However, damage does occur when space vehicles travel through the heart of radiation belts as would be the case for spacecraft in low Earth polar orbit, or prolonged periods in geostationary orbit. Here, ‘radiation hardening’ is required by means of altering the processing steps during device manufacture or providing countermeasures such as physical shields or foils around the packaged device. Detailed handbooks have been compiled by Homes-Siedle and Adams (1993) and Mikaelian (2001) to cover the effects of radiation environments on spacecraft electronic equipment, their components, and materials. It is noted that in recent years researchers have been searching for novel ways to avoid radiation damage, either integrating functions into a single chip or ASIC for better performance, or by enhanced radiation shielding with tantalum and tungsten ‘spot shields’. These metallic elements are about six times the density of aluminium and they allow thinner shields to be made, thus only incurring a small weight penalty (Maurer 2008).

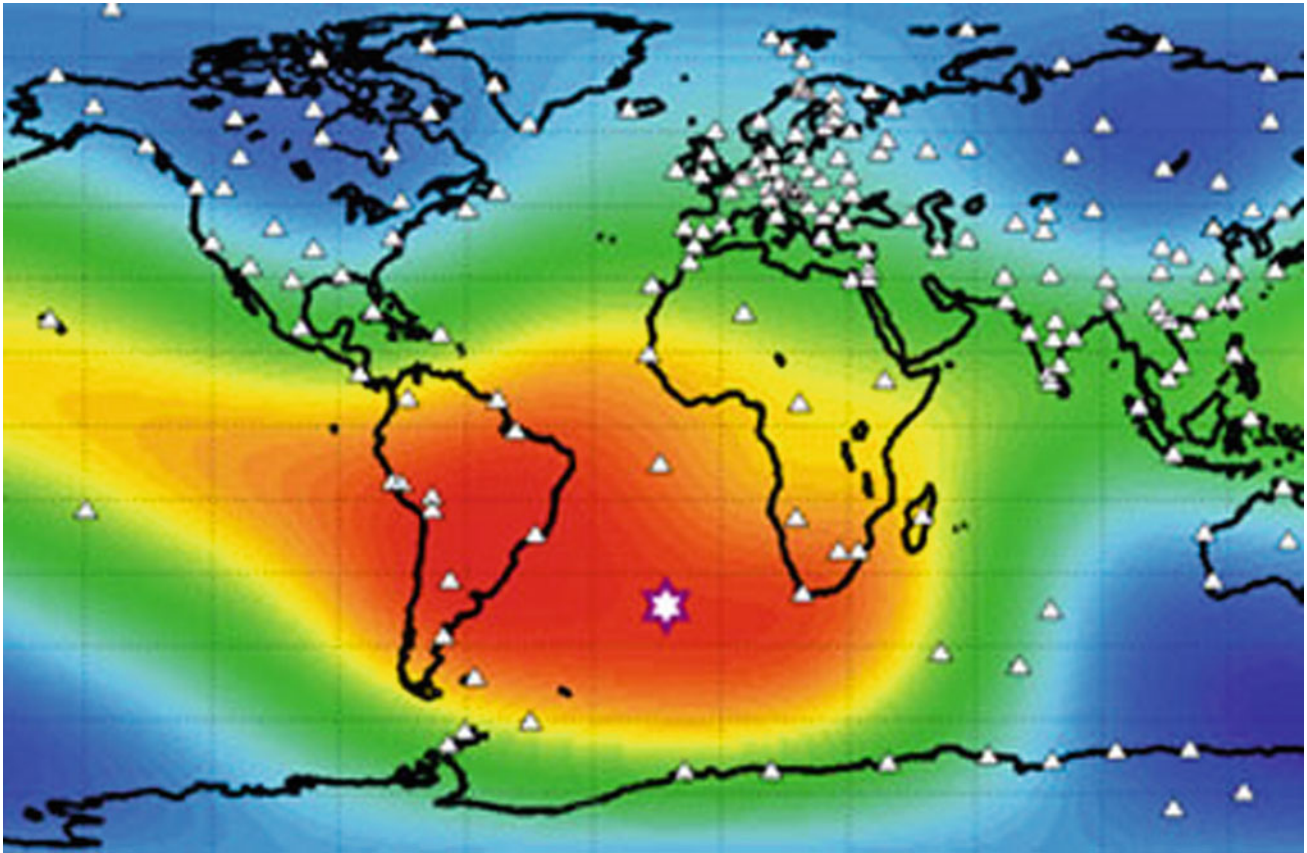


Fig. 8.5 Tristan da Cunha is located in the middle of the South Atlantic Anomaly, which is also where the Earth's magnetic field shows an anomalous dip. Courtesy of the Danish National Space Centre

8.2.3 Effects of Vacuum on Metals

As already alluded to in the previous sections, there have been no instances of degradation to metallic materials due to the combined effects of vacuum and radiation even when returned to Earth from the longest exposures to LEO. This is because the selection process avoided the use of metals known to produce problems such as sublimation (e.g. for cadmium and zinc), whisker growths (tin and zinc), or loss of hermeticity for pressurized items, such as battery cells, hydrazine fuel tanks, and the like. The problem with silver was related to atomic oxygen, which will be discussed in Sect. 8.5.

One problem that did come to light, which resulted from a poor electrical design, was the major failure of one of the HST solar array drive electronic (SADE) systems after three years of satisfactory operation. At the moment the solar array position data was lost, the drive electronics was automatically switched off. A redundant unit was powered up soon after this event for the subsequent eight-month period up to the date of the HST service mission. As a consequence from

on-ground studies of the problem it was concluded that the failure was due to overheating of one of the SADE's assembled printed circuit boards (PCBs). A replacement model was built in which two power transistor devices were physically removed from the circuit and mounted via heat-sink caps onto the internal metallic structure of the SADE (Haines et al. 1995). This modification resulted in a device junction-to-structure thermal resistance of 30 °C per watt and ensured that even under the worst case conditions, the maximum transistor junction temperature would be less than 85 °C.

The SADE exchange activities on the first HST servicing mission were performed at night and under poor lighting conditions by astronauts Story Musgrave and Jeff Hoffman. Light from Musgrave's helmet light was used to illuminate the SADE system and during one of the most difficult EVA (extra-vehicular activity) tasks of the mission, the defective SADE was removed and replaced (Haines et al. 1995).

Electrical tests and visual inspections were performed on the defective PCB after it had been returned to Earth.

Following removal of the equipment's cover, a few minute spheres of solder alloy were seen attached to the inside surface of the lid. Subsequent inspections revealed much discoloration of the Solithane conformal coating in the vicinity of the two previously suspected power transistors. Electrical tests were made. The electronic unit had a below nominal power consumption, solar array position data were not available, and no smoke was seen to emanate from the suspected fault area. Further disassembly was performed and photographs made of the charred and overheated power transistors (see Fig. 8.6a). Inspection of the diodes adjacent to the charred site showed that they had also overheated as their solder joints had remelted and both the conformal coating and the epoxy top-coat of the circuit board had been completely evaporated away (Figs. 8.6, 8.7 and 8.8) to expose a region of glass-fibre weave (Adams 1994).

The cause of the SADE failure is thought to have resulted from the inadequate thermal management of the defective PCB assembly. Testing on the ground, in air, had not caused any pre-flight failures because the area surrounding the two power transistors could be kept below a critical temperature by means of heat lost by thermal conduction through the board and heat lost by thermal convection through the laboratory air. Under spacecraft conditions, the operating environment of vacuum excluded convection as a means of cooling and, after a period of high-temperature operation, the transistor solder joints melted (above 183 °C), so producing the final failure. By modifying the circuit such that both power transistors were physically attached to the metallic frame of the box, additional conductive heat loss was made possible and, to date, the present HST SADE unit is operating perfectly.

8.3 Temperature Cycling

The effects of temperature on spacecraft materials are depicted in Fig. 8.9a. The main input is from the Sun, sometimes reflected by a planet, and on output (cooling) by emission to the immense sink of deep black space. Temperature excursions are also generated by the operational mode of the spacecraft, from high-power electrical systems, and by the release of energy (exothermic reactions) during the consumption of liquid fuels. Local thermal cycling is caused by the expenditure of electrical power as devices such as travelling wave tubes are operated and then switched off (power cycling). The main overall thermal cycling of a spacecraft is experienced as it repeatedly passes from sunlight into eclipse during the course of an orbit. The solar array of the HST is subjected to 6000 thermal cycles per year between the temperatures -113 and $+95$ °C.

Little space will be devoted to temperature effects and thermal cycling in this section, as much has been written in this book to cover the topics of sublimation, thermal fatigue, and the importance of matching adjoining materials so that they will have similar coefficients of expansion. The very gradual thermal fatigue degradation of the HST solar array cell-to-interconnector weldments (only made visible by SLAM investigations) were described in Sect. 4.14. Distortion of the HST solar array due to differential heating and expansion rates were described in Sect. 5.17, but apart from this major defect, the remaining materials compatibility on the array seem to be good and the complete spacecraft will be flightworthy until its successor, the James Webb Telescope will be launched and become operational in 2017.

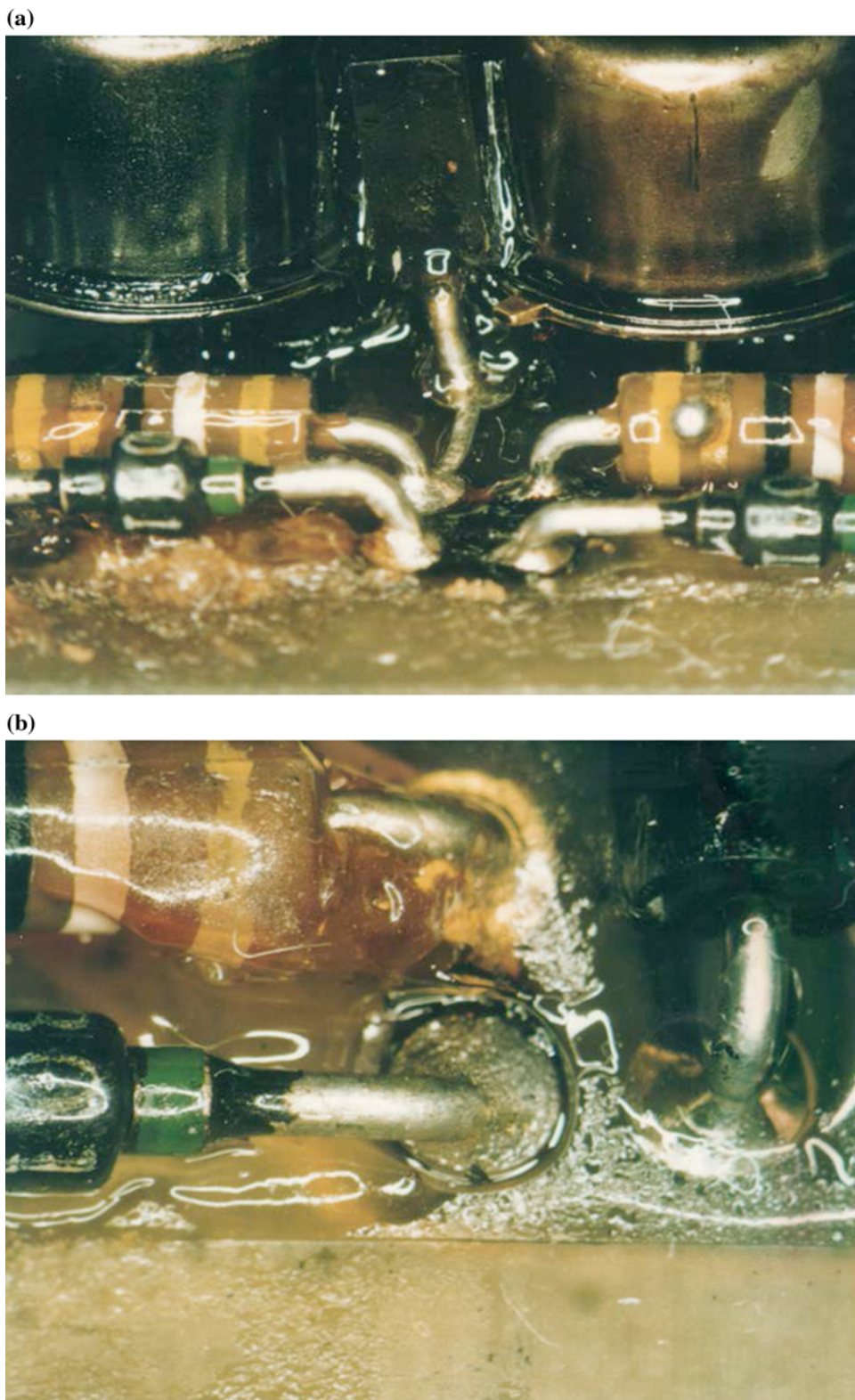
One of the most severely thermal-cycled solder joints to have been returned from space is shown in Figs. 8.10. This joint was one of several that existed on the HST array's so-called tag board. All survived 21,000 thermal cycles. The solder fillet has seen some stress due to the large thermal expansion coefficient of the FR4-type PCB in its z -direction (see also Chap. 6). Thermal fatigue is induced by 2.1 μ m mismatch between the board's glass-fibre weave/epoxy matrix and the brass terminal pin. This has exceeded the yield strength of the solder alloy during thermal cycling, causing the observed 'orange peel' effect on the surface of these solder fillets (Fig. 8.10a), but when microsectioned, it is clear that the integrity of the interconnections has remained intact (Fig. 8.10b, c).

8.4 Micrometeoroids and Debris

8.4.1 General

Micrometeoroids and cosmic dust are natural, hypervelocity particles that originate from comets, collisions between asteroids, and interstellar material. All sizes of these particles are of importance to spacecraft, but those most likely to cause damage, owing to their statistical distribution, range in diameter from 1 μ m to 5 mm. Before the space age began, this was the only particle population surrounding the Earth and passing through her atmosphere. Since the 1950s, debris from man's activities in space has accumulated across the skies. Space debris includes satellites and rocket upper stages that have completed their mission, together with thousands of smaller particles generated by explosions in space. Since the launch of Sputnik in 1957, more than 4600 launches have placed some 6000 satellites into orbit. Nearly 2200 remain in orbit, of which 450 are still functional. This means 80 % of space objects are uncontrolled debris.

Fig. 8.6 Visual appearance of post-flight Hubble Space Telescope's SADE failed electronic circuit board. **a** View showing the two transistors, in the background, detailing the discoloration of the Solithane coating on the component bodies. **b** View showing a joint on a diode, detailing the melting of the coating causing it to draw away from the joint. Other areas of this pcb assembly are seen in Figs. 8.7 and 8.8



Most of the debris exists in low orbits and is removed by the natural cleaning process of being slowed down by atmospheric drag and then burning up by the effects of air friction. Debris above 1000 km is only marginally subjected to

atmospheric drag and consequently may remain in orbit for thousands of years. Numerous debris removal concepts have been proposed, from electromagnetic ones to surrounding the object in foam and relying on the enlarged area-to-mass

Fig. 8.7 View showing a solder sphere attached to a resistor adjacent to one of the diodes

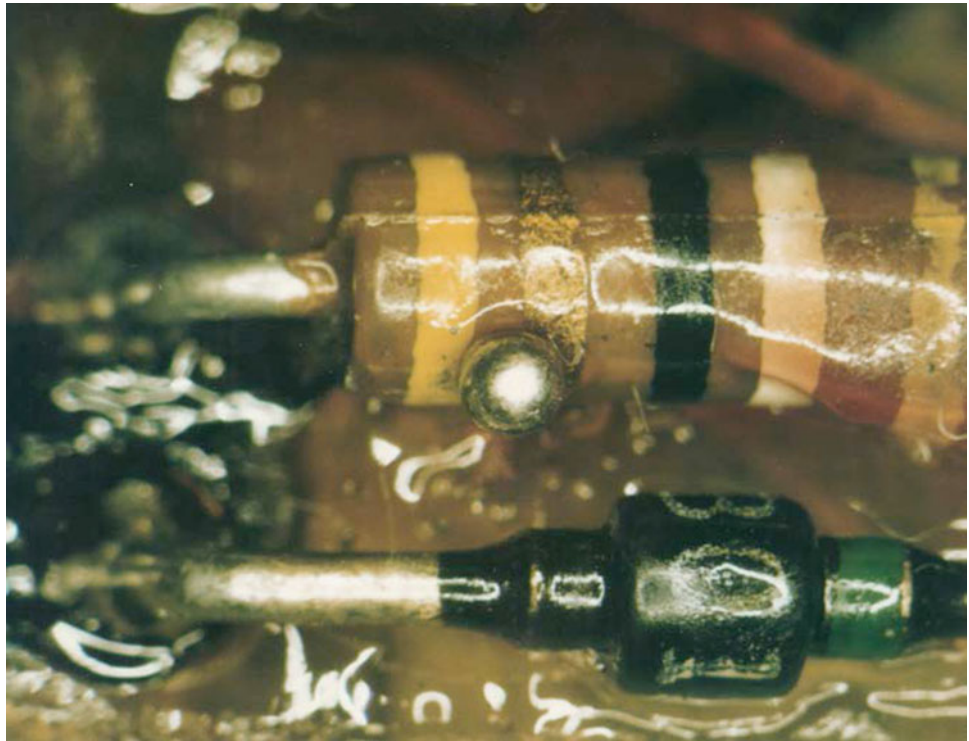
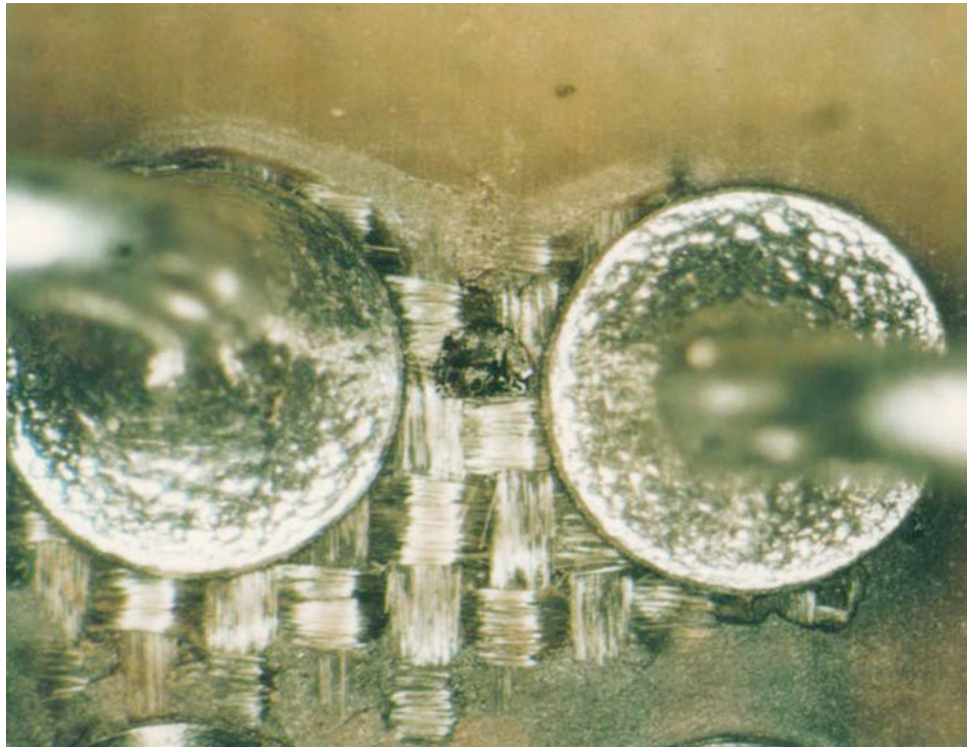


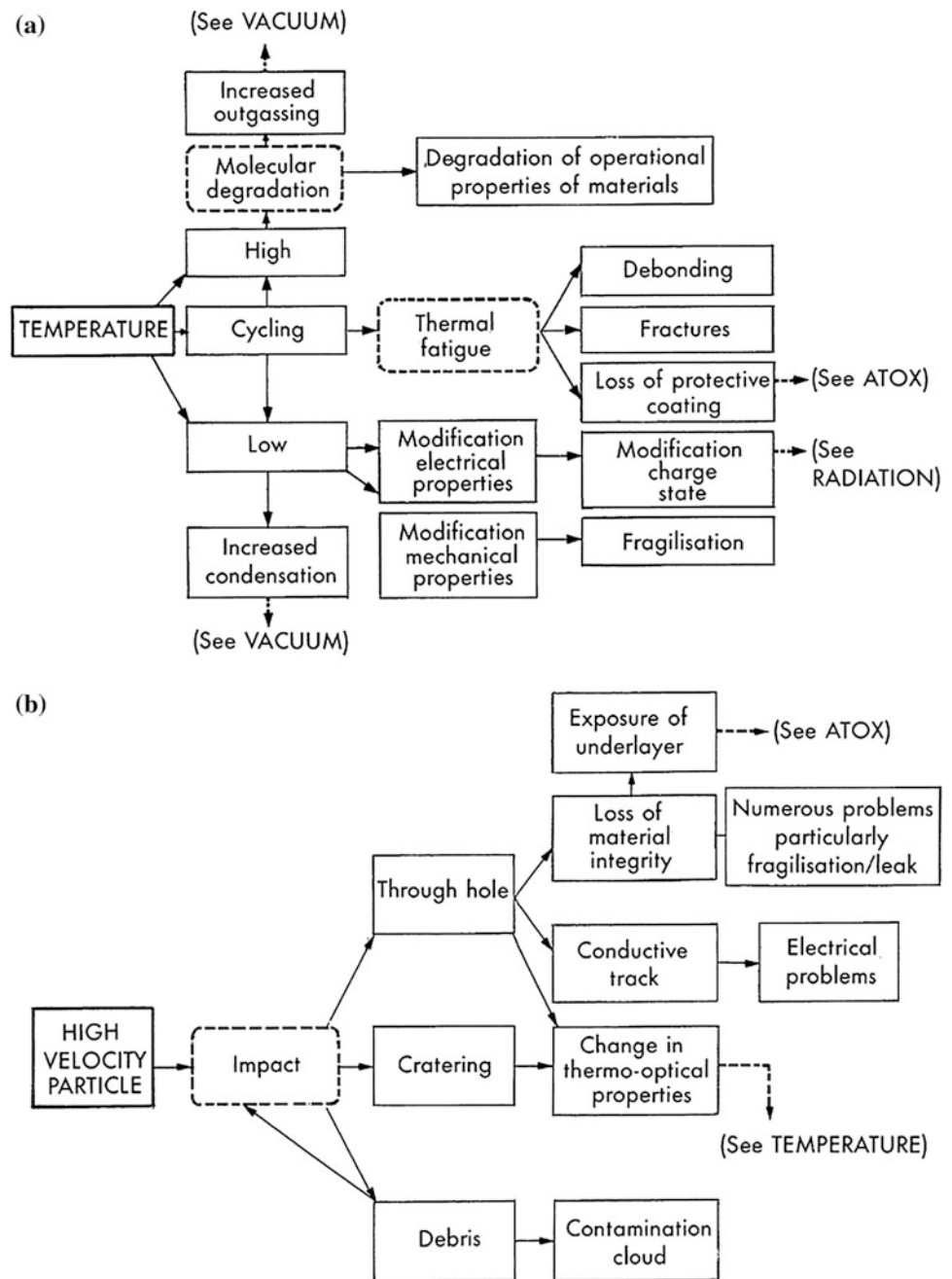
Fig. 8.8 Detail of the damage to the board substrate, some solder splash between the pad terminations, and the granular appearance of the solder



ratio to increase natural atmospheric drag and thus enhance deorbiting and burn out (Pergola 2011). The following sections include data recorded by the writer, but for a

complete treatise on space debris, models and risk analysis the reader may consult the works compiled by Klinkrad (2006).

Fig. 8.9 Space environmental effects: **a** temperature; **b** micrometeoroids and debris



8.4.2 Debris Emanating from Catalytic Bed Thruster Motors

Almost all unmanned spacecraft continue to incorporate monopropellant hydrazine thrusters for attitude control and trajectory corrections. Certain older thruster designs use a catalyst bed consisting of iridium-coated grains of alumina having a diameter of between 200 and 1200 μm . Small grains provide a high surface area of the iridium catalyst for decomposing anhydrous hydrazine (N_2H_4) into innocuous products consisting of nitrogen, ammonia and hydrogen. This

reaction is strongly exothermic and the hot reaction product gasses expand and are forced through a nozzle to produce thrust, usually in the form of specific, high energy impulses of greater than 10 N. The thruster design, an engineering drawing, and the appearance of catalyst bed particles are seen in Figs. 5.44–5.48. A screen is incorporated into the thruster adjacent to the nozzle in order to reduce the number of particles exiting through the nozzle. However, small particles are known to be expelled through this screen as the mesh size cannot be so small as to limit the flow of gases and create high internal pressures. It has been reported that up to 30 % of

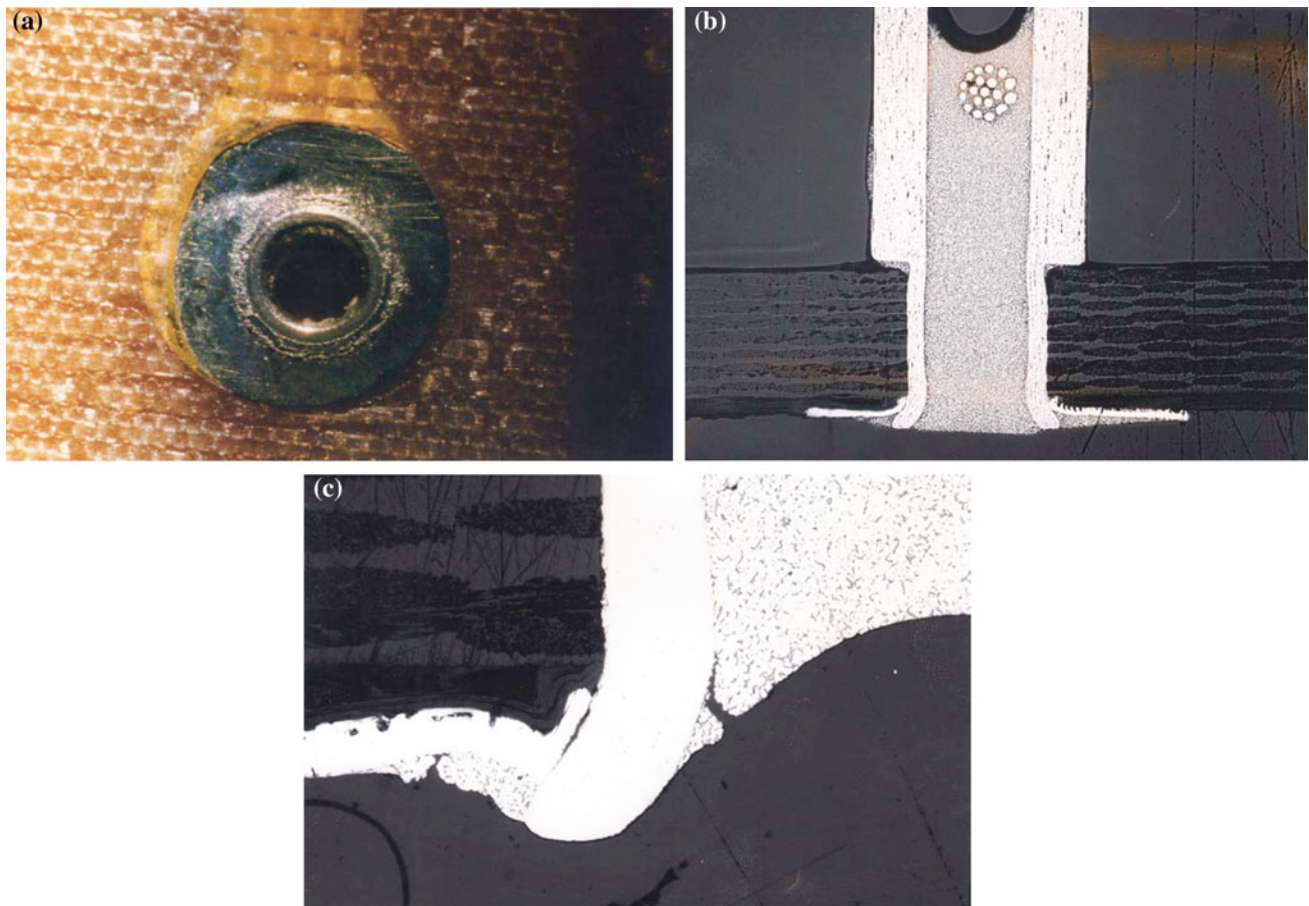


Fig. 8.10 **a** Detailed view of the soldering side of a terminal pin attached to the 'tag board' on HST following approximately 21,000 thermal cycles between -100 and $+90$ °C. Some circumferential cracks are visible and a little 'orange peel' effect ($\times 12$ magnification). **b** Microsection through the solder joint shown in **a**; the PCB has a

thickness of 1.65 mm. **c** Only at a magnification of $\times 100$ can the shallow thermal fatigue cracks and surface roughening be detailed, but the majority of the joint's circumference shows no cracking (de Rooij 1995)

these particles have been lost during repeated firings. Such contaminant particles continue cause a degree of debris to the space environment and there is an environmentally friendly trend for spacecraft to employ other types of small propulsion systems based on either electric propulsion using xenon inert gas as the propellant, or solid "green propellants" as were described in Sect. 3.5. An extensive overview of propulsion systems and their applications is given by Leyva (2011).

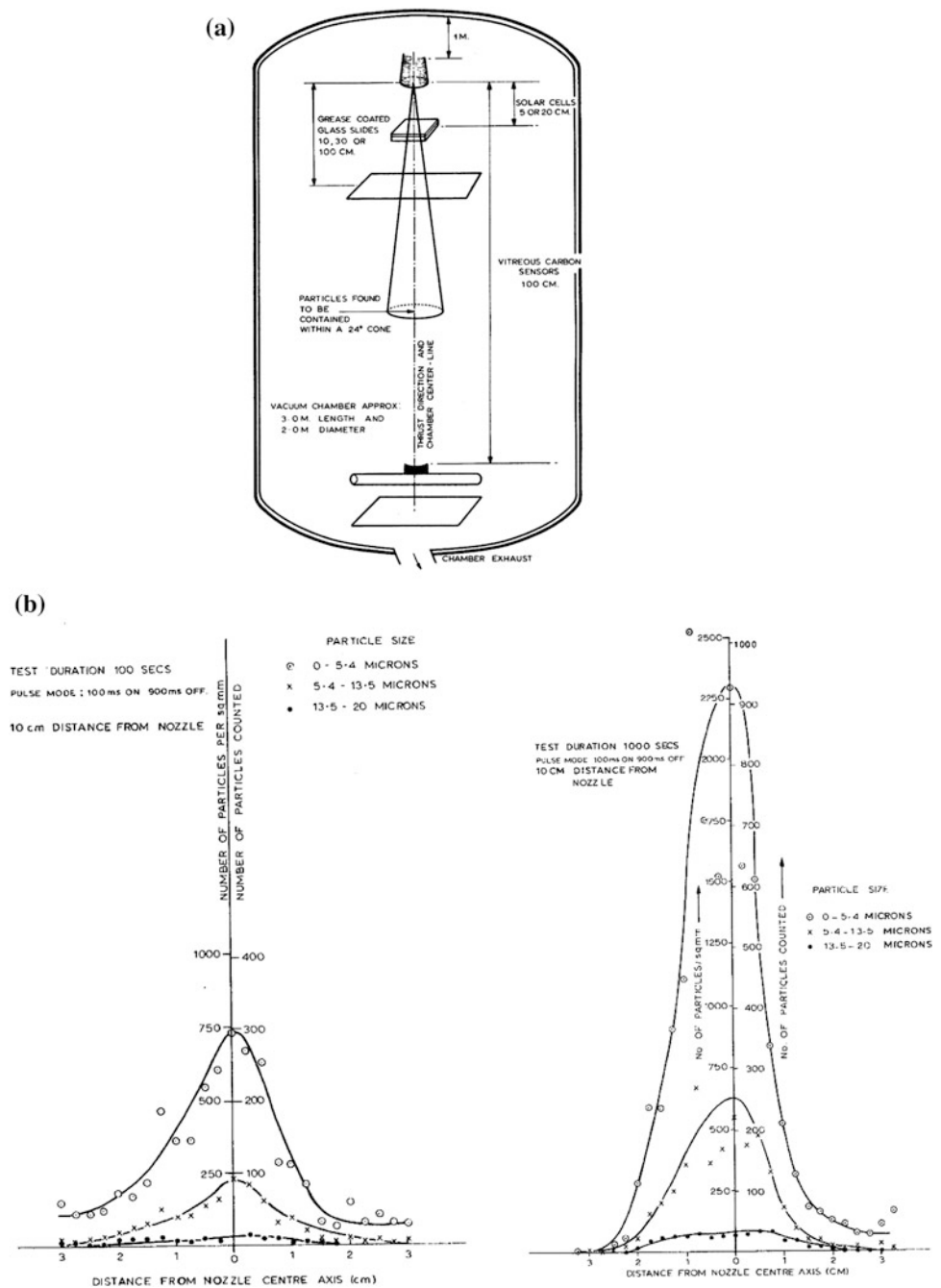
An early experimental set up was used (Dunn and Steinz 1974) to assess both the effects of contamination and heating from a 2N hydrazine monopropellant attitude control thruster on the performance of conductively-coated solar cells, and very sensitive vitreous-carbon sensors attached to long booms planned for use on the scientific satellite GEOS. A large vacuum chamber, 3 m long and 2 m in diameter, was used to determine the angular distribution of catalyst particles to be ejected from the thruster during operation. Simple measurements were possible by placing glass plates coated with low-outgassing silicone grease in front of the thruster

nozzle at right angles to the line of thrust. Temperature excursions were measured with high accuracy, rapid response (10 ms) thermocouples attached to the GEOS hardware. Oil contamination sensors were also distributed around the chamber—these established that there was no contamination caused by the pump down motors of the vacuum chamber. The 2N thruster had a nozzle-area expansion ratio of 50, and a nozzle-exit lip angle of 15° . A diagram showing the motor exhaust plume and sample positions is seen in Fig. 8.11a.

A brief summary of the results from the test programme are as follows:

- (a) The heating rate and temperature of the sample surfaces exposed to steady state and pulse-mode firings have temperature gradients dependent upon the nozzle to sample distance. After 1000 s, the sample surfaces reached their maximum, or equilibrium temperatures (between 180 and 220 °C).

Fig. 8.11 **a** Schematic diagram of motor exhaust plume and position of samples within the vacuum chamber. **b** Particle size and distribution count over grease-coated slide following thruster motor firing in pulsed mode (100 ms on, 900 ms off). The x-axes show number of particles per mm^2 as well as actual number of particles counted. y-axis records the distance from nozzle centre up to a circular diameter of 6 cm. The *left-hand graph* is for at test duration of 100 s, on the *right* is graph for a 1000 s, with slide at 10 cm from nozzle



- (b) Photoelectric yield data for the vitreous-carbon sensors proved they were not affected by thruster heating or contamination.
- (c) The conductively-coated solar cell cover slips showed no significant change in surface resistivity and no damage from the exhaust plume.
- (d) The grease coated slides did collect iridium-coated alumina particles—many thousands were entrapped on the slides as black spherical particles and these slides were subjected to image analysis (Quantimet 720B) and electron microscopy. The particle size and distribution

count over two slides are seen in Fig. 8.11b. The maximum size of particles to be released is 20 μm , the majority had a diameter of under 5.4 μm .

8.4.3 Returned Hardware

Micrometeorites and the <20-micron-sized particulate contamination ejected from thruster motors, as documented in Sect. 8.4.2, are dangerous but do not pose the same threat as

space hardware debris. They are smaller in size and have a lower density, being composed of a material similar to sand. Debris that originates from spacecraft is generally made of heavy metallic materials and may consist of steel bolts, copper wires, released aluminium lens caps, titanium fuel tanks, and the like. A great effort is now being made by the various world space agencies to control the amount of debris in space. As mentioned earlier in this chapter, many experiments have been devised to evaluate the effects of the low Earth orbit environment on spacecraft. Some of the findings will be summarized here, particularly with regard to impacts of debris and meteoroids on the Eureka spacecraft returned from space and the solar array of the Hubble Space Telescope (see also Fig. 8.4). Information on more than 20,000 catalogued space objects is assessed by engineers as a basis for risk assessment in the planning of future spacecraft orbits. Similarly, a model for the micrometeoroid environment surrounding the Earth is available and continues to be upgraded as new data are collected. Unfortunately, the active removal of debris from orbit using laser evaporation or debris ‘sweeper’ mechanisms is in its infancy and may be economically impossible. The focus must therefore be on preventative measures such as the maneuvering of spacecraft and rockets out of heavily trafficked orbits by means of their thruster motors, preferably into orbits that will carry these parts back to the Earth’s atmosphere. Also, the practice of generating pieces of metal coming from the in-orbit fragmentation of pyrotechnic cutters, clamp bands, springs, and other release mechanisms is now curtailed. One upper stage of an Ariane IV launch vehicle exploded in a Sun synchronous orbit in 1986. This alone produced 499 catalogued pieces of debris, among which 61 were still in orbit seven years later (Laporte-Weywada et al. 1993) and some stringent general policies concerning launcher debris have been made subsequent to this explosion (covering both Ariane 5 and 6) which drastically reduce the risk of creating debris. In 2009 a defunct Russian satellite collided with and destroyed a US commercial satellite and this collision alone introduced another 2000 pieces of trackable debris to the catalogued space objects. In an incomprehensible 2007 test, China used a missile to blow-up an old satellite and this created a further 3000 pieces of debris.

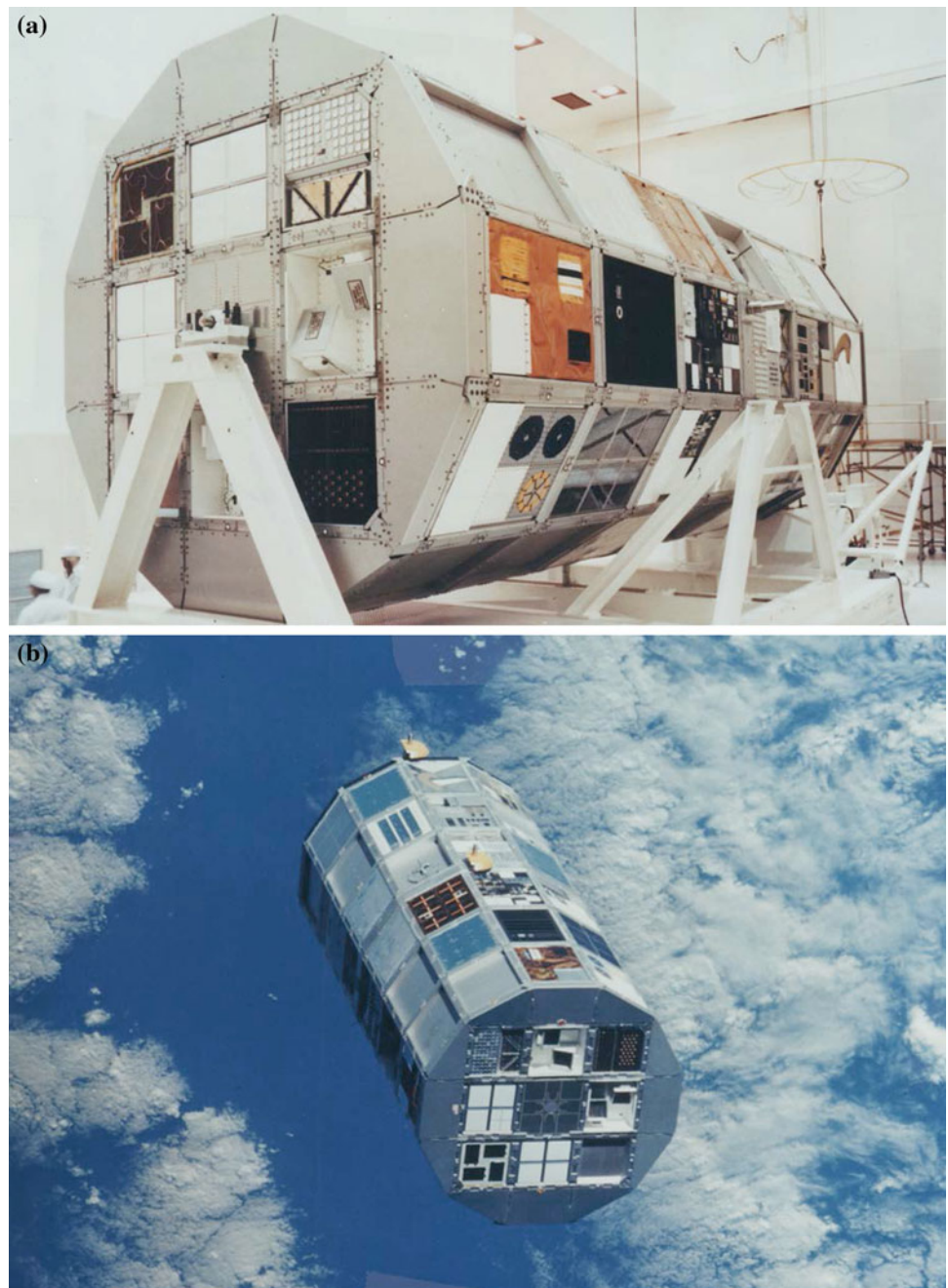
The consequence of interaction between hypervelocity particles and spacecraft surface is rather obvious, but itemized in Fig. 8.9b. The Space Shuttle windows had to be regularly replaced because of particle impacts. The surfaces of other spacecraft that have been retrieved from LEO and brought back to Earth have been found peppered with craters and pin-holes caused by particle impacts. The NASA LDEF spacecraft, shown in Fig. 8.12, was deployed in an almost circular orbit by STS-41C at an altitude of 477 km. One of its main purposes was to gather in situ data of particles in LEO by means of experiments covering materials, coatings,

and thermal systems. 68 months after launch, the spacecraft was recovered and returned to Earth. At least 34,000 impacts were recorded on all the space-exposed surfaces; some are illustrated in Figs. 8.13 and 8.14. Particles were noted to have pierced aluminium screens 0.8 mm thick but that multilayer materials of teflonized woven glass were less damaged (Durin et al. 1993). Solar cells with various cell covers showed that polymer cell covers provide very little protection. When the crater impact diameters were about 100 μm , 2–4 % degradation in short-circuit current was observed—with smaller impact sizes, no measurable changes in efficiency were observed. If the cell itself was damaged, the loss in current was proportional to the size of the damaged area (Gruenbaum and Dursch 1993). Similar impact holes were seen on the returned HST array (Fig. 8.4) and detailed in Fig. 8.15, but here they accounted for an insignificant loss of power. The Eureka spacecraft was retrieved in 1993 after almost one year in LEO. With a total area of 140 m^2 the observed impacts included 73 penetrations of the outer layer of the thermal blankets which covered most parts of the spacecraft’s external body, and more than 2000 impacts on the front face of the solar arrays. The size of recorded impact features ranges from about 30 μm to 6.5 mm (Drolshagen et al. 1996). One impact on Eureka’s painted scuff plate is shown in Fig. 8.16. The ESABASE meteoroid and debris tool was used to predict particle flux for the Eureka mission (for details of the model see Berthoud 1994). Figure 8.17 shows that there is a good comparison between Eureka measured and modelled fluxes and LDEF measured flux in terms of particle diameter.

8.4.4 Protection Shields

The growing amount of man-made objects in LEO may also require the protection of sensitive parts of unmanned spacecraft such as the electronic boxes for Earth observation satellites. In fact Canada’s Radarsat incorporates modifications designed to reduce the crippling effects of impacts. Shielding blankets cover fuel lines, wiring bundles, and electronic boxes—these add 17 kg to the satellite’s mass but are said to increase the odds of survival of 87 % (David 1995). This satellite orbits the Earth at 800 km where there is a high level of space debris, including tiny paint chips, fragments from spent rocket stages, and fluids that leaked from a retired nuclear-powered spacecraft. Shields with multi-layer designs are termed “Whittle shields” as they had been initially proposed by Frank Whittle in 1947. The development of the International Space Station (ISS), now with a final-build cross-section of about 11,000 m^2 , prompted NASA and associated space agencies to pay more attention than ever to debris hazards during early design stages (Chenard 1990). The ISS has been designed to

Fig. 8.12 The long duration exposure facility (LDEF): **a** during experiment integration; **b** spacecraft in orbit. LDEF was deployed from the orbiter's cargo bay during STS 41-C mission in April 1984. The 10-tonne, 9.1 m long, 4.3 m diameter, and 12-sided space platform was later retrieved in January 1990. LDEF's 86 experiment trays provided immense space environmental effects data



withstand impactors of up to 1 cm in size by the incorporation of three kinds of Whittle shields (an aluminium alloy bumper-plate to break up and melt a particle on impact; an outer bumper plate with an underlying blanket of Nextel ceramic cloth and Kevlar fabric spaced away from the module pressure shell; and, a multilayer shield consisting of multiple layers of fabric and metal panels to protect the most critical parts of ISS).

Since only larger space objects can be catalogued and tracked, it is these that have been avoided by evasive manoeuvres—the uncatalogued smaller debris can, and have

been, shielded against using passive protection techniques. The Giotto spacecraft, seen in Fig. 4.44, achieved protection by means of a Whipple Shield consisting of layers of aluminium, Nextel and Kevlar. According to studies, shields can provide reasonable protection against fragments of less than 15–20 mm diameter, with velocities of 10–12 km/s. These represent 78 % of the debris population. European studies favour shields of aluminium and ceramic cloth bumpers. Many possible combinations of protection-shield materials have been investigated by ground simulations and one is illustrated in Fig. 8.18.

Fig. 8.13 Part of the LDEF surface covered with impact records



The present activities are focusing on advanced measurement techniques for hypervelocity impact testing. Little research has been published on the effects of such impacts on space hardware, and there is almost a total absence of data related to fracture critical equipment such as pressure vessels. Poe and Ruckner (1993) have tested pressure vessels constructed from aluminium alloy 6061-T62, with a burst pressure rating of 15.3 MPa. It was indicated from their results that the vessel's internal pressure has an effect on the severity of impact damage. A critical pressure could be identified above which catastrophic failure usually occurred (for those vessels it was about 3.45 MPa). By maintaining

vessel pressure below the critical value, catastrophic failure can be minimized, thus reducing the risk of secondary damage to equipment and personnel.

8.5 Effect of Atomic Oxygen on Materials

A satellite in geosynchronous orbit and operating at a height of 22 000 km will experience about 90 thermal cycles per year, and at this altitude only vacuum radiation and thermal flux will contribute to environmental wear-out mechanisms. A spacecraft in a Low Earth Orbit (LEO) will, in contrast,

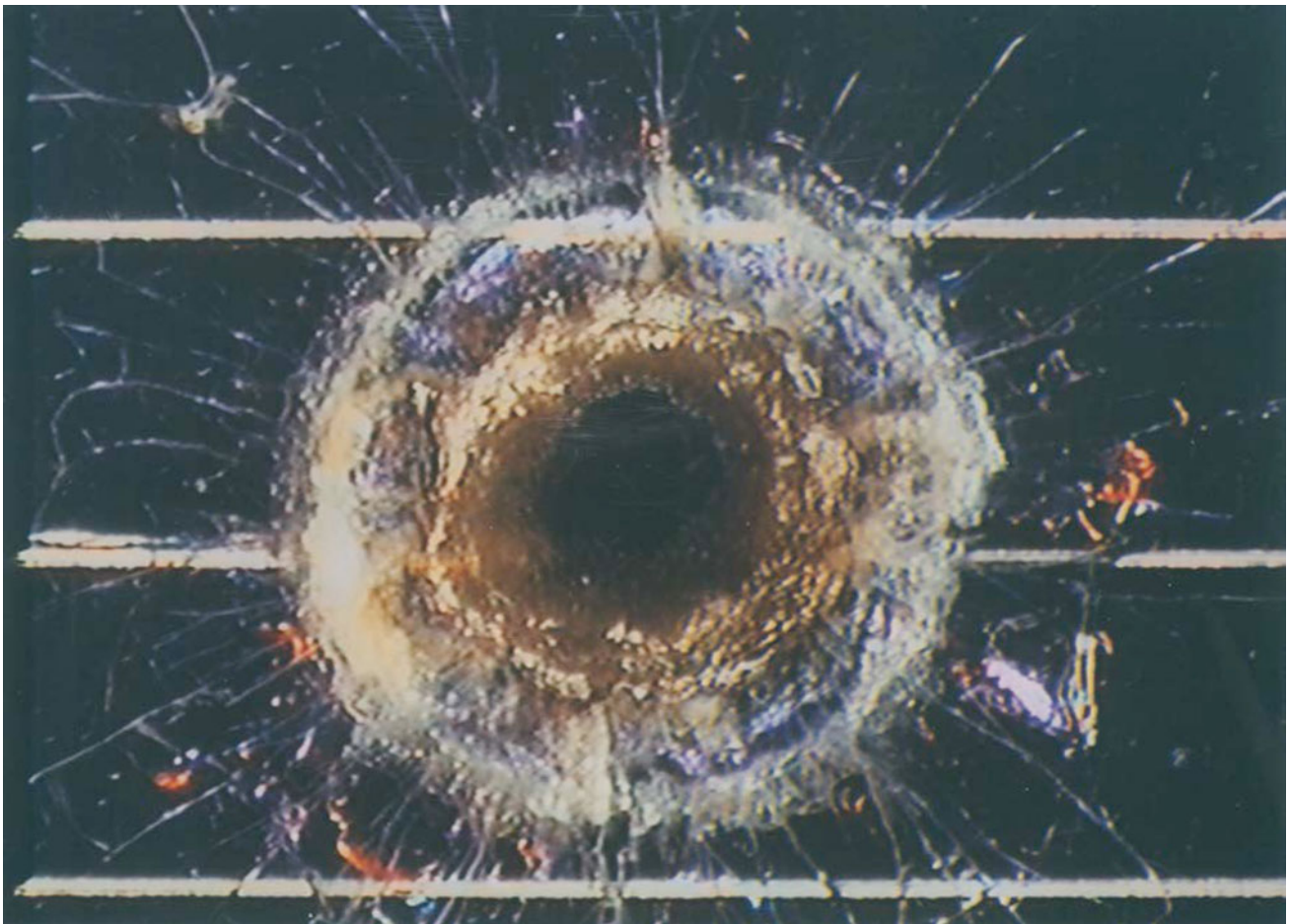


Fig. 8.14 Detail of micrometeoroid impact on solar cell

experience up to 16 thermal cycles per day, and at an altitude of between 200 and 700 km by far the greatest problem is degradation and erosion of externally exposed materials by atomic oxygen (see Table 2.3 and Fig. 8.19).

The effects of atomic oxygen were not considered until engineers began to notice measurable, visible material loss on Space Shuttle missions after only tens of hours in LEO. Oxidation and erosion were not a significant problem on the relatively short-term Space Shuttle missions, but similar rates of material degradation were considered unacceptable on the 30–40-year ISS programme. The hazard of radiation by neutral atomic oxygen arises from the photo-dissociation of upper atmosphere molecular oxygen. This atomic oxygen impacts spacecraft surfaces in the ram direction with an energy of about 4–5 eV, owing to the relative velocity of the orbiting spacecraft. The high velocity of the Shuttle (approximately 8 km/s) produced a flux of atomic oxygen on a ram-facing surface in the order of 10^{15} atoms/cm². This flux has been found to be strongly chemically reactive with many of the thermal control films and paints usually used on the external surfaces of conventional spacecraft. In particular, many organic polymer materials were severely degraded

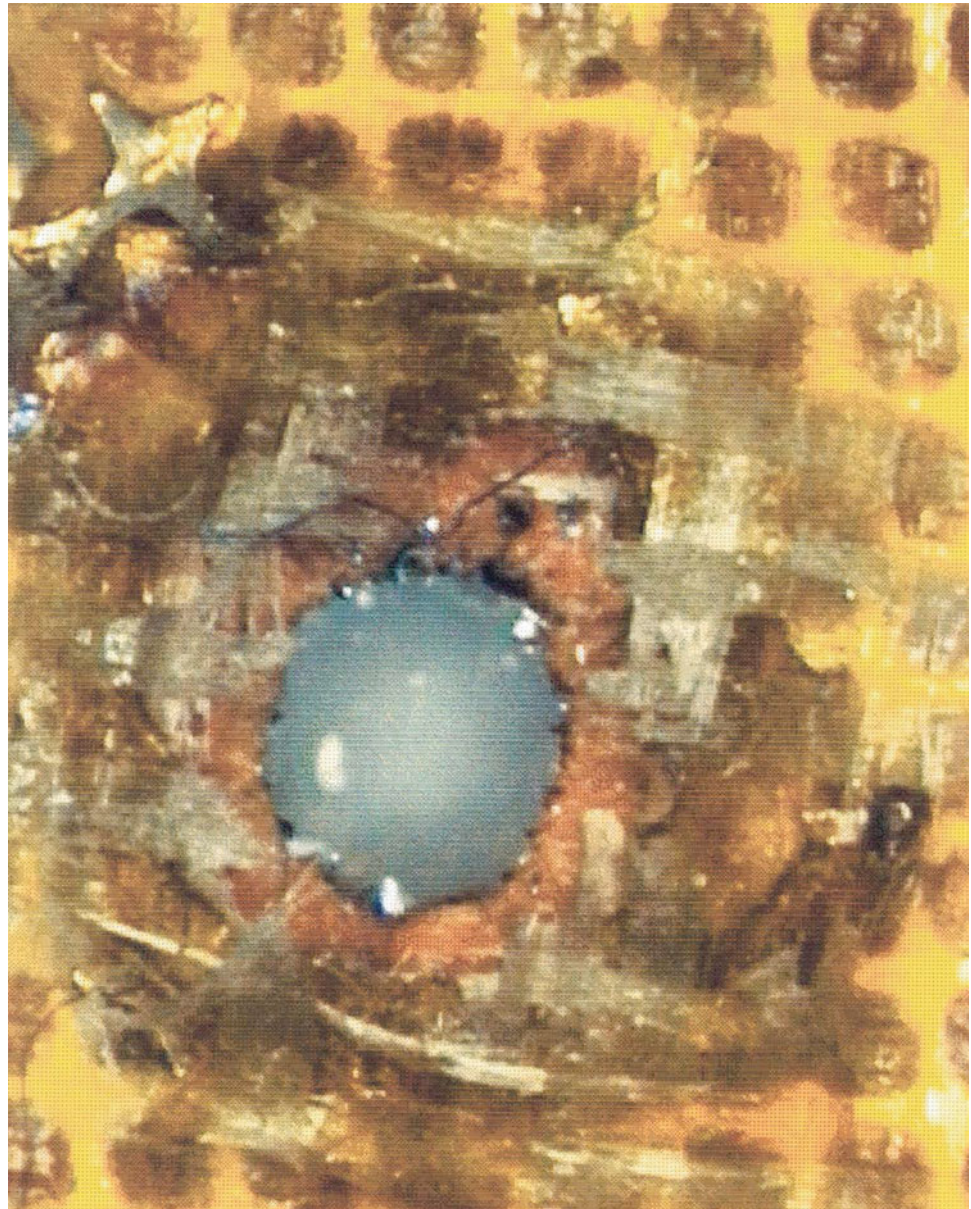
after only 40 h of exposure. This is evident on Kapton samples observed after flight (Fig. 8.20), and high recession rates have been measured by Pippin (1995).

Organic paint binders such as methyl silicone or polyurethane react with atomic oxygen to form volatile carbon-based molecules which are removed from the paint surface (Zimcik 1987; Jagers 1993).

Lubricant films of molybdenum disulphide were exposed to atomic oxygen during some LEO flights. This lubricant is used on a variety of spacecraft mechanisms such as release/deployment devices and precision bearings. Post-flight examinations indicate that the MoS₂ can oxidize to MoO₃, which is an inferior lubricant with a higher friction coefficient. If mechanisms are continually used in orbit they should be shielded from atomic oxygen to avoid accelerated wear.

Metals have been observed to react less than polymers to atomic oxygen attack, although important exceptions are silver, osmium, and copper as shown in Table 8.2. Metal oxides (SiO₂, indium tin oxide, Al₂O₃, etc.) are nonreactive because they are already in their highest oxidation state. Carbon–epoxy composite materials have shown a loss of surface resin, and the carbon fibres themselves have been

Fig. 8.15 Rear-side of HST solar array illustrating a typical 2 mm diameter hole where complete penetration of the array has occurred (through cover glass, solar cell, and insulation layers)



seen to be attacked and reduced to porous ridges with little apparent residual strength or stiffness.

The high capture efficiency for atomic oxygen of silver has created a major problem for the manufacturers of solar cell interconnectors, as these are generally made of either thin silver foil or silver-coated molybdenum foil. Degradation of these interconnection materials severely jeopardizes the reliability of solar arrays designed for LEO. A combination of atomic oxygen attack and excessive thermal cycling (e.g. 30,000 thermal cycles for the Hubble Space Telescope during a 5-year period, and 60,000 thermal cycles during the 10-year life of Space Station) is known to result in a premature loss of electrical power generation caused by the thinning and eventual failure of the solar cell interconnector itself or failure of the cell-to-interconnector weldment (see

Fig. 4.63). The appearance of silver interconnectors attacked by atomic oxygen is shown in Fig. 8.21. Progressive degradation of these electrical connections is attributed to the formation of AgO which, on reaching a certain thickness, becomes non-adherent and detaches as flakes during thermal cycling (de Rooij 1985, 1989, 1995). Recent detailed modelling by de Rooij (2010) uses two transport mechanisms to account for the transport and oxidation of silver through pores in the built-up oxide layer—namely, gas-flow and Fickian diffusion. Both mechanisms result in the parabolic growth of oxide.

Protective measures that either slow down or prevent the attack of atomic oxygen have been proposed by Dauphin (1987). They rely on the use of vacuum-deposited protective coatings known to be resistant to atomic oxygen, such as:

Fig. 8.16 Impact feature on a painted steel scuff plate. The crater centre is about 0.5 mm in diameter. The *circular patch* around it where the paint has been removed by the impact is about 3 mm wide (Drolshagen 1994)

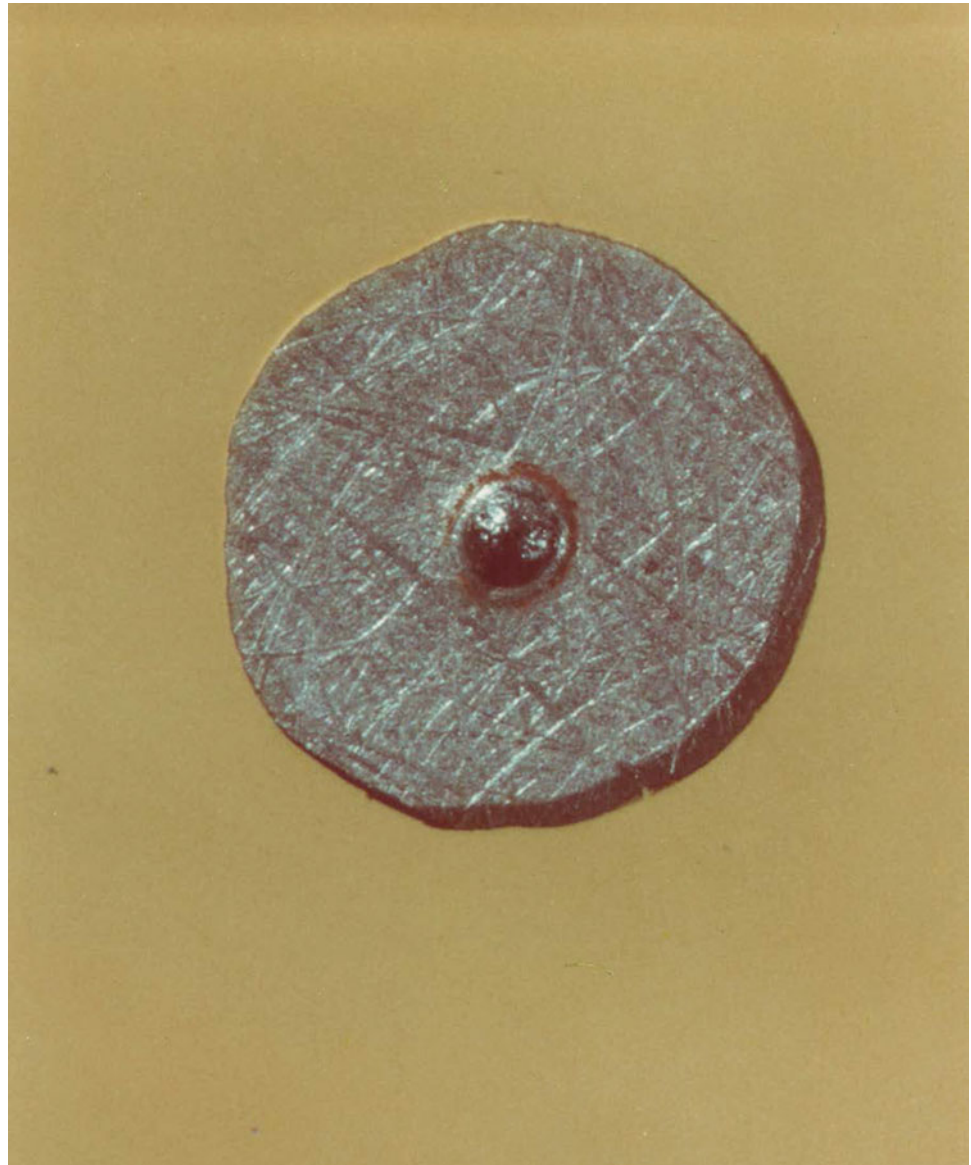


Fig. 8.17 Comparison between Eureka (EURECAmeas) and LDEF leading and trailing measured fluxes (LDEFleadmeas and LDEFtrailmeas) and the results of the ESABASE modelled flux (EURECA_{tot})

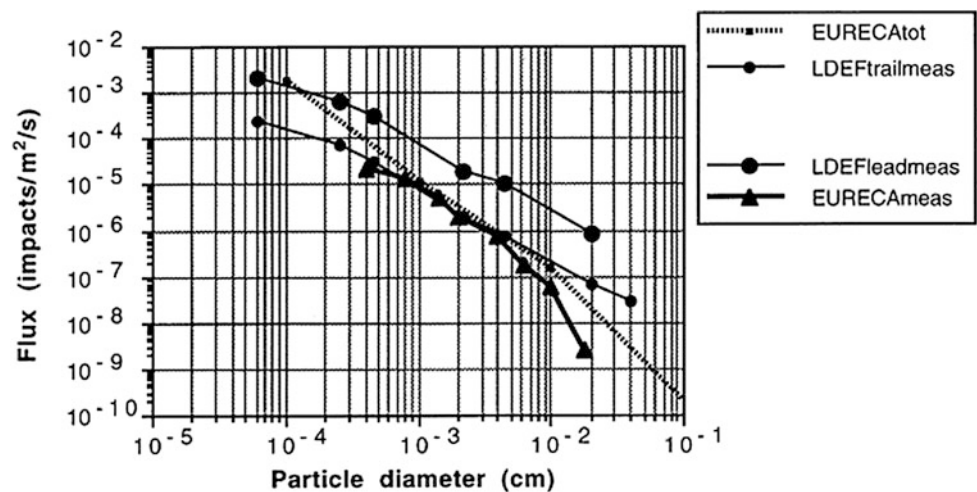
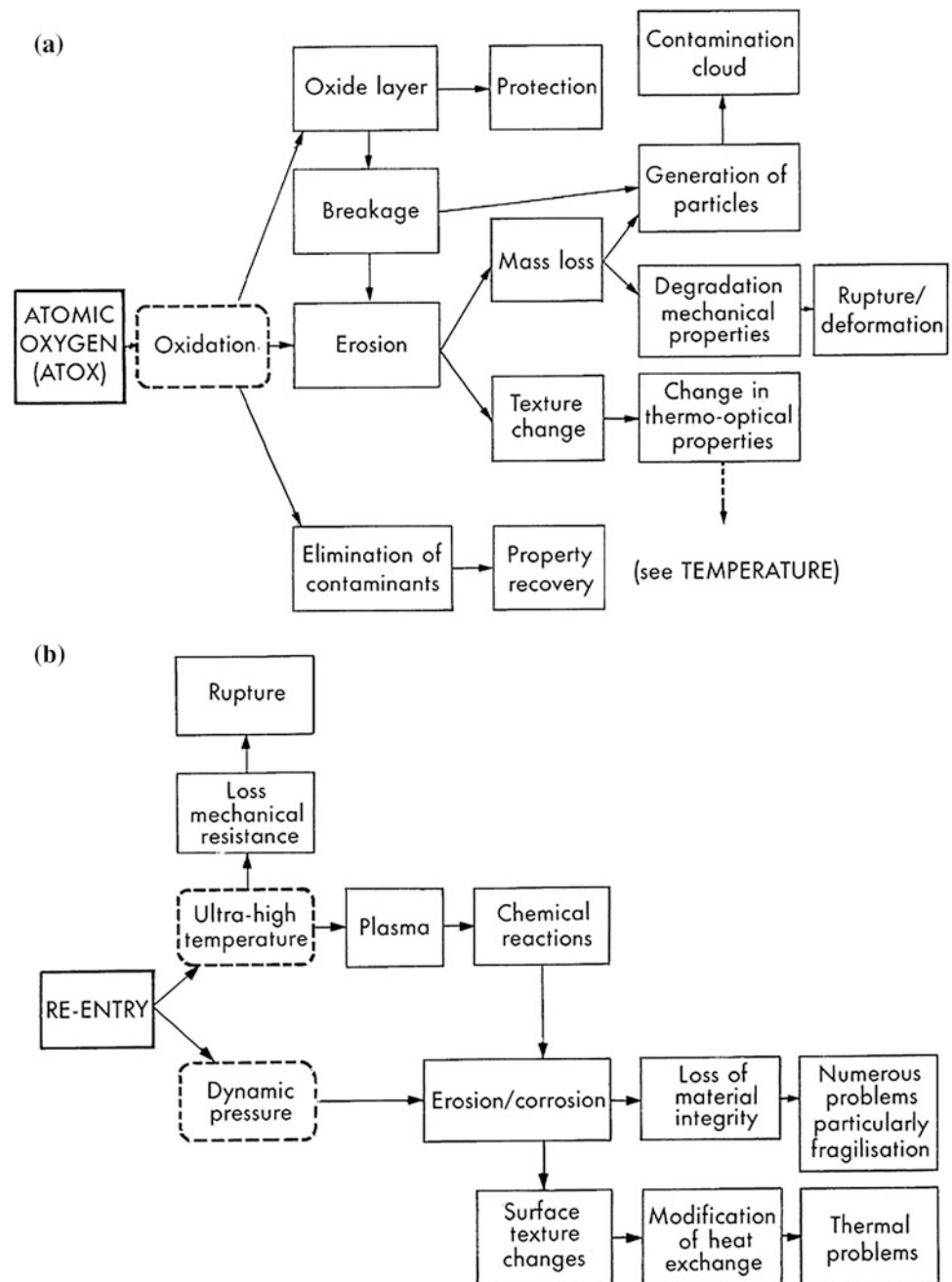


Fig. 8.18 a A simulation of the wall of the ISS *Columbus* Attached Laboratory after being hit (from the *right*) by a 10 mm aluminium projectile at a velocity of 5.5 km/s. From *right to left*, the layers are: the shield or first bumper, the second bumper, multilayer insulation (before the test, it resembles many layers of foil but has been shredded by the impact), the wall of the spacecraft, and several witness plates used only in testing.

b Details the damage on the face of the second plate caused by a cloud of aluminium plasma and debris



Fig. 8.19 Space environment effects: **a** atomic oxygen; **b** re-entry



- Metallic layers of platinum and aluminium.
- Stable oxide layers such as Al_2O_3 , SiO_2 , or indium tin oxide.
- Silicone layers that are possibly protective owing to the formation of a thin, self-healing layer of silicon oxide.
- Fluorinated layers.

Many articles returned from LEO have been seen to support a light-brown contamination layer. Analyses have shown this to be a deposited layer containing silicones (condensed volatile materials from outgassing sources); this layer may only be a few angstroms thick; it then oxidizes in

the atomic oxygen atmosphere to form silicates and silica—both protective compounds that are resistant to further erosion.

It is clear that a great deal of ground-based research is developing theoretical models to account for material degradation and protection methods to meet the challenge of atomic oxygen. Ground-based atomic oxygen simulation facilities have been designed and commissioned (at ESTEC, PSI, DERTS, AODTS, PPPL, and UTIAS). The ground tests on metals and polymers are giving results comparable to some LEO exposures, but as often seen in nature, it is the complex synergistic reactions—between atomic oxygen, UV

Fig. 8.20 Effect of atomic oxygen on Kapton H surface before and after STS 5 flight. Degradation is by mass loss and surface texturing (Micrographs courtesy of A. de Rooij)

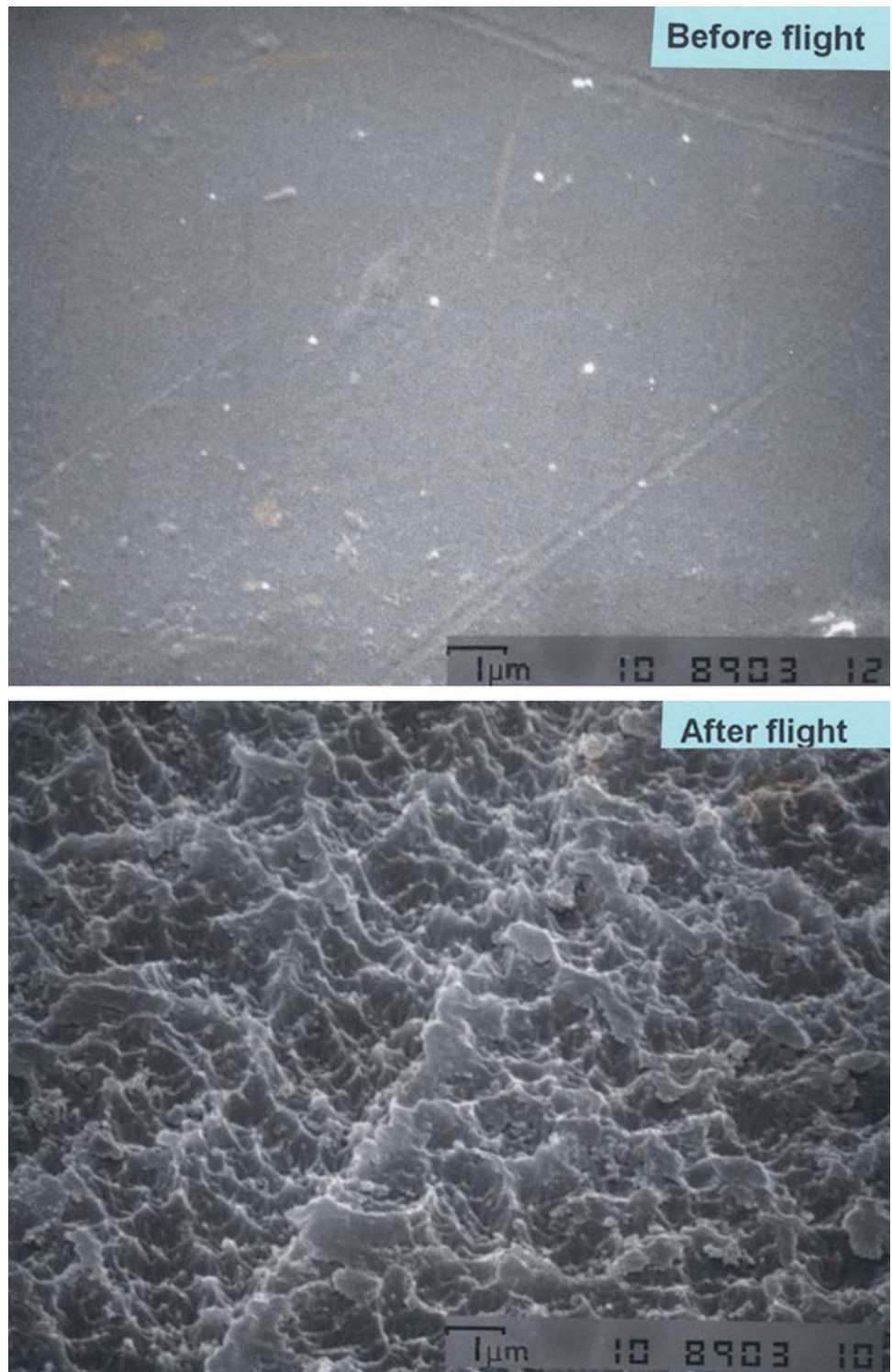


Table 8.2 Reaction of atomic oxygen with selected metals (data from LEO exposure)

Metal (protective system)	Reaction efficiency $R_e \times 10^{-24} \text{ cm}^3/\text{atom}$	Oxide type	Comment	Collated reference
Aluminium	0	Al_2O_3	Self-protecting	S
Brass, bronze	0			P
Chromium (100 Å)	Part eroded		Optical properties affected	S
Copper (bulk)	0	Cu_2O	Self-protecting	SP
Copper (1000 Å)	0.006	Cu_2O	Optical properties affected	S
Gold	0		Nonreactive	S
Gold on Ag or Mo	0		Protective until silver diffuses through gold	HR
Iridium	0.0007			S
Lead	0			S
Magnesium	?		Slight attack	SP
Molybdenum (1000 Å)	0.006	MoO_3	Slight attack	S
Molybdenum (bulk)	0			S
Monel	0			P
Nichrome (100 Å)	0	Cr_2O_3	Self-protecting	S
Nickel film	0	NiO		S
Niobium film	0			S
Osmium	>0.026		Heavily attacked	S
Palladium	?		Optical properties affected	S
Platinum film	0		Nonreactive	S
Silver	10.5	AgO	Heavily attacked	SH
Silver on Mo		AgO	Heavily attacked	H
Solder (Sn–Pb)	0		No visual change	H
Stainless steel	0		No visual change	P
Tantalum	0	Ta_2O_5		S
Titanium			Slight	P
Tungsten	0			S

REF: S Silverman (1995)

H Hamacher et al. (1995)

P Pippin and Bourassa (1995)

R de Rooij (1995)

$$R_e = \frac{\text{Volume of material lost}}{\text{Total no. of incident O atoms}} (\text{cm}^3/\text{atom})$$

exposure, thermal cycling, contamination layers, etc.—that are almost impossible to reproduce in the laboratory.

8.6 Decelerators and Heat Shield Materials

8.6.1 General Examples

An overview of the various groups of materials that have been selected as the outer skins of thermal protection systems (TPSs) were discussed in Sects. 2.4 and 2.5. Reusable launch vehicles and manned capsules that return to Earth have heat shields made either of lightweight silicon-based ceramic tiles

that have a good resistance to high-temperature oxidation, air turbulence, and shock (See Figs. 2.14 and 2.15), or from ‘ablatives’, such as the epoxy resin-based shields on the Mercury, Gemini, and Apollo capsules, that could only be used for one descent to the Earth’s surface. The Gemini and Apollo TPSs were manufactured from an ultralight ablator called ULD 100 by the McDonnell Douglas company in the USA. Beagle 2 and launch vehicles such as Atlas V, Ariane’s 5 and 6, Vega and Falcon employed cork, as seen in Figs. 2.24 and 2.25.

The effects of re-entry into the Earth’s atmosphere on materials are shown schematically in Fig. 8.19b. A similar chain of reactions can be expected for the TPSs attached to

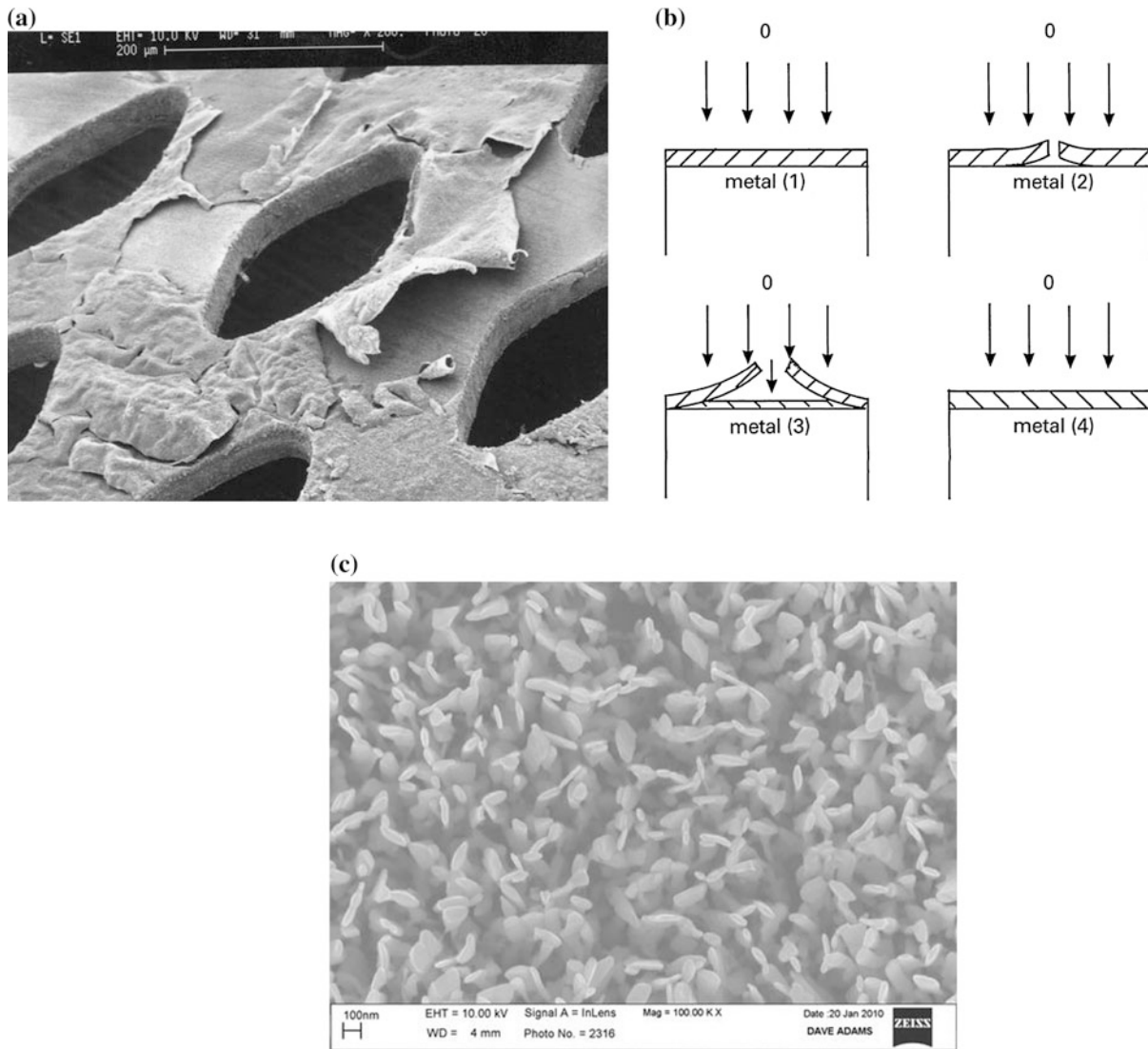


Fig. 8.21 Degradation of silver mesh solar cell interconnectors due to atomic oxygen (Courtesy of A. de Rooij): **a** Silver oxide flakes after atomic oxygen attack during STS flight. Cross-sections revealed the silver interconnector to have thinned from an original thickness of 34 to 29.5 μm . **b** Flaking of oxide layer due to internal stresses and

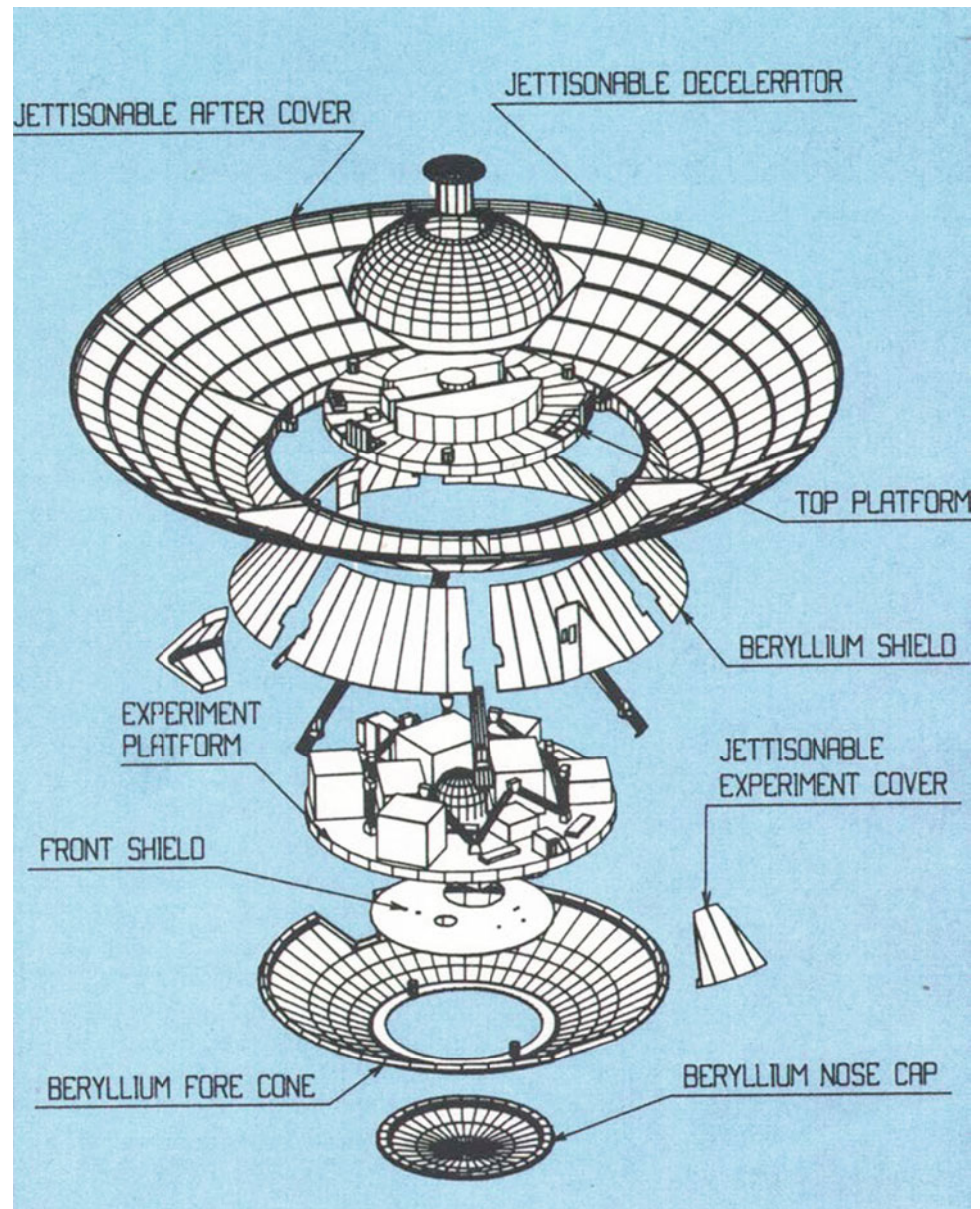
microcracks, primary and secondary oxide layers depict the growth and spalling observed on **(a)**. **c** A recent observation made by de Rooij (2010) and D. Adams, is that the oxidized silver surface consists of nano-flakes and pores

unmanned space probes that are designed to descent onto the surfaces of those planets and moons possessing their own gaseous atmospheres. Space probe missions can usually be divided into four phases: launch from the Earth, coast through space for long periods of time, entry into the planet or moon's atmosphere, and descent onto its surface. The design of these probes usually consists of two major components: The high-speed deceleration system and the descent module. The high-speed deceleration system is often deployable owing to the volume restrictions of most launch vehicles. It must be made of a material having a high heat resistance, low mass, and adequate strength at elevated temperatures. This decelerator is used only in the entry phase of the mission when aerodynamic

braking is required as the probe makes contact with the planet or moon's atmosphere at a supersonic speed. On reaching a subsonic speed the decelerator structure is parted from the probe by the firing of a pyrotechnic device. The probe descent module consists of a TPS (heat shield) that protects the outer envelope of the probe, its equipment, and antennae. When the decelerator is jettisoned, the descent module may be further slowed down by the deployment of a pilot parachute which drags out the main parachute. The probe must possess energy-absorbing properties to cushion it as contact is made with the planet or moon's surface.

The Cassini-Huygens mission is a joint NASA and ESA project to Saturn and its major moon, Titan. The Cassini

Fig. 8.22 A preliminary design for the Huygens Titan probe. This exploded view shows a carbon-carbon decelerator and several beryllium thermal protection components



spacecraft was launched in 1997 in an orbiter (Cassini) and probe (Huygens) configuration. After encounters with Jupiter and a portion of the asteroid belt, it reached Saturn in the year 2003. On completing its first orbit of the planet, the spacecraft released the Huygens probe in the direction of Titan. Eleven days later the Huygens probe entered Titan's dense atmosphere (expected to be composed of nitrogen and methane). Deceleration will be by means of an aerodynamic braking structure. The design of the Huygens probe is drawn in Fig. 8.22. The expected entry and descent scenario is illustrated in Fig. 8.23 and in situ images are included in Fig. 8.24. NASA attempted to use solar arrays to power Cassini but these would not have been possible as the spacecraft would have become too massive. Radioisotope thermoelectric

generators were selected as they remain unmatched for power output for missions to the outer solar system—at the time of writing, this spacecraft continues to relay incredible images of Saturn and its many moons (Fig. 8.25).

The actual material that was selected for the high-temperature thermal protection of the Huygens probe is a low-density ablator called 'AQ 60 I' (a trademark of Aerospatial, France). This material is in full industrial production, being used for the protection of strategic military missiles. It is in fact a felt, made up of short silica fibres reinforced by an impregnation of phenolic resin. AQ 60 I has a final density of 0.3 and a total porosity of 84 %. It is not reusable because part of the material becomes pyrolysed between 400 and 1000 °C. After pyrolysis, this heat-shield material is still

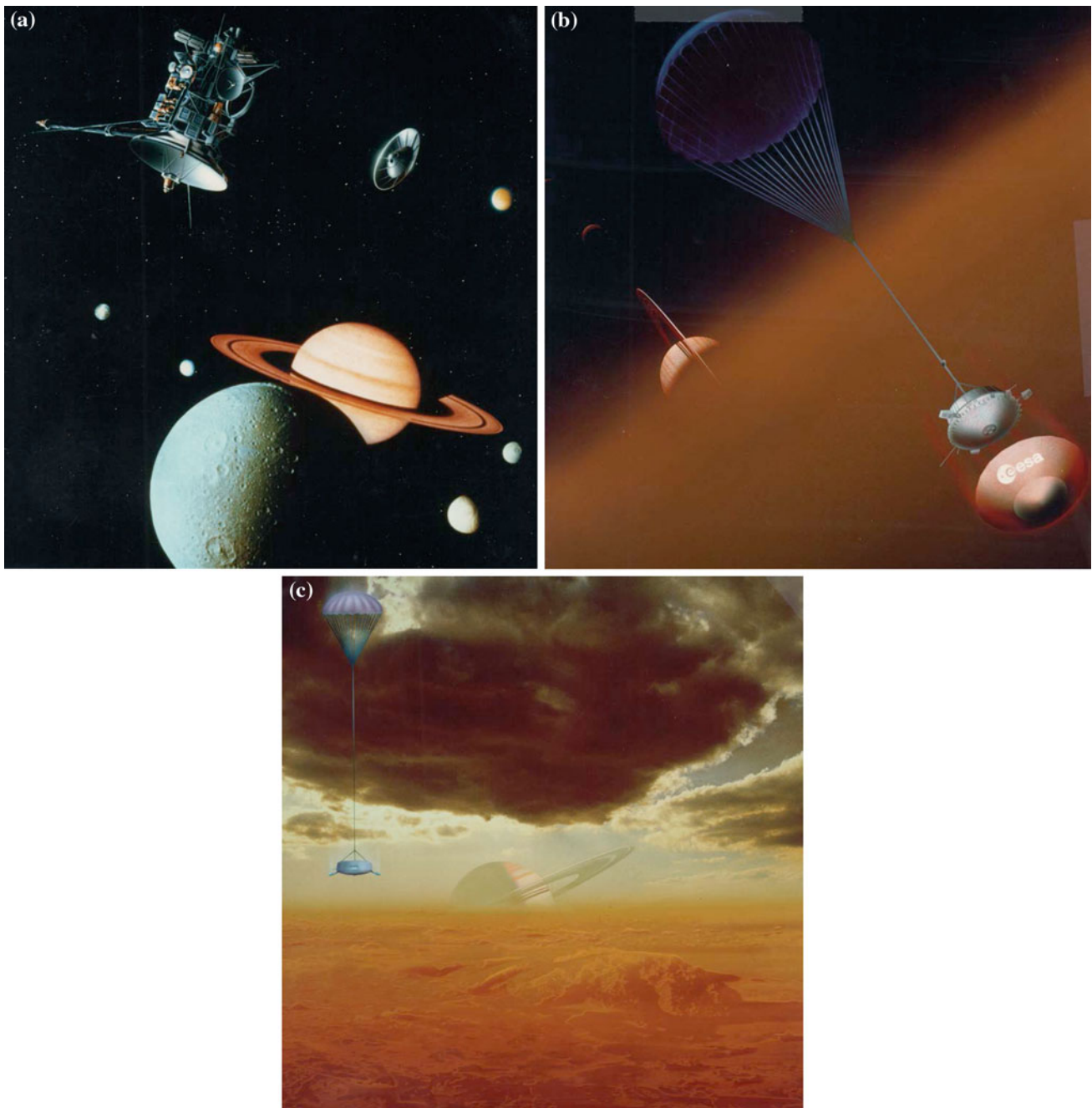


Fig. 8.23 **a** The Huygens probe (ESA) after separation from the mothership, the Cassini Saturn Orbiter (NASA), is depicted in these artists impressions heading towards Titan. **b** Huygens: after entry in Titan's atmosphere on 14th January 2005, the parachute was deployed

and the heat shield separated. **c** Huygens descended through the clouds of Titan, analyzing its atmosphere and transmitting data for 2 h 27 min, after landing it transmitted signals via Cassini for 72 min before its batteries drained (Courtesy of ESA)

self-supporting and becomes an efficient thermal insulator which then behaves like all the silica-carbon systems, being ablated at temperatures in the region of 2000 °C.

During descent, the various sets of instruments on-board the Huygens probe were activated in order to measure

temperature and pressure, atmospheric composition (by mass spectroscopy and gas chromatography), cloud particle sizes and composition, lightning detection, and, for the last phase of the descent, surface imaging was successful as evidenced by the Fig. 8.24.

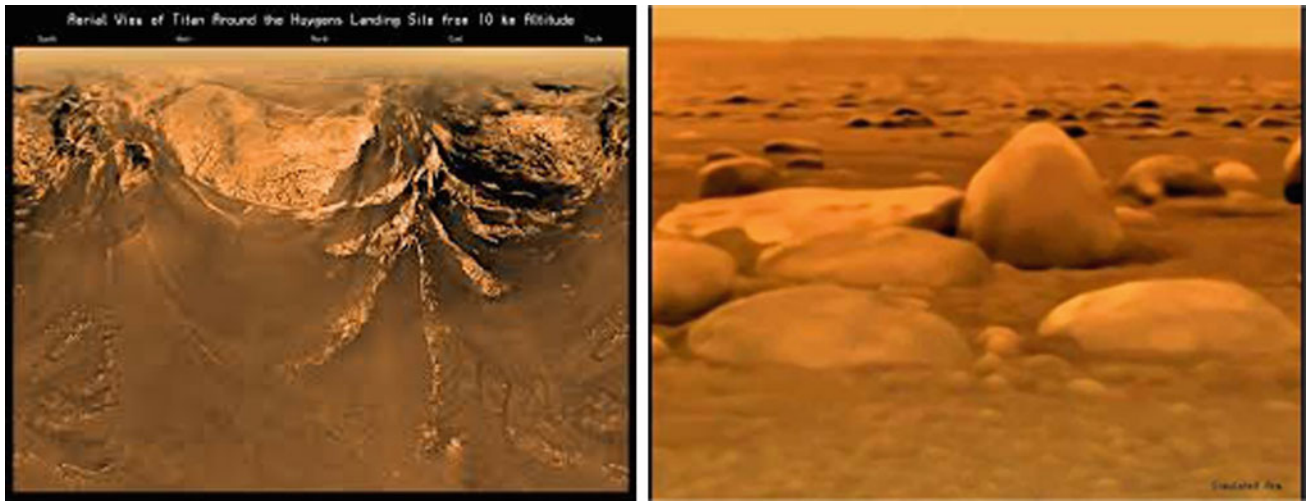
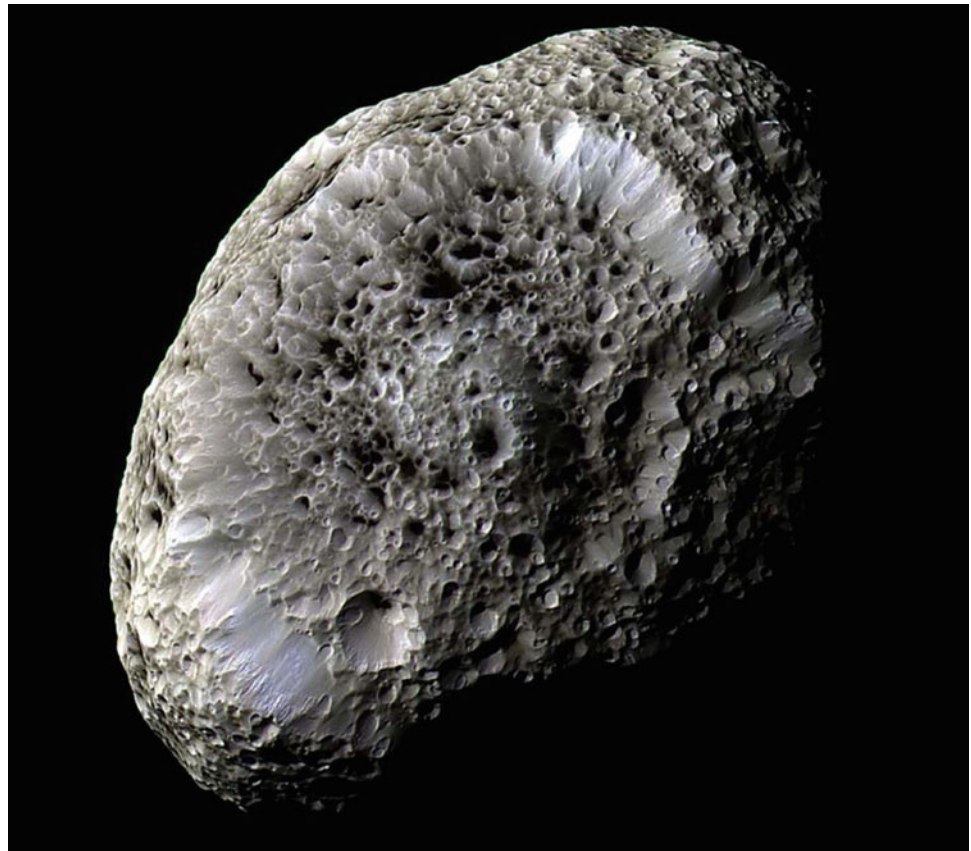


Fig. 8.24 Actual in situ images of Titan's surface from Huygens. Bright highland terrains are visible with deep drainage networks indicating erosion by methane rainfall. It is assumed the rounded

cobbles (10–15 cm in size) are composed of hydrocarbons and water ice. (Credit ESA/NASA/JPL/University of Arizona)

Fig. 8.25 NASA's Cassini spacecraft made its final close approach to Saturn's large, irregularly shaped sponge-like moon Hyperion, taking this image on 31 May 2015



8.6.2 Beryllium as a Heat Shield

The virtues of beryllium, together with some spacecraft applications, have been reviewed in Sect. 5.7. In TPS applications, beryllium can be particularly useful, as it is one of the lightest structural metals known, it has a

high stiffness and strength, and the highest heat capacity of all metals. Beryllium plate and sheet can be easily machined, then milled to exacting final part tolerances by chemical milling, electrochemical machining (in NaCl and NaNO₃ electrolytes), and electric discharge machining.

Although beryllium can be chromate conversion coated with Alodine (as for aluminium alloys) and also anodized to increase its corrosion protection properties, little was known concerning its suitability as a heat shield material. However, it was known that the natural colour of anodized beryllium is black, and this has the added advantage of increasing emissivity (particularly useful for reducing the temperature excursion of a heat shield during descent) and depressing light reflectivity in optical systems. Because of the absence of experience in the anodization of beryllium in the European space industries, a short programme was devised to establish a processing route and expose samples to a series of environmental tests which might simulate some of the rigours of a heat shield similar to that required by the Huygens probe. To reduce the temperature excursion during descent through the mainly nitrogenous atmosphere of Titan, a very high surface emissivity of approximately $\varepsilon = 0.7$ is desirable.

The following paragraphs summarize some tests and results from this unpublished programme of work (Semerad and Dunn 1990).

A. Test material

Flat-rolled beryllium sheet, type S-200, with a thickness of 2 mm. Produced by the hot rolling of vacuum hot-pressed block (minimum room temperature properties being 344 MPa yield strength, 482 MPa ultimate tensile strength, and a minimum elongation of 10 %).

Be-samples of size $20 \times 20 \times 2$ mm were machined and subsequently pre-cleaned in a proprietary solution containing carbonates, phosphates, borates, and inhibitors with a pH of 9.6. The samples (anode) were held by titanium clamps and the cathode was made of 3 mm diameter aluminium wire. Anode-to-cathode distance was 20 mm. The anodizing process was performed in a solution of chromic acid (100 gCrO₃/l) with a current of 16 A/dm². Magnetic stirring at 500 rpm assisted the process. Two anodized-layer thicknesses were expected, nominally 5 and 15 μm , using anodizing times of, respectively, 10 and 60 min. These are referred to as thin and thick anodized layers in the results. Electrolyte temperature was 13 °C. Samples were spray rinsed in de-ionized water and finally dried in hot air at 120 °C.

B. Test programme

Multiple samples were made to assess the initial physical and thermo-optical properties of the as-received samples.

Groups of samples were then exposed to environmental extremes:

- thermal cycling under vacuum, 200 cycles from -150 to $+100$ °C, per ECSS-Q-ST-70-04

- high-temperature exposure, 600 °C in nitrogen (8 h)
- high-temperature exposure, 1000 °C in nitrogen (8 h)
- salt spray corrosion exposure (5 % NaCl in water for 192 h at 35 °C).

The physical and thermo-optical properties were evaluated after each of the environmental exposures, and then recorded.

C. Results

(a) Visual aspects

The changes in appearance of the Be-samples due to the environmental exposures were identical for the thin- and thick-anodized layers. The thin-anodized samples are shown in Fig. 8.26. The original Be-oxide layer appears dark black with the rolling texture of the Be sheet just visible. After thermal cycling there is no macroscopic or colour change (only the thick-anodized finish shows some microscopic hairline cracks). After the additional 600 °C nitrogen exposure there is a pronounced colour change to grey/ochre, but the oxide layer still shows no macroscopic defects (the microscopic hairline cracks are still seen on the thick-anodized samples). After exposure to 1000 °C in nitrogen, the surface becomes rugged. White pustules appear, their number and height being greater for the thick-anodized samples. The colour reverts to a darker grey and the rolling texture disappears.

The salt spray test did not degrade the as-received or thermally cycled samples. Corrosive products were seen on all samples exposed to either 600 or 1000 °C; this corrosive attack occurred only at the microcracks in the anodized layer.

(b) Surface analyses

Infrared spectroscopy showed a low IR-reflectance for the as-received and thermal cycled samples. After 600 and 1000 °C exposure in nitrogen, the surfaces appear to have very slightly transformed to nitrate. This was confirmed by XPS analysis. X-ray diffraction measurements, with CuK α -radiation, identified only Be and BeO crystallographic phases on all the as-received samples and environmentally exposed samples. However, only the 1000 °C nitrogen-exposed samples contained traces of Be₃N₂.

(c) Thermo-optical properties

The solar absorption for the thin(thick)-anodized layers decreases from 0.95 (0.96) to 0.65 (0.69) after the 600 °C nitrogen exposure, and increases again to 0.8 (0.73) after the 1000 °C nitrogen exposure. Thermal cycling and salt spray corrosion have only very minor effects. The observed

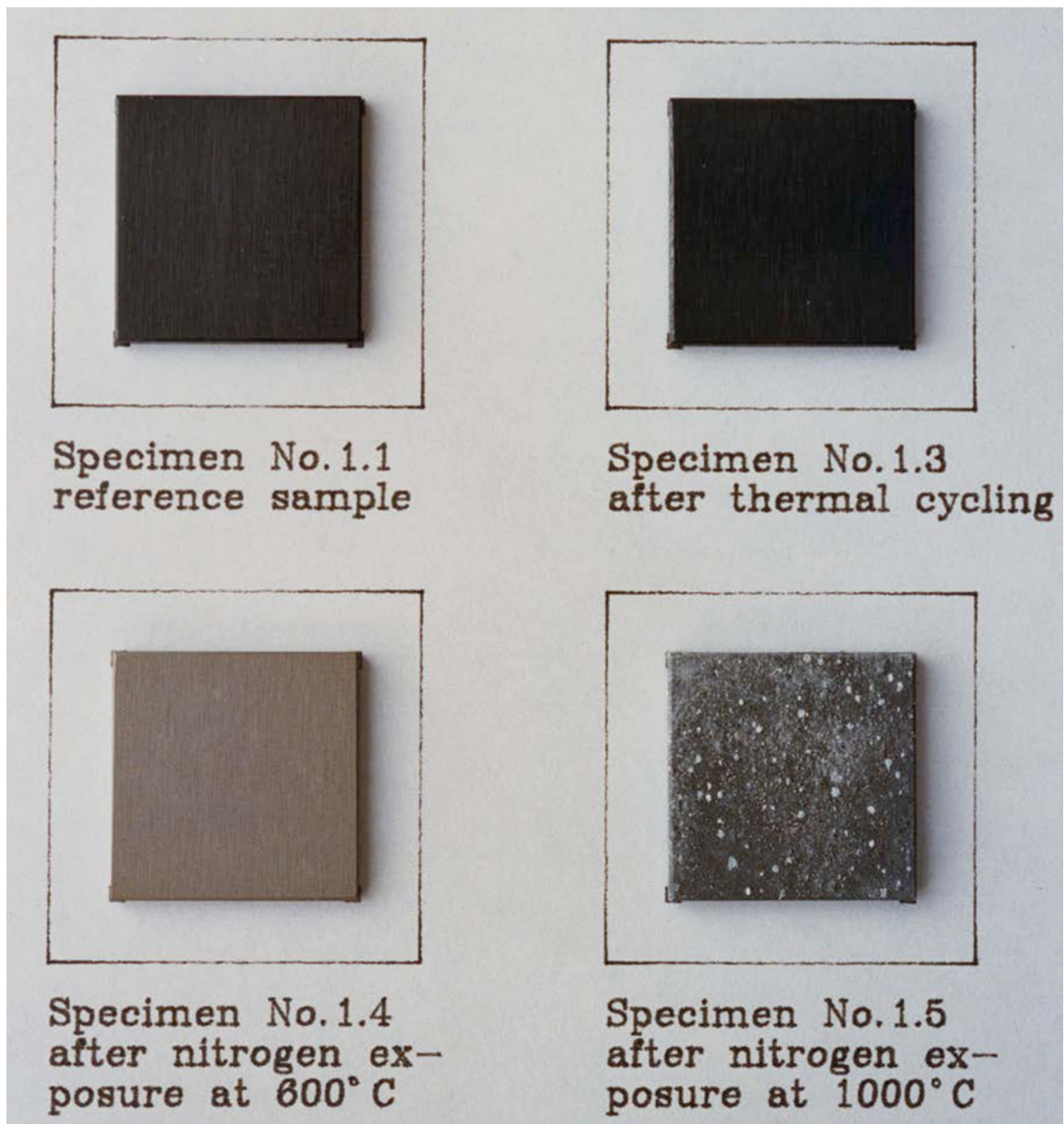


Fig. 8.26 Change in appearance of the Be-samples after different environmental tests (Be-oxide process 1:5 μm)

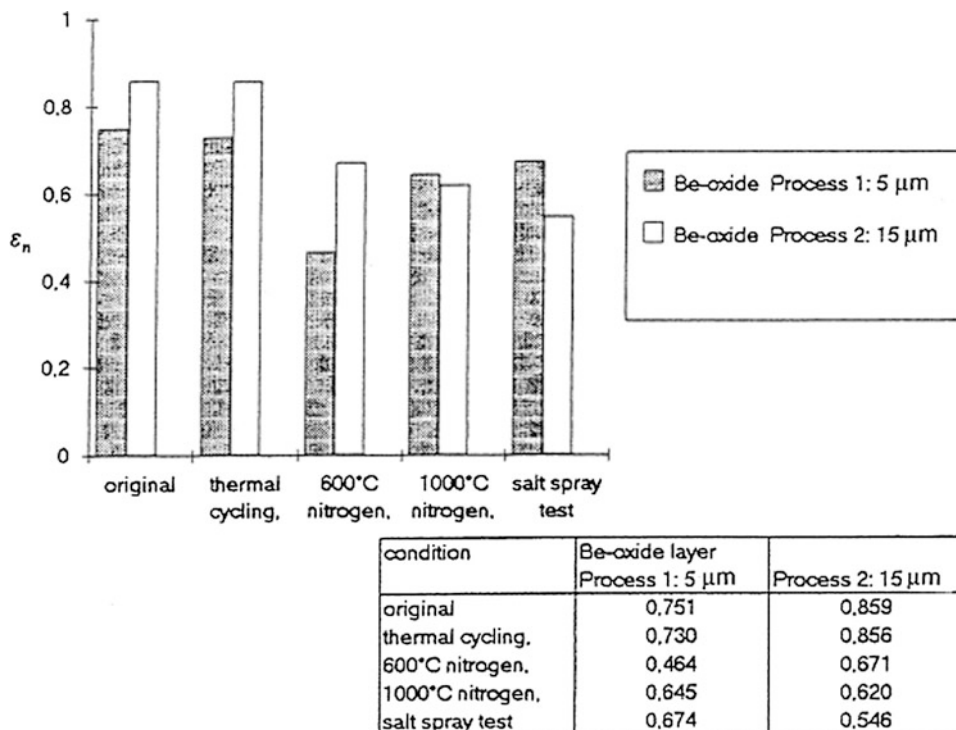
decrease of solar absorptance in the course of the high-temperature nitrogen exposure lowers the heating by Saturn/Titan and solar radiance, but is considered much less important than the observed changes in emissivity. The total hemispherical emittance (average of three samples) is shown in Fig. 8.27. The observed decrease in the emittance after the 600 °C exposure can be understood either as a change of the intrinsic properties of the Be-oxide layer, or in analogy to the

visual spectral range, by an increased transparency in the infrared, so that part of the radiance is reflected/emitted by the Be-substrate surface.

(d) *SEM observation of the environmentally tested samples*

The environmentally exposed samples were carefully handled and mechanically broken to enable examination of their

Fig. 8.27 Total hemispherical emittance, ϵ_n , of the anodized Be-samples in sequence of the environmental tests



cross-sections. Sharp notches were machined into the Be from the underside; the samples were then pulled in tension and this resulted in brittle fractures at right angles to the anodized surface. Figure 8.28 shows that the nominally thin (5 μm)-anodized layer is in fact 2 μm in thickness. Similarly, Fig. 8.29 shows that the thick-anodized layer is also of inadequate thickness, being only 8 μm instead of the nominal 15 μm. After thermal cycling there is good adherence between oxide and substrate, but more microcracks in the thicker oxide layer. This holds true following thermal cycling plus the 600 °C nitrogen exposures. After an additional 1000 °C exposure, plus salt spray testing for 8 days, there are extensive signs of oxide breakdown and corrosion of the Be-substrate and this has occurred for both oxide thicknesses.

D. Conclusion

The thin (actually 2 μm)-anodized layer shows a better mechanical performance regarding cracks and detachment, but the thicker layer (actually 8 μm) is better suited in view of a high emittance. For both layers the emittance of the anodized surface decreases below the required $\epsilon = 0.7$ after the 600 and 1000 °C nitrogen exposures.

8.6.3 Alternative Heat Shield Materials

An almost infinite number of composite materials, metallic alloys, ceramics, and glasses, together with their numerous

oxidation and heat-resistant coatings, have potential TPS applications. As previously described, some very suitable materials have been developed and are in use today. However, others are being evaluated for future applications such as those needed for future space transportation vehicles and spaceplanes where surfaces will reach 1600 °C. Heat shields such as ceramic tiles may be attached to these spacecrafts' structural materials in order to provide for protection during descent phases of a mission but, for future designs, the outer skin structure will also need to be also resistant to this environment. The following materials are presently identified for structural applications in the various high-temperature ranges:

1000–1600 °C	Carbon–carbon composites, also with active cooling; these include carbon felts (e.g. Calcarb, a rigid felt developed in Ireland; Carbone Lorraine, a flexible felt made in France, and Aerospatial's AQ 61)—limitations apply owing to oxidizing properties, but in space these materials have excellent outgassing characteristics
700–1000 °C	Carbon–silicon carbide composites, also with coatings, and compacted silica powder (e.g. Microtherm, manufactured in the UK by the Micropore Company)
400–700 °C	Titanium aluminides and high-temperature titanium alloys such as

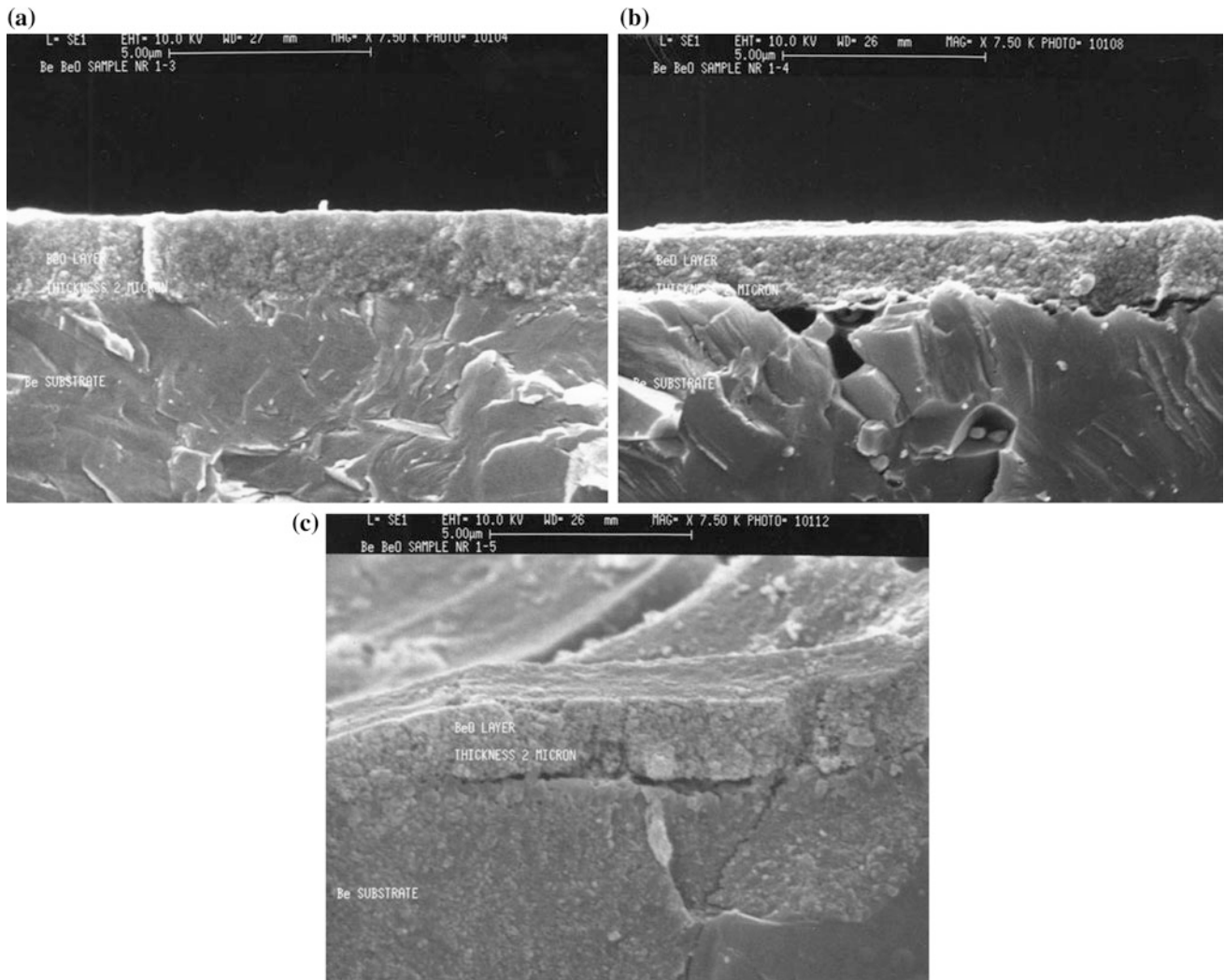


Fig. 8.28 Anodized beryllium, thin (2 μm) coating, showing fractured sections after: **a** 200 thermal cycles (-150 to $+100$ $^{\circ}\text{C}$), **b** thermal cycling plus 600 $^{\circ}\text{C}$ nitrogen exposure/8 h, and **c** all exposures, plus 1000 $^{\circ}\text{C}$ nitrogen/8 h and salt spray/192 h

IMI 834 and Ti 1100 with special coatings
less than 400 $^{\circ}\text{C}$ Conventional metal alloys, oxide-dispersion-strengthened aluminium alloys, carbon fibre reinforced plastics, etc.

Two concepts for the oxidation protection of ceramic matrix composites are shown in Fig. 8.30. The carbon fibres are encapsulated in a matrix of silicon carbide that is introduced by processes involving liquid phase infiltration and/or chemical vapour infiltration.

For external oxidation protection, the multicomponent oxidation protection (or thermoviscous external oxidation coating) was developed in Europe for the Hermes spaceplane. It has an effective operational temperature range from 500 to 1600 $^{\circ}\text{C}$, a proven reparability, and utilizes relatively inexpensive materials and processes that can be readily

industrialized. The disadvantages of this system are that the thermoviscosity of the coating does not permit for very high mechanical clamping stresses at fixation points, or for extremely high pressures of gas flow. The internal oxidation protection system illustrated in Fig. 8.30 has been developed and tested. Initially, the C/SiC material with an outer coating of chemical vapour deposited SiC was tested in static oxidation tests (Lamouroux et al. 1994)—that was without the internal oxidation protection. The results were encouraging, but more recently a great improvement has been achieved when the matrix composition was modified to contain an internal oxidation protection formulation. This formulation consists of a glass sealing agent (having a good wetting to the carbon fibres and the silicon carbide matrix, and a low gas pressure under vacuum at high temperatures), an oxygen getter, and refractory particles.

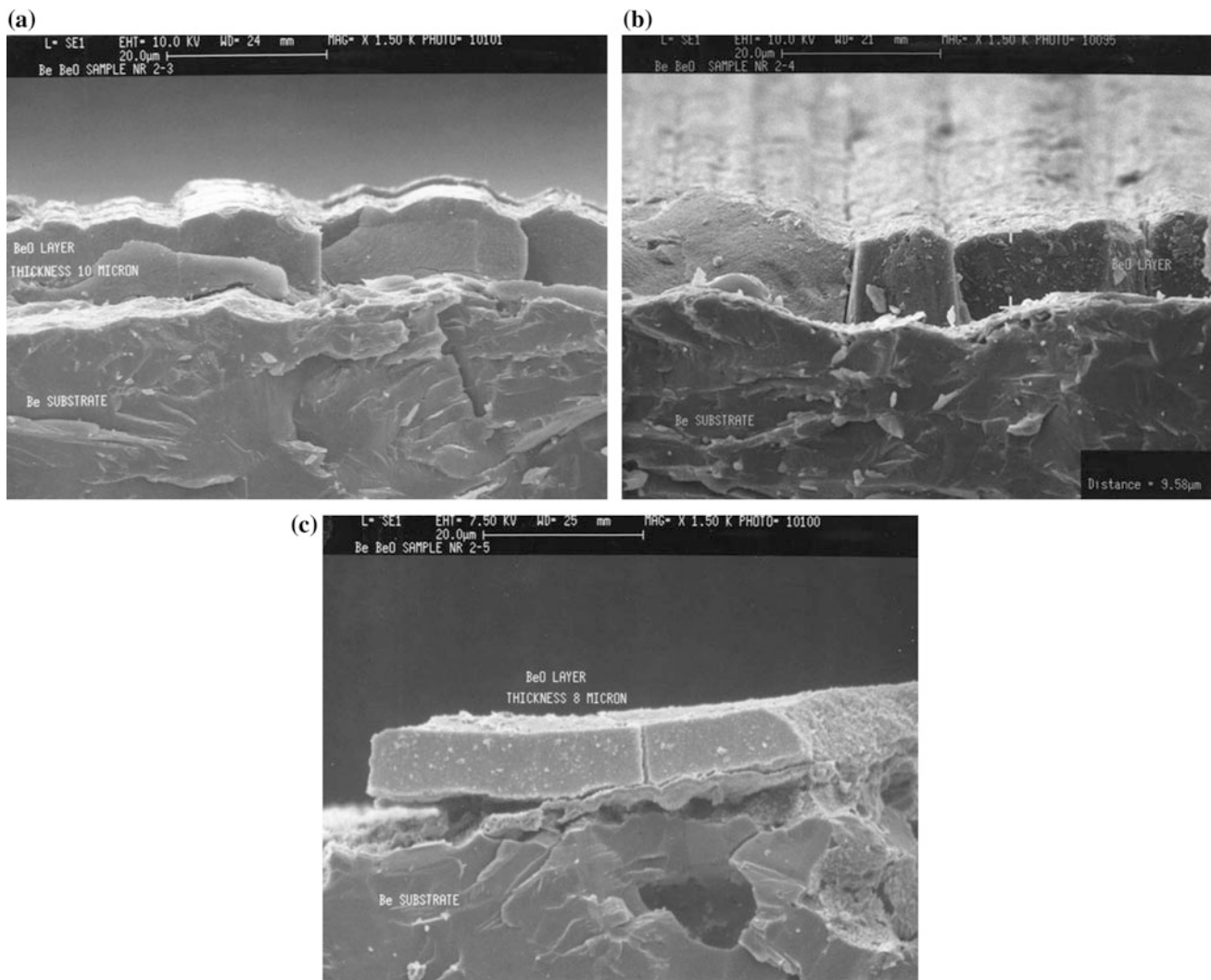


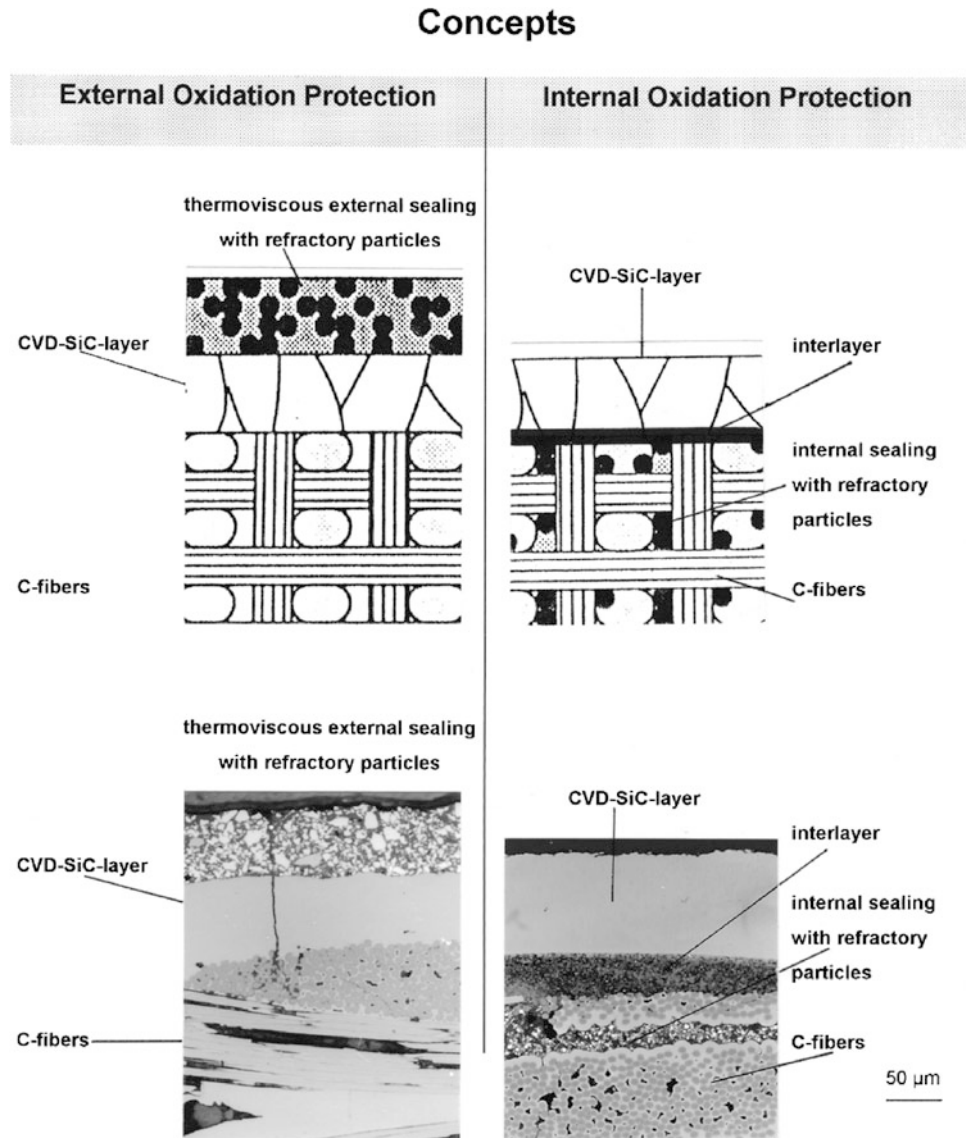
Fig. 8.29 Anodized beryllium, thick (8–10 μm) coating, showing fractured sections after: **a** 200 thermal cycles (-150 to $+100$ $^{\circ}\text{C}$), **b** thermal cycling plus 600 $^{\circ}\text{C}$ nitrogen exposure/8 h, and **c** all exposures, plus 1000 $^{\circ}\text{C}$ nitrogen/8 h and salt spray/192 h

8.6.4 High-Temperature Fasteners

Adhesive compounds are available to secure heat shield elements onto spacecraft outer structures. The Shuttle tiles were described in Sect. 2.4 and the fact that on re-entry the outer skin of this vehicle is forced to bend owing to aerodynamic pressure and, in part, to the differential heating rates and enormously high temperatures seen by the tiles themselves. Silicone adhesives such as RTV 560 are used to bond the ceramic tiles onto the aluminium skin structure, as this adhesive can flex and absorb most dimensional mismatches. In many applications, high-temperature fasteners will be required for the attachment and disassembly of spacecraft parts including those associated with rigid external insulation (hot outer shell elements), ceramic heat shields, hot metallic structures, and items connected to propulsion systems.

Wherever possible the designer will use graphite- and ceramic-based fasteners for these fixations, but screws, bolts, and nuts made of these materials are very difficult to manufacture and procure. Also, they can only be used once and need to be drilled free unless in the particular application it is possible to apply a suitable lubricant. The ceramic matrix material described at the end of Sect. 8.6.3, and illustrated in Fig. 8.30, is being developed for fastener applications. Bolts and nuts (size KM 8) have been fabricated from C/SiC material with coatings of SiC. Test programmes utilized these fasteners (they were coated with the additional external oxidation protection layer seen in Fig. 8.30) to mechanically hold boreholed atmospheric re-entry demonstrator plates for long periods at 1600 $^{\circ}\text{C}$ in air. Under these conditions the fasteners survived a maximum load of 9.75 kN. Similar bolts are now being fabricated with enhanced internal oxidation protection, as drawn in Fig. 8.31.

Fig. 8.30 Methods for protecting ceramic matrix composites from oxidation (Courtesy of MAN Technologie, Germany)



Metallic fasteners may be more suitable than the graphite or ceramic fasteners for applications where there are specific demands for ductility, thermal shock resistance, repeatable joining, or electrical and thermal conductivity. This may be important during the integration of heat exchangers, propulsion system parts, and heat shields. The most common high-strength spacecraft fastener materials are listed in Table 5.1 and described in Sect. 5.4, but for general spacecraft applications even the most advanced alloy (Waspaloy) has a maximum service temperature of only 800 °C.

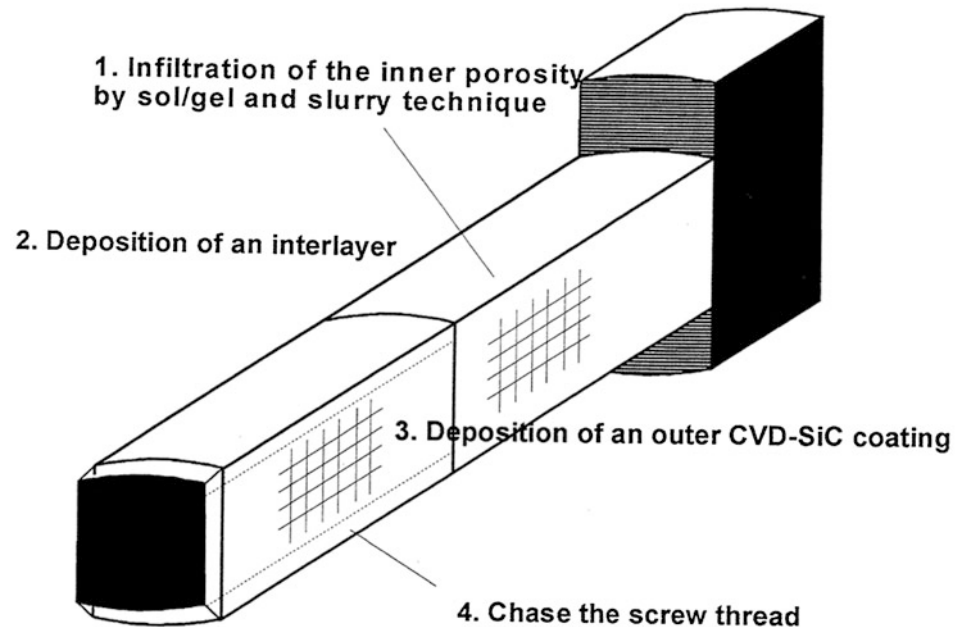
When the Periodic Table is consulted, it is noticed that there are 15 metallic elements with sufficiently high melting points (over 1700 °C) for the very-high-temperature applications required by the space industry (Lupton 1990). Some have been referred to in earlier chapters with respect to their use in electron tubes. Zirconium and vanadium have to be excluded owing to poor high-temperature strength, and

osmium is seriously toxic. The remaining twelve metals can be placed into three classes, described as ‘the refractory metals’ (hafnium, niobium, tantalum, chromium, molybdenum, and tungsten), ‘rhenium’ from the 7th group in the Periodic Table, and ‘the platinum group metals’ (platinum, ruthenium, rhodium, palladium, and iridium). Oxidation resistance is the most important characteristic which differentiates the three classes. Most refractory metals react strongly with oxygen at elevated temperatures and then become severely embrittled at room temperature—however, chromium, molybdenum, and tungsten have volatile oxides and they generally lose section thickness. Rhenium is similar to, but slightly more favourable than, tungsten. The platinum group of metals is usually highly resistant to oxidation but is costly, and has a low strength at temperatures greater than 1100 °C. These strengths can be increased by alloying, and artificial hardening is possible by means of adding a fine

Fig. 8.31 Concept for the enhanced oxidation protection of ceramic matrix composite fasteners (Courtesy of MAN Technologie, Germany)

Internal Oxidation Protection

Concept for the oxidation protection of CMC-fastener



dispersion of a thermodynamically stable oxide phase (e.g. zirconium oxide) to alloys based on platinum and rhodium (Selman et al. 1974; Lupton 1990).

Metallic fasteners for applications in the region of 1600 °C have been produced from the refractory metals, particularly those based on niobium (sometimes called columbium). Data exist for alloys Nb-752, Mo41Re, and Ta10 W. Oxidation-protection coatings are essential for these alloys and several have been developed including silicides (e.g. Si₂₀Cr₂₀Fe and Si-Cr-Ti), aluminides (e.g. Al₁₄₀Si and Al-Si-Ti), and noble metals such as platinum and iridium. An example of one fastener design is shown in Fig. 8.32. Coating thicknesses may range from 20 to 200 μm, depending on the application, and may be applied by physical vapour deposition, plasma spraying, pack cementation, and slurry deposition. Loss of ductility resulting in catastrophic failure may occur if local flaws exist in the oxidation-protection coating. Processing techniques and nondestructive testing for these types of fastener have been refined up to a point where coating defects can be eliminated. However, it is important to apply stringent assembly rules that avoid damage to the coatings from either careless

handling or local stressing by the edges, corners, and recesses of materials being joined. Although the oxidation resistance of assembled Nb-752 fasteners (coated) has been successfully demonstrated, it is noted that shear forces between screw and nut must be minimized, and this requires special assembly techniques.

8.7 Manned Compartments

8.7.1 General Conditions

Human beings' quest to live in space began in 1961, with the first orbital flight of Soviet cosmonaut Yuri Gagarin in the Vostok 1 spacecraft. Later in the 1960s, the US Mercury and Gemini programmes developed manned spaceflight, and these were followed by the Apollo programme that culminated with several landings on the Moon. Skylab was the first American space station; it was launched in 1973 and visited by three sets of astronauts for periods of up to 84 days. Soviet cosmonauts stayed in space for even longer periods during the Salyut-6 and Mir space station missions

Fig. 8.32 Silicide-coated fasteners developed for assembly of the Thermal Protection System of re-entry vehicles. These oxidation-protected fasteners are machined from niobium alloy 752. After machining (1) the parts are coated with SiCrFe and annealed (2). The arrow at (3) shows the pre-oxidized deliverable finish. These fasteners have been tested at elevated temperatures and do not degrade in mechanical properties following exposure in air to 1150 °C for more than 500 h. They also survive temperature cycling to 1300 °C for 40 h (Courtesy of Plansee Aktiengesellschaft)



(longer than one year). This clearly demonstrated that with supplies of air, food, and water, people can function effectively in space for long periods in order to perform useful experiments, observations, and services for those of us who must remain on Earth. In the former Space Shuttle era, the human role has taken advantage of the lessons learnt by the early manned flights into space. Although not designed for permanent presence in space, it was regrettable that the Skylab space station was unceremoniously dumped into the Indian Ocean (and parts of Australia) because delays at the beginning of the Shuttle programme prevented a refurbishment mission. However, the Russian Mir space station, launched in 1986, did prove to be an extremely durable vehicle owing to its design innovations which include a five-port docking adapter onto which can be attached additional laboratory modules (see Fig. 8.33). This legend proved Russia to be a leader in space technology as Mir endured 15 years in orbit, three times its planned lifetime. By the time the International Space Station *Alpha* (Fig. 3.1) was launched and operational around 2003, Mir was still demonstrating its usefulness by some forms of low-cost extended missions. The European-built Spacelab has flown on many missions inside Space Shuttle cargo bays since 1983. After several refurbishments and reconfigurations with new equipment and experiments, detailed inspection of the interior structure of the fourteen-year-old Spacelab (see Fig. 3.2) shows no sign of degradation.

The success of the existing space station and laboratory projects has been, in part, due to the importance that was

given to the proper selection of materials and processes during the design and fabrication stages of these spacecraft. Some considerations are familiar to those engineers who have designed or lived in confined volumes, such as submarines! Past experience has been accumulated by the various space agencies and this has formed the basis for establishing acceptable requirements. The majority of the metallic materials and the manufacturing processes that were selected for fabricating both manned and unmanned spacecraft have been touched on between the covers of this book. There are though, specific problems that might occur within manned spacecraft—the main ones being highlighted in Fig. 8.34—and these can only be avoided by additional requirements. Chapters 2 and 3 detailed the main product assurance requirements set by the space agencies to cover general spacecraft materials and processes. An excellent overview of the technical issues related to materials safety for manned space have been documented by Pedley (2009). For manned vehicles, some of the additional safety requirements relate to:

- Structural design providing ultimate factors of safety equal to or greater than 1.40; and, primary structures and support bracketry precludes failure by the propagation of pre-existing flaws based on fracture control; special design burst pressure levels for pressure vessels
- Metallic materials being resistant to cracking due to stress corrosion (i.e. select from the alloys listed in Table 2.2)

Fig. 8.33 **a** Photograph of the Russian Space Agency's Mir space station docked to the Space Shuttle Atlantis in June 1995. **b** Mir station taken at the time of the EuroMir mission in 1996 (the ESA astronaut Thomas Reiter became the first non-Russian astronaut to spend 180 days on-board)

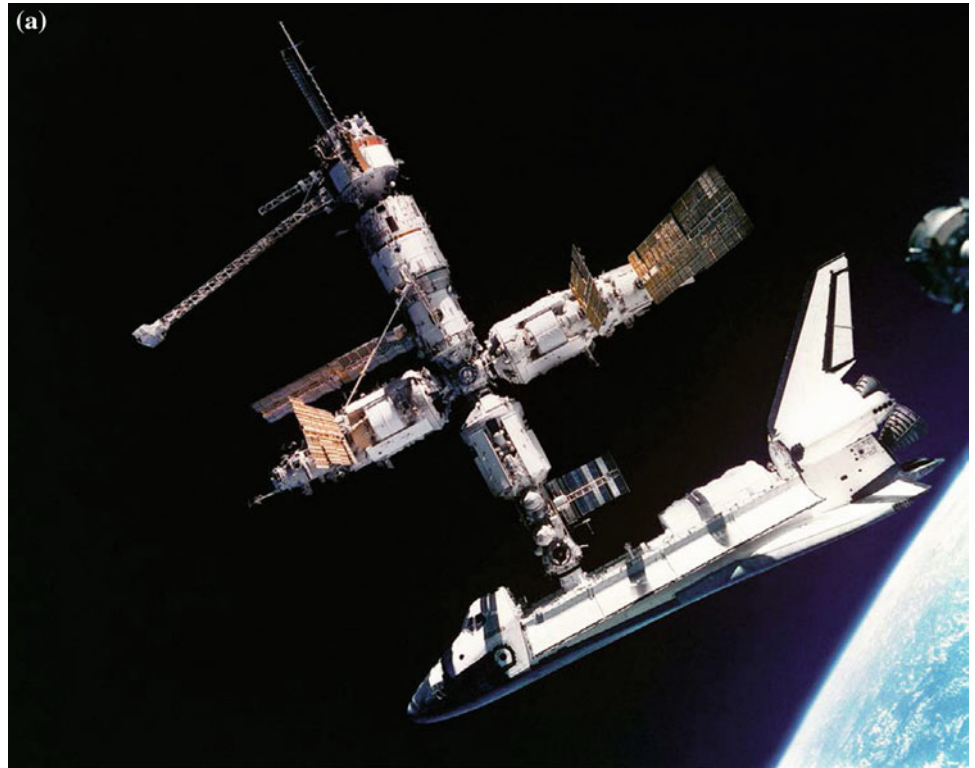
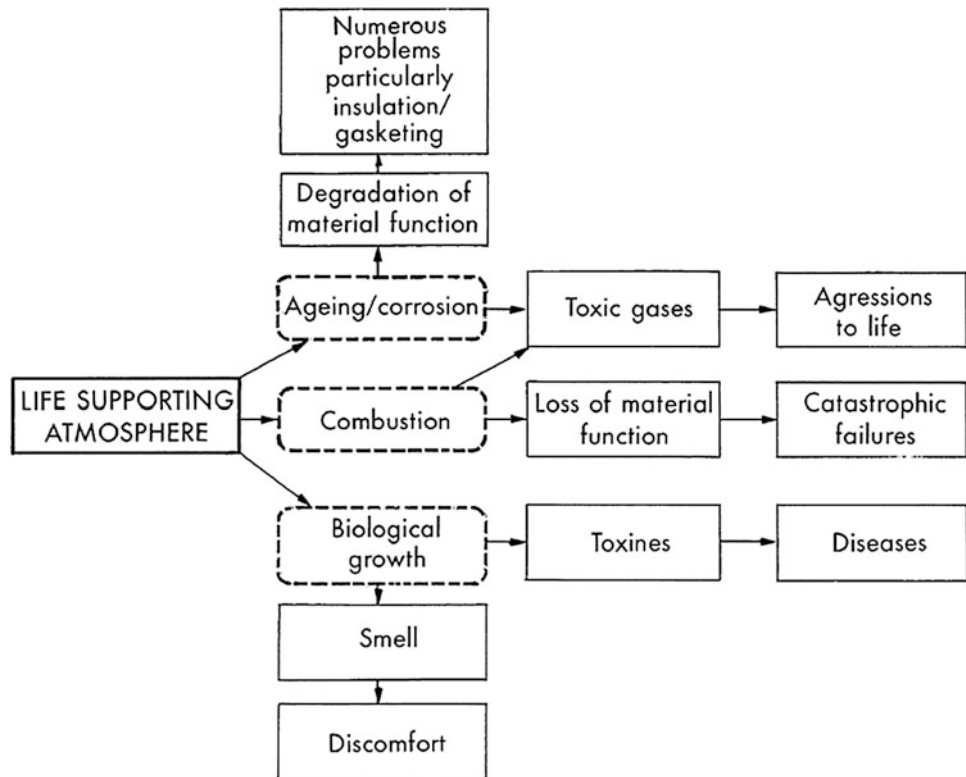


Fig. 8.34 Space environmental effects: manned volumes



- Propellant compatibility
- Oxygen compatibility
- Avoidance of hazardous materials, including radioactive metals, beryllium (toxicity problems if scraped), and mercury (as this liquid metal, when spilt, can penetrate the aluminium alloy walls of the vehicle causing leakage of the atmosphere)
- Nonmetallic materials being controlled for flammability, toxicity, and odour (they will therefore have low off-gassing properties). They need to resist moisture and fungal growth.

From a European viewpoint, the metallic materials that were selected for projects associated with manned spacecraft requirements (i.e. Spacelab and its on-board experimental apparatus, for Eureka, Hubble Space Telescope, etc.) have functioned correctly without any problems related to safety and reliability (Dricot et al. 1994). A short list of Preferred Materials that was compiled for the *Columbus* project in 1994 enabling a check to be made concerning the number and extent of materials tests that were, at that time, still outstanding has been reproduced in Table 8.3.

8.7.2 Solder Assembly Defects

Occasionally, equipment associated with Spacelab experiments has failed during flight. When it can be demonstrated that the potential failure of experiments will not be life-threatening or a danger to the space mission, some of the specific materials and processes requirements for manned projects may be waived. This can achieve cost reductions for universities, and the like. It can also cause the early curtailment of an interesting in-orbit investigation.

One recent equipment failure involved a video camera that was being used to record a fluid dynamics experiment. The liquid under evaluation in zero gravity was made up of 95 % French tap water mixed with 5 % Ajax washing solution (one of several candidates being considered as an aqueous film-forming foam (AFFF), for the suppression of fires in the *Columbus* module). An astronaut was filming the morphological changes that occur under zero-g, when small droplets of water and foam were injected into an orbit space laboratory. Soon after commencing the experiment, the video camera suddenly stopped functioning. A few small globules of water had made contact and intruded into the camera.

Table 8.3 First list of preferred materials for short-term evaluation

Sample	Material identification	F1	Tox	Odor	Mbio	Tdec	Fow	Corr	SCC	Arc T	Outg	Tcyc	UV	Atox	FL21
0101	AA 1100	N/A	N/A	N/A	T	N/A	N/A	A	A	N/A	N/A	N/A	N/A	N/A	N/A
0102	AA 2024-T81 (bar, rod)	N/A	N/A	N/A	T	N/A	N/A	A	A	N/A	N/A	N/A	N/A	E	N/A
0103	3.3214-T6 (6061-T6)	N/A	N/A	N/A	T	N/A	N/A	A	A	N/A	N/A	N/A	N/A	E	N/A
0104	3.4364-T7351 (7075-T73)	N/A	N/A	N/A	T	N/A	N/A	A	A	N/A	N/A	N/A	N/A	E	N/A
0105	AA 2219-T81	N/A	N/A	N/A	T	N/A	N/A	A	A	N/A	N/A	N/A	N/A	E	N/A
0302	INCONEL 718-PH	N/A	N/A	N/A	T	N/A	N/A	A	A	N/A	N/A	N/A	N/A	E	N/A
0401	3.7164.1	N/A	N/A	N/A	T	N/A	N/A	A	A	N/A	N/A	N/A	N/A	E	N/A
0402	3.7164.7	N/A	N/A	N/A	N/A	N/A	N/A	A	A	N/A	N/A	N/A	N/A	N/A	N/A
0602	AISI 304L Cond. A	N/A	N/A	N/A	T	N/A	N/A	A	A	N/A	N/A	N/A	N/A	E	N/A
0603	AISI 316 Cond. A	N/A	N/A	N/A	T	N/A	N/A	A	A	N/A	N/A	N/A	N/A	N/A	N/A
0604	AISI 347 Cond. A	N/A	N/A	N/A	T	N/A	N/A	A	A	N/A	N/A	N/A	N/A	N/A	N/A
0606	1.4944.9 (A 286 SH)	N/A	N/A	N/A	T	N/A	N/A	A	A	N/A	N/A	N/A	N/A	E	N/A
0607	17-7 PH-CH 900	N/A	N/A	N/A	T	N/A	N/A	A	A	N/A	N/A	N/A	N/A	N/A	N/A
1001	ARALDIT AV138/HV998	A	A	A	T	N/A	N/A	N/A	N/A	N/A	A	N/A	N/A	E	N/A
1002	ECCOBOND 57C/9	T	T	T	T	T	N/A	N/A	N/A	N/A	A	E	N/A	E	N/A
1003	RTV-S 691	T	T	T	T	T	N/A	N/A	N/A	N/A	A	A	A	E	A
1004	SCOTCH-WELD 2216 B/A	A	A	A	T	T	N/A	N/A	N/A	N/A	A	E	N/A	E	N/A
1005	PARYLENE C	A	A	A	T	T	N/A	N/A	N/A	N/A	A	N/A	N/A	N/A	N/A
1101	G410810	N/A	A	A	N/A	N/A	N/A	N/A	N/A	N/A	A	E	E	E	A
1102	SCOTCH Y-966	T	A	A	N/A	N/A	N/A	N/A	N/A	N/A	A	A	N/A	E	A
1103	TESAMETAL 4500 Silver	T	T	T	T	N/A	N/A	N/A	N/A	N/A	A	E	N/A	E	N/A
1104	MYSTIC 7367	T	T	T	T	T	N/A	N/A	N/A	N/A	A	E	E	E	A
1201	CHEMGLAZE Z306	A	A	A	N/A	N/A	N/A	N/A	N/A	N/A	A	A	E	E	N/A
1202	ELECTRODAG +501	A	N/A	N/A	N/A	N/A	N/A	N/A	N/A	N/A	A	A	A	E	A
1203	PYROLAC PSG 120 FD	A	N/A	N/A	N/A	N/A	N/A	N/A	N/A	N/A	A	A	E	E	A
1204	ALEXIT 406-23 104 G	T	A	A	T	T	N/A	N/A	N/A	N/A	A	N/A	N/A	N/A	N/A
1301	BRAYCO 815 Z	A	A	A	T	T	N/A	N/A	N/A	N/A	A	N/A	N/A	N/A	N/A
1302	BRAYCOAT 601	A	A	A	T	T	N/A	N/A	N/A	N/A	A	N/A	N/A	N/A	N/A
1303	BRAYCOAT 602	N/A	N/A	N/A	T	T	N/A	N/A	N/A	N/A	N/A	N/A	N/A	N/A	N/A
1304	TIO-LUBE 460	A	A	A	T	N/A	N/A	N/A	N/A	N/A	A	E	N/A	E	N/A
1401	ECCOSIL 4952/50	A	A	A	T	T	N/A	N/A	N/A	N/A	A	N/A	N/A	N/A	A
1402	ECCOFOAM FPH/12-2 H	A	A	A	T	T	N/A	N/A	N/A	N/A	A	N/A	N/A	N/A	N/A
1501	CHO-THERM 1671	A	A	T	T	T	N/A	N/A	N/A	N/A	A	E	N/A	N/A	N/A
1503	MXB-6001/1581	T	T	T	T	N/A	N/A	N/A	N/A	N/A	T	E	E	E	N/A
1504	BETA CLOTH X 389-7	A	A	A	N/A	N/A	N/A	N/A	N/A	N/A	A	E	E	E	A
1505	GUDE SPACE 18 DPTH	A	A	A	T	T	N/A	N/A	N/A	N/A	A	N/A	N/A	N/A	N/A
1506	DURA VER-E-Cu 104 (FR4)	A	T	T	T	T	N/A	N/A	N/A	N/A	A	N/A	N/A	N/A	N/A
1507	FLEXAFIT SG 2212	A	A	A	T	N/A	N/A	N/A	N/A	N/A	N/A	N/A	N/A	N/A	N/A
1601	VITON B	A	A	A	T	T	N/A	N/A	N/A	N/A	A	E	E	E	N/A
1602	5 SL 1617	T	T	T	T	N/A	N/A	N/A	N/A	N/A	A	N/A	N/A	N/A	N/A
1701	DACRON B 4 A	A	A	A	N/A	N/A	N/A	N/A	N/A	N/A	A	E	N/A	E	N/A
1702	PTFE 9900/0100	A	A	N/A	T	T	N/A	N/A	N/A	N/A	A	E	E	E	A
1703	THERMOFIT KYNAR	A	A	A	T	T	N/A	N/A	N/A	N/A	A	N/A	N/A	N/A	A
1704	INSULITITE HFT-A Blue	T	A	T	T	T	N/A	N/A	N/A	N/A	A	N/A	N/A	N/A	A
1705	TY RAP TYZ 28 M	A	A	A	T	T	N/A	N/A	N/A	N/A	A	N/A	N/A	N/A	N/A
1901	Wire type: 1871	T	T	T	T	T	T	N/A	N/A	T	A	N/A	(A)	N/A	(A)
1902	Wire type: 3901/002	T	T	T	T	T	T	N/A	N/A	T	A	N/A	(A)	N/A	(A)
1903	Wire type: 3901/1	T	T	T	T	T	T	N/A	N/A	T	A	N/A	(A)	N/A	(A)
1904	Wire type: 3901/2	T	T	T	T	T	T	N/A	N/A	T	A	N/A	(A)	N/A	(A)
1908	Wire type: SPA 2110	T	T	T	T	T	T	N/A	N/A	T	A	N/A	(A)	N/A	(A)

(continued)

Table 8.3 (continued)

1909	Wire type: SPB 2110	T	T	T	T	T	T	N/A	N/A	T	A	N/A	(A)	N/A	(A)
1910	Wire type: SPC 2110	T	T	T	T	T	T	N/A	N/A	T	A	N/A	(A)	N/A	(A)
1911	Wire type: MTV-BTV	T	T	T	T	T	T	N/A	N/A	T	A	N/A	(A)	N/A	(A)
1912	Coax Cable: 50 CIS	T	T	T	T	T	T	N/A	N/A	N/A	A	N/A	(A)	N/A	(A)
1913	Coax Cable: R 59	T	T	T	T	T	T	N/A	N/A	N/A	T	N/A	(A)	N/A	N/A
1914	Wire type: 1872	T	T	T	T	T	T	N/A	N/A	T	A	N/A	(A)	N/A	N/A
1915	Wire type: 3901/001	T	T	T	T	T	T	N/A	N/A	T	T	N/A	(A)	N/A	N/A
<i>Tests</i>								<i>Test houses</i>			<i>Ratings</i>				
Fl:	Flammability 24.5 % O ₂	SCC:		Stress-corrosion cracking		C:	DCN (CERTISM)		T:	To be tested					
Tox:	Toxicity	ArcT:		Arc-tracking		D:	DERTS		N/A:	Not applicable					
Odor:	Odour	Outg:		Outgassing		E:	DASA-RIT		A:	Test data available					
Mbio:	Microbial resistance	Tcyc:		Thermal cycling		S:	SINTEF		(A):	Tested per ESA space components spec.					
Tdec:	Thennal decomposition	UV:		Ultraviolet radiation					E:	Evaluation					
Fow:	Flammability of wires	Atox:		Atomic oxygen											
Corr:	Corrosion	F121:		Flammability 21 % O ₂											

A metallurgical investigation was performed on the video camera six weeks after the failure event. A summary of the findings is as follows:

- the black plastic video camera case was not hermetically sealed and there were many places where liquid could penetrate
- close inspection showed that not all of the assembled components were covered with a very thin layer of conformal coating; some of the noncoated regions of the assembly had corroded (as shown on Fig. 8.35)
- the residues from liquid solder flux were present adjacent to many solder joints
- one typical region that supported corrosion products was photographed at a high magnification (as shown in Fig. 8.36 in the colour section), the voluminous products having characteristic colours: red, blue-green and white
- the distinct corrosion products were carefully removed from the board and chemically analysed by energy-dispersive X-ray analysis.
- the results are given in Figs. 8.37, 8.38 and 8.39, white deposits being mainly lead oxide, blue-green deposits containing copper chloride, and red deposits containing cuprous oxide (chlorides are expected to originate from solder flux, as the AFFF liquid and original French tap water showed no white precipitation when mixed with a solution of silver nitrate—a very sensitive test for chlorides)
- dark, electrically conductive traces (similar to the electrochemical migration illustrated in Figs. 6.30, 6.49 and 6.50) were seen beneath some of the corrosion products, indicating that the camera failure mechanism resulted from the migration of tin between the very small track spacing when the circuit was damp.

It was concluded that this commercial video camera contains design weaknesses that permit the intrusion of liquids. Also, the quality of workmanship fell short of that normally required for space hardware (ECSS-Q-ST-70-38); some line spacings were extremely narrow, the residues of soldering flux had not been removed, and the circuit had not been adequately conformally coated. High humidity and condensation of water onto all internal surfaces, including electronic housings, within manned volumes is always a potential problem. This is due to the fact that life-support systems may not always be able to remove humidity quickly enough from the habitat module or laboratory module, particularly at times when there is a large temperature difference between the walls, floors, and working space within the galleys.

It is interesting to note that the ISS includes a Maintenance Work Area consisting of a portable foldable workbench and tabletop. Astronauts can unfold it anywhere and clamp it to a slotted track—these tracks are located on most of the floor-to-ceiling racks inside station. Many tests have been made related to soldering operations on ISS while orbiting the Earth. These were made during a dedicated work programme in order to check if solder joint repair is feasible inside the manned modules (Flin 2005). The results are fascinating, and can be summarized as follows:

- when rosin-cored solder is applied to the heated tip of a soldering iron the solder becomes molten and clings to the tip, the solder liquid then begins to spin round and round, getting progressively faster.
- In low-gravity surface tension forces are greater than on Earth so soldering processes are more difficult to perform.
- Splatter from liquid solder forms drops held together by surface tension, these float through the air in space and can be hazardous.

Fig. 8.35 Video camera electronics after disassembly. The miniature electronic components are surface mounted onto the facing PCB. Localized regions of corrosion products are present on solder joints and tracks (*arrowed*)

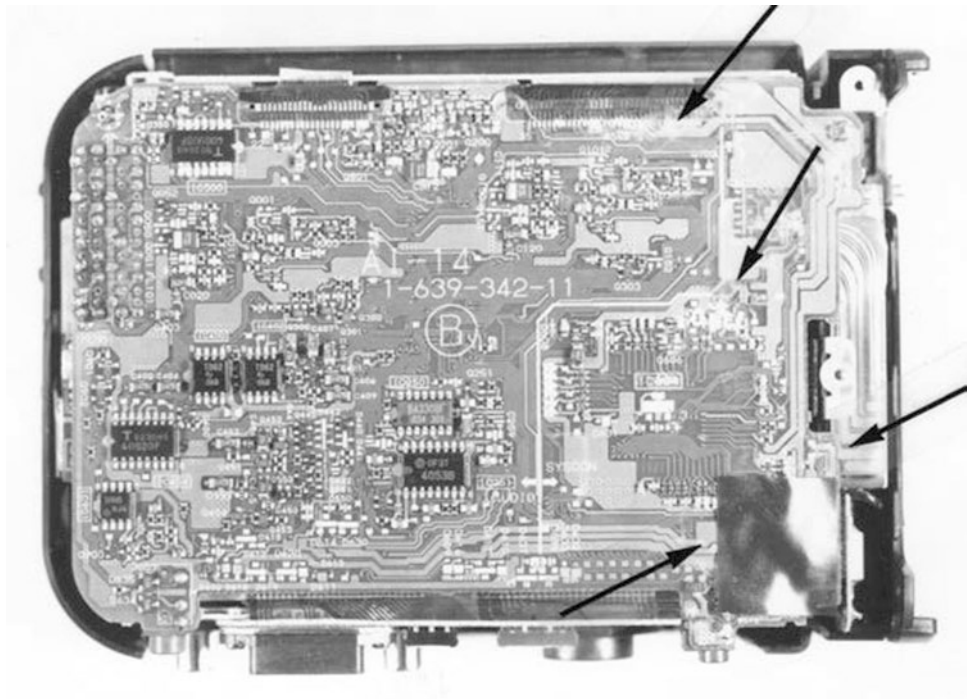
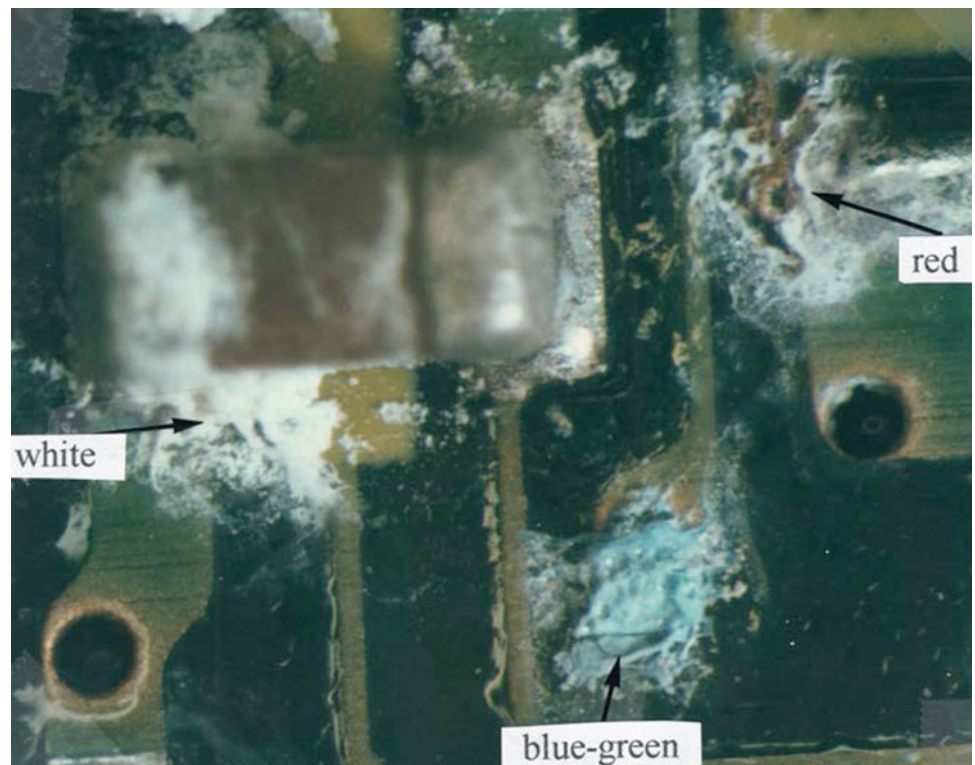


Fig. 8.36 Colour photomicrograph of corrosion products seen on failed video camera electronic circuit (approximately $\times 50$ magnification)



- Low gravity eliminates convection and cooling is initiated at the molten solder surfaces, so entrapping gasses and solder flux and this leads to poor quality joints.
 - Debris from cutting and soldering needs to be captured and disposed of using the station's vacuum cleaner.
 - Smoke created during soldering does not easily disperse, possibly leaving the operator without a good view of the workpiece.
- Clearly soldering and conducting repairs in space is challenging and it may be needed to select conductive

Fig. 8.37 The majority of corrosion product on the circuit board is *white*. EDAX analysis shows this to be mainly lead (oxide) with tin (oxide) originating from attack of the solder joints. Compare with the colour photograph shown in the colour section (Fig. 8.36)

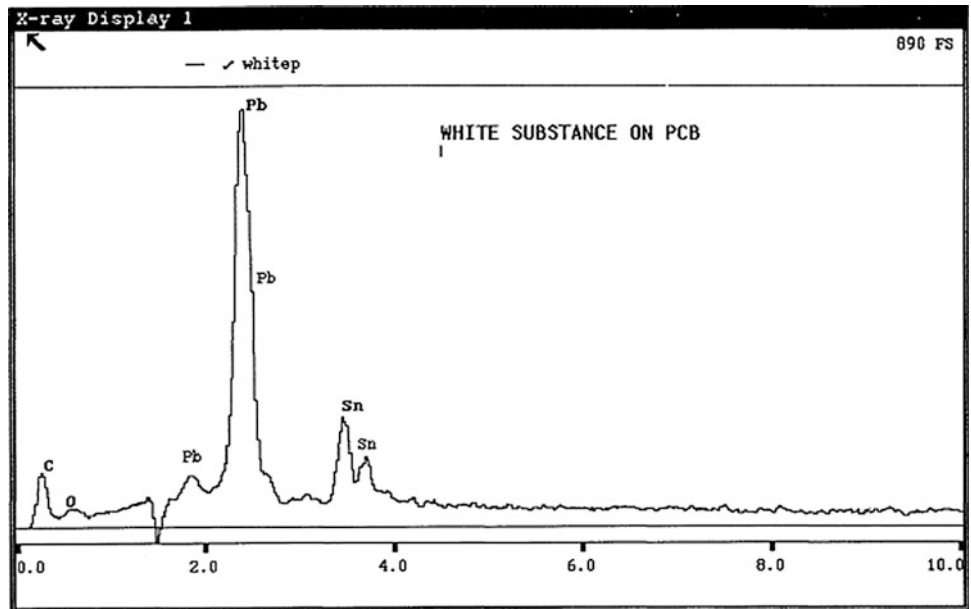
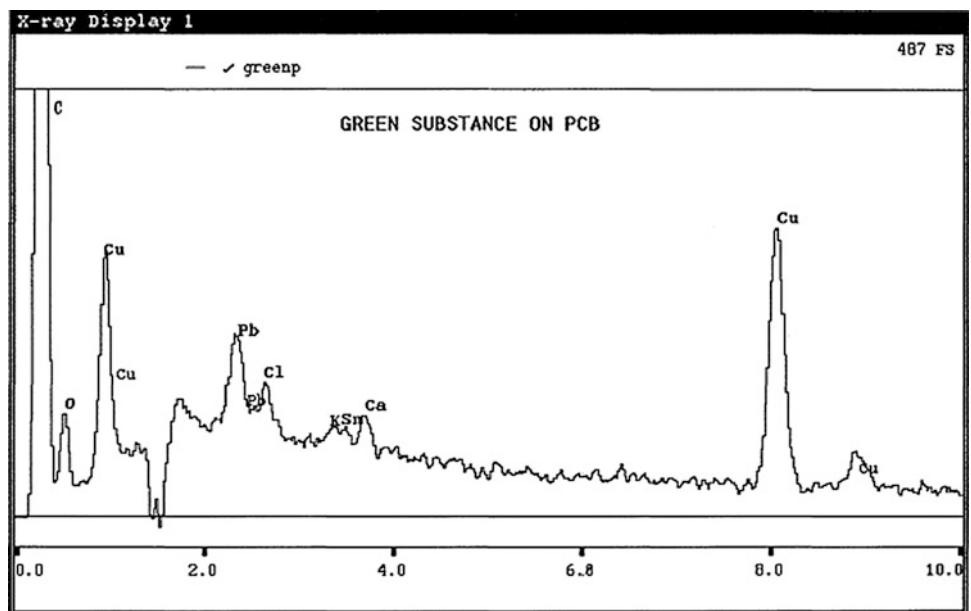


Fig. 8.38 EDAX analysis of green product. This contains mainly copper with associated chlorine, calcium, and lead. This is similar to 'green plague', the reaction product of solder flux with copper oxide (solder flux generally contains chlorine)



adhesives for repair work, despite their inferior properties when compared to traditional soldering (see Sect. 6.13).

8.7.3 Inspection of Spacelab Post-flight Hardware

Spacelab has been one of ESA's most important projects and was a major contribution to the US Space Shuttle

programme. The hardware was manufactured in Europe after long development activities in the fields of materials and processes (M&P). This final section describes the findings of a detailed inspection of the various Spacelab-1 hardware at the Kennedy Space Centre. The inspections were made by the writer in the presence of long-term NASA personnel who had been associated with the day-to-day use and operation of the hardware. The full report and an extensive description of the objectives, methods and findings from this investigation

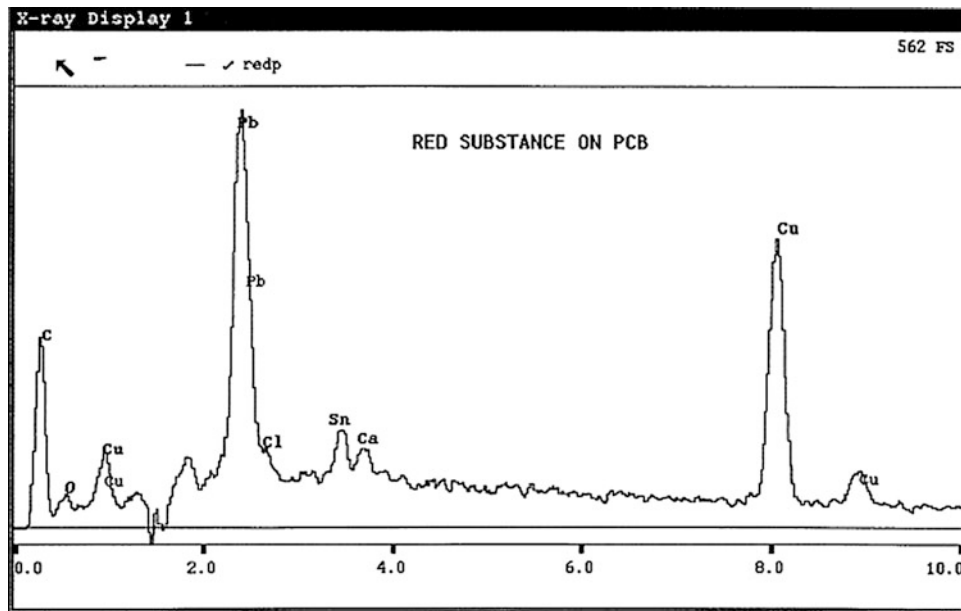


Fig. 8.39 EDAX analysis of *red* product showing much copper and lead. This is similar to 'red plague', the corrosion product of copper to form red cuprous oxide

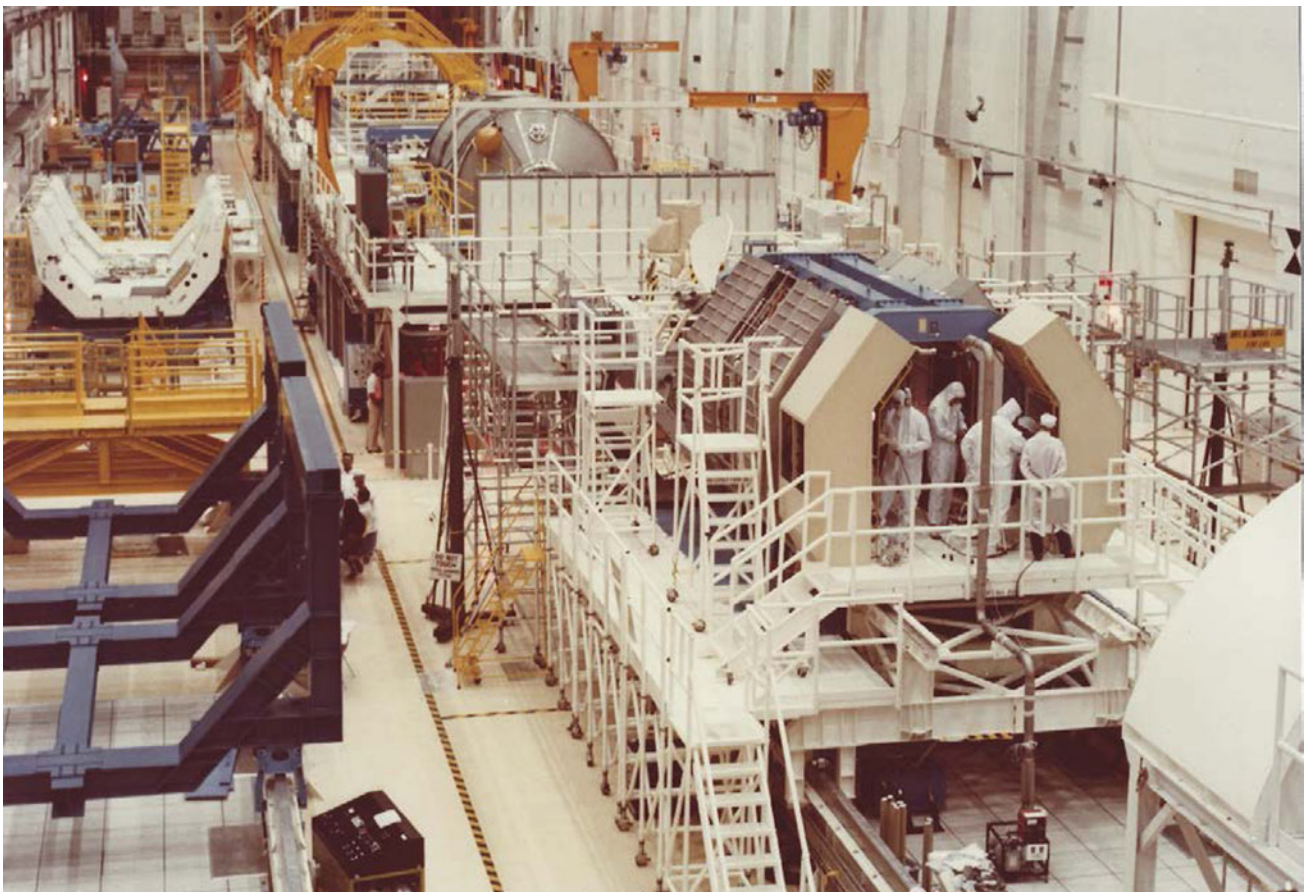


Fig. 8.40 General view of the Spacelab processing and integration area in the "O and C" building at KSC during 1982

Fig. 8.41 Spacelab-1 located in the Shuttle Cargo Bay in-orbit



have been published (Dunn and Stanyon 1997). This end-of-service inspection took place 16 years after Spacelab's integration (Fig. 8.40) and one year after the final in-orbit flight (Fig. 8.41). Spacelab flew on 22 Shuttle missions between 1983 and 1996. Various flight configurations were qualified and flown with the pressurised, habitable laboratory module. The other components were: the Spacelab Pallet, a U-shaped un-pressurised platform onto which were mounted experiments and telescopes having a direct exposure to space; an Instrument Pointing System attached to the Pallets for precise pointing and observation of the Earth and our planetary system; and, a Tunnel connecting the laboratory to the crew compartment of the Shuttle.

The main objective of the inspections was to identify M&P problems which had been experienced and during Spacelab's life, assess their importance and feed this information to the engineers engaged in the selection of materials and processes for future European manned space missions, such as the Columbus module of ISS.

Some problems were identified during the inspection visit, but all-in-all, the post-flight hardware was considered to be in an excellent condition and generally it was the materials known as having a finite shelf- or service-life which had degraded. Documented problems (from non-conformance reports, material review boards, etc.) were made the subject for detailed inspection, they comprised of:

- (a) Corrosion: of the Alodined weld and its heat affected zone, degradation of anodised surfaces and condensation in cold areas.
- (b) Painted surfaces: peeling, flaking, degradation of optical properties, atomic oxygen effects.
- (c) Thermal protection: thermal blanket degradation, wear, tarnishing, etc.
- (d) Interface problems: wear, friction on trunnions and mounting points, fasteners, wear of electrical connectors, fluid disconnect problems, threaded connections, accidental damage (dings) needing added protection.
- (e) Limited life items/physical degradation: seals and associated leak rates, relief valves (positive and negative pressure), brush motor start-up after long periods of non-activity (sticktion), harness attachment points and insulation damage, condensate heat exchanger degradation, evidence of microbial contamination.

The following figures illustrate some of problems listed above—their captions describe in more detail the topographical evidence (Figs. 8.42, 8.43, 8.44, 8.45, 8.46, 8.47, 8.48, 8.49, 8.50, 8.51, 8.52, 8.53, 8.54, 8.55 and 8.56).

Fig. 8.42 The waffle structures and internal walls consist of anodised AA2219-T851, the TIG welded plates are ground, polished and brush Alodined. The brush Alodined weldments **a** show some discolouration, but after inspection of all accessible welds, and at higher magnification, only one “suspect” area **b** was identified and later NDT found this to be tarnish. No areas of corrosion or staining were observed

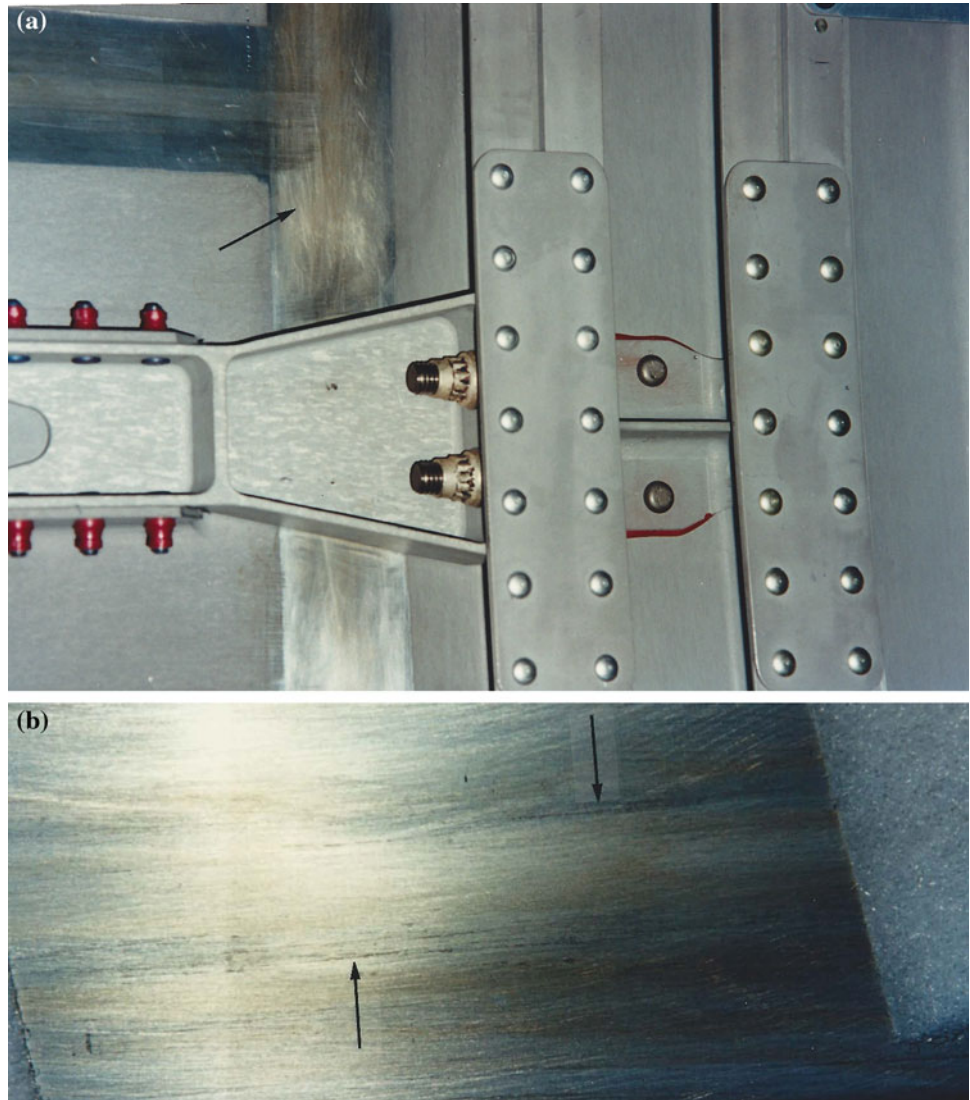


Fig. 8.43 **a** General view of heat exchanger and the right-hand region of corrosion. **b** The corroded aluminium and brown corrosion product appears to result from flux residue

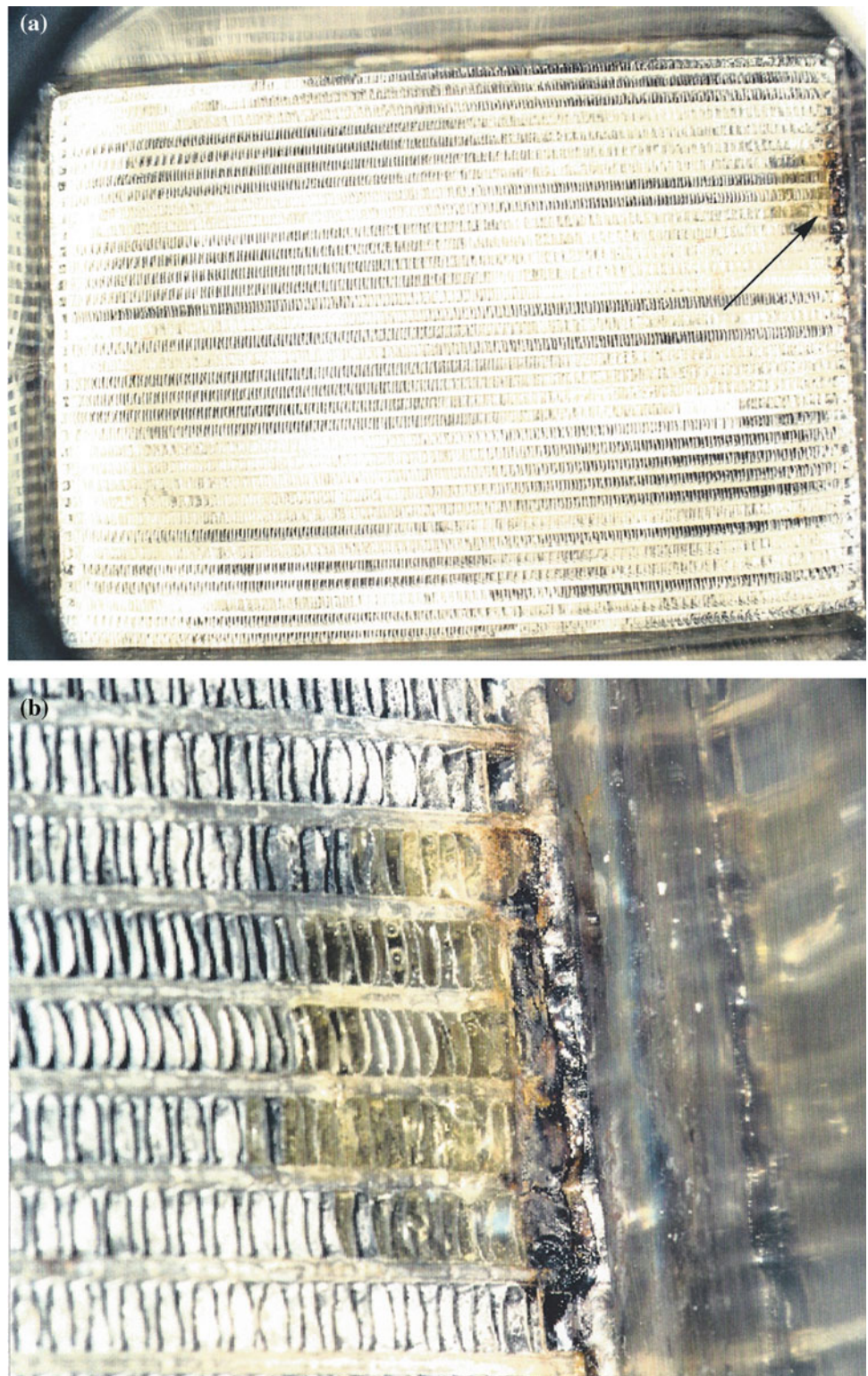


Fig. 8.44 Detail, showing some small areas of Chemglaze white paint removed from rounded corners, indicating the need to check the suitability of the primer. All other areas coated with Chemglaze (also external and on Pallet) were in excellent condition



Fig. 8.45 Solar blankets are undamaged, there is slight darkening of the cloth surrounding ESA logo but none of the colours have altered or become bleached due to the space environmental exposure (radiation and atomic oxygen)

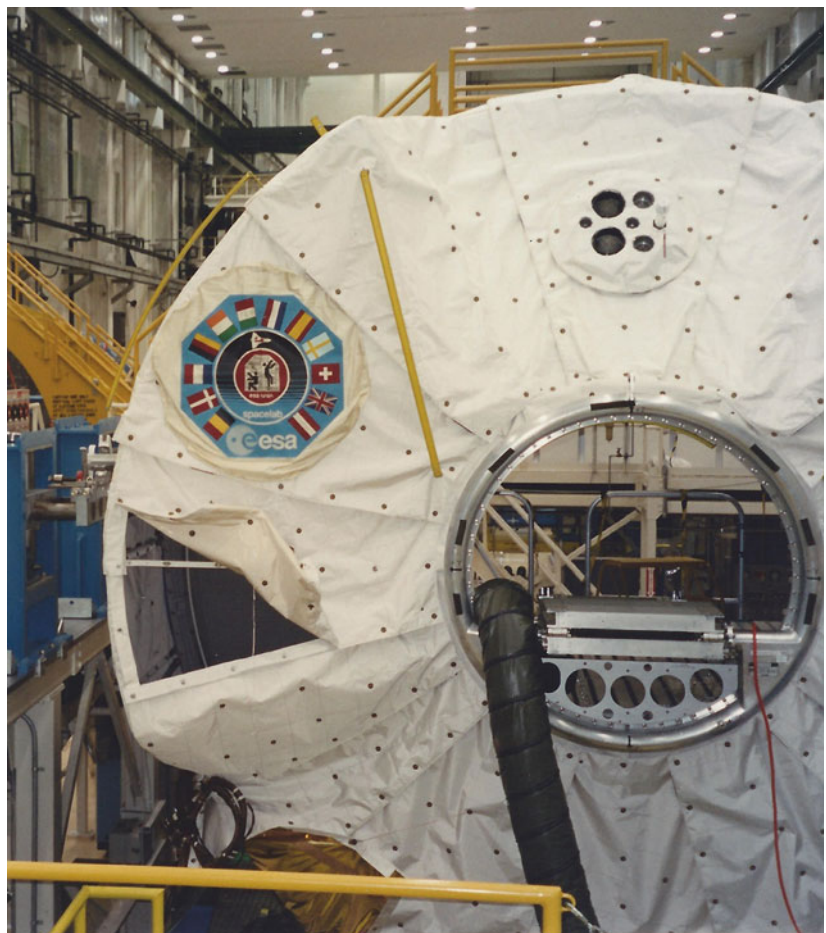


Fig. 8.46 Delamination of the goldized-Kapton thermal blanket is seen in this area and an indication of staining. Only this region, subjected to a small bend radius was damaged. Nomex cloth is now used and the NASA logos painted directly to this material have proven to be resilient to colour degradation in space

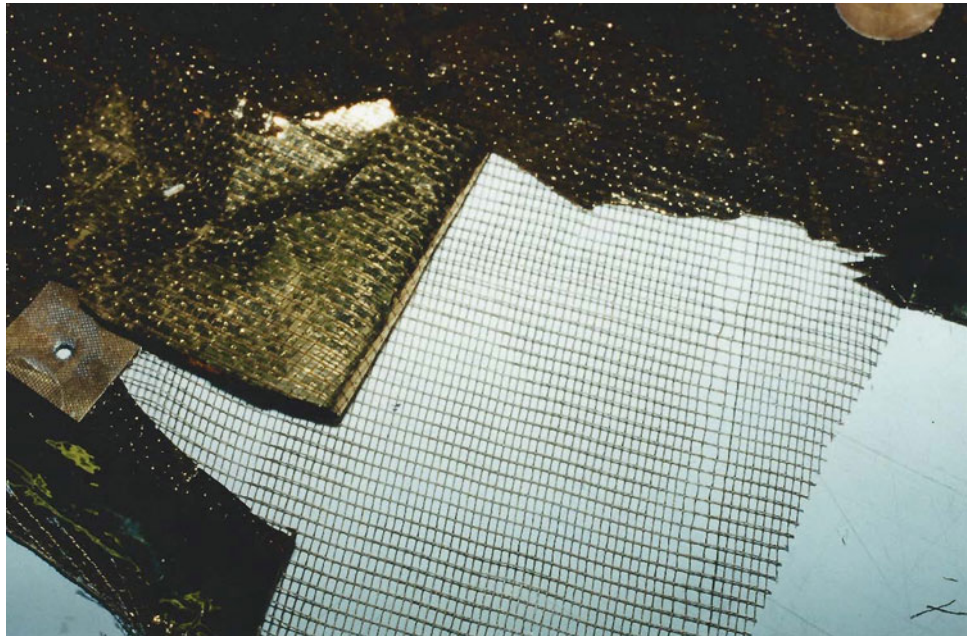


Fig. 8.47 These plastic attachment devices for holding together the blankets have a tendency to pop-off and the plastic ring, shown here, can uncontrollably spring away from the retaining groove of the tubular post (insert) during flight (creating debris)



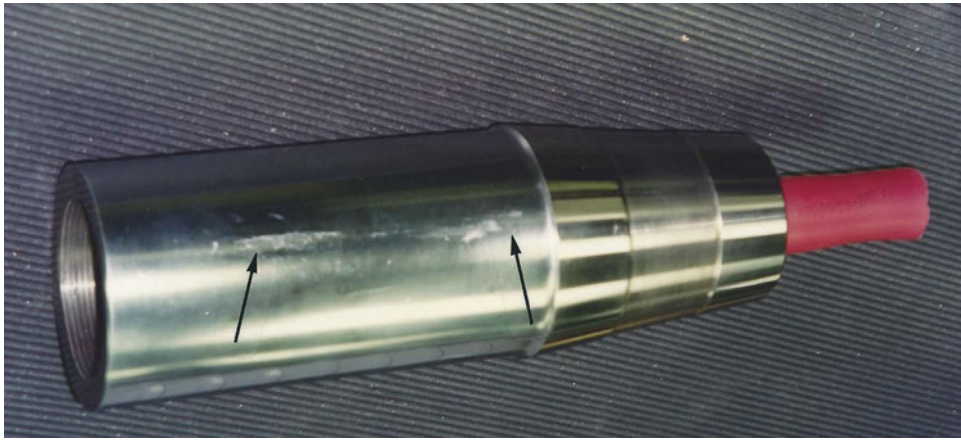


Fig. 8.48 Chromium-plated main module trunnion (approximate diameter 80 mm) removed after flight and ground handling. An extensive deposit of aluminium alloy is seen to adhere to this bearing surface. It was determined to have been transferred from an

aluminium-rich coating on a mounting point; the Al-to-Cr interfacial couple is not a recommended combination as surfaces can cold-weld under the combined effects of vacuum and pressure (see especially Figs. 2.4a and 2.5

Fig. 8.49 The ducting/bellows interface providing cooling to the racks created a problem because the bellows material is very rigid. A more flexible material would make the connection and clamp-securing operations in orbit less difficult and reduce the amount of damage and shred material. Scuffing and wear causes contaminant particles to be released

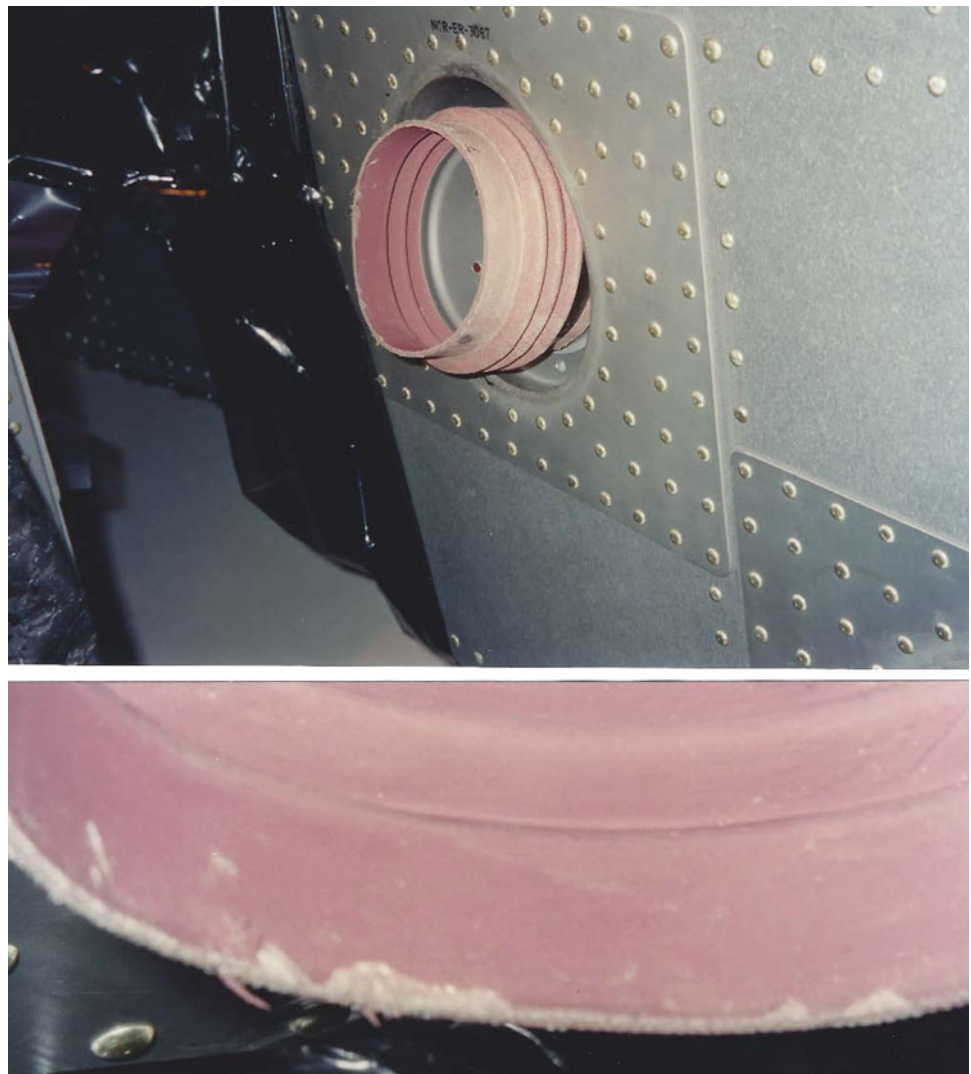


Fig. 8.50 It is probable that these flight harness materials were manufactured 15 years before this final inspection. Damage to the Kapton insulation around a cable attachment point reveals silver-plated copper strands of the shielding. Also, in the cable bundle, the outer layer of the wrapped Kapton has crazed and become embrittled, with some very small flakes being shed. Wires from the same batch/spools kept for the same period in a controlled store showed no degradation. The ISS baseline for wire insulation is Teflon-coated Kapton, which seems less susceptible to handling damage than bare Kapton

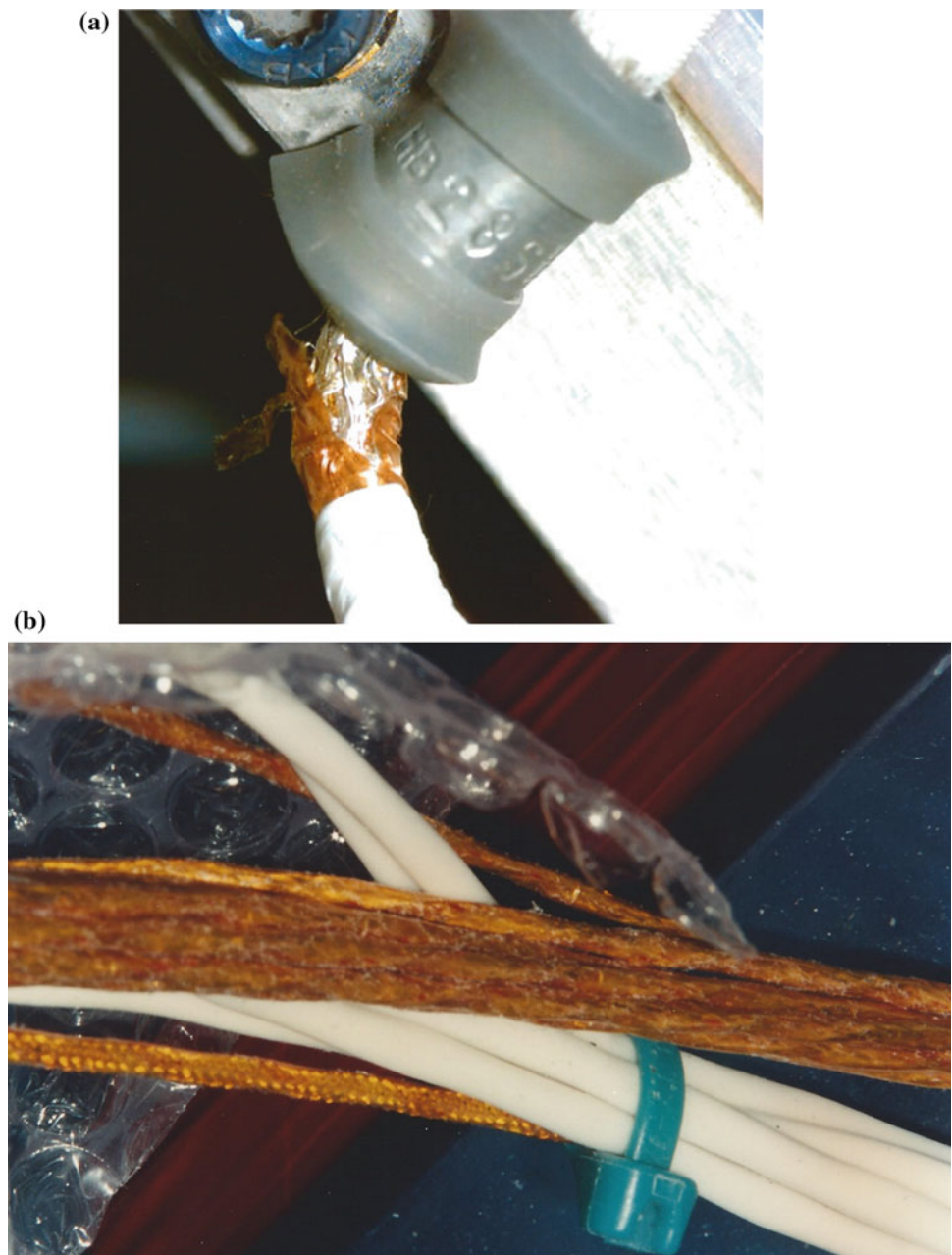
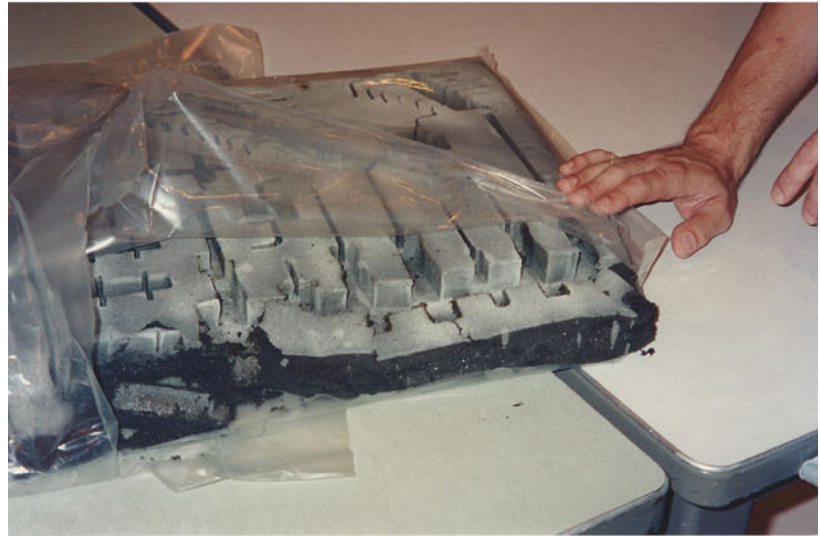
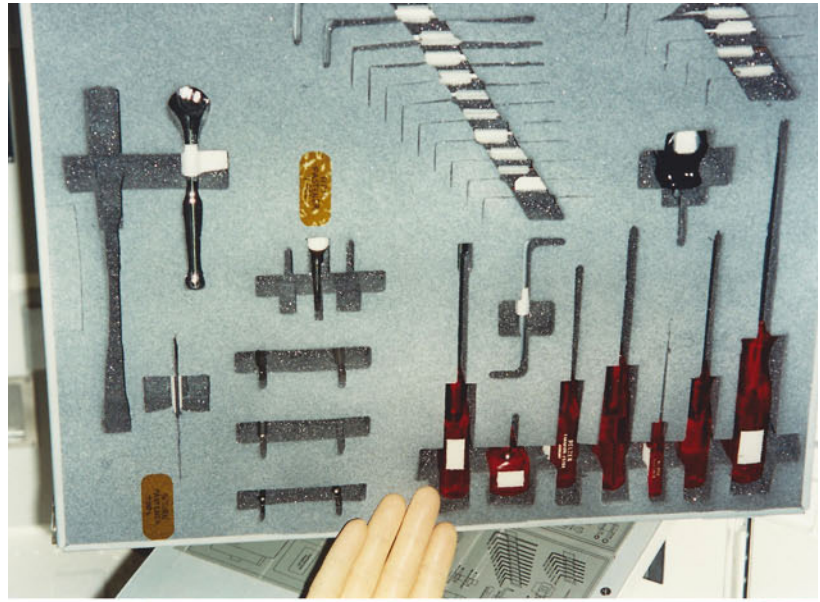


Fig. 8.51 Several wire bundles containing spliced wire joints made with Solder Sleeves. These wire interconnections would not be permitted for vacuum applications due to the entrapped solder flux and its residues (seen as a *yellow-brown* layer beneath the sleeving)



Fig. 8.52 *Top photograph* show a new on-board tool holder made from Solamide 301 foam for the ISS. It is expected to have a longer life than the Pyrel foam seen for the Spacelab tool holder. After 6 years of use the Pyrel has completely degraded. When compressed by slight handling during this inspection, it pulverises to the powder seen in the lower photograph. Pyrel foam (non-flammable, no off-gassing and non-toxic) was used for sound insulation and packaging in toolboxes, work boxes and Spacelab drawers



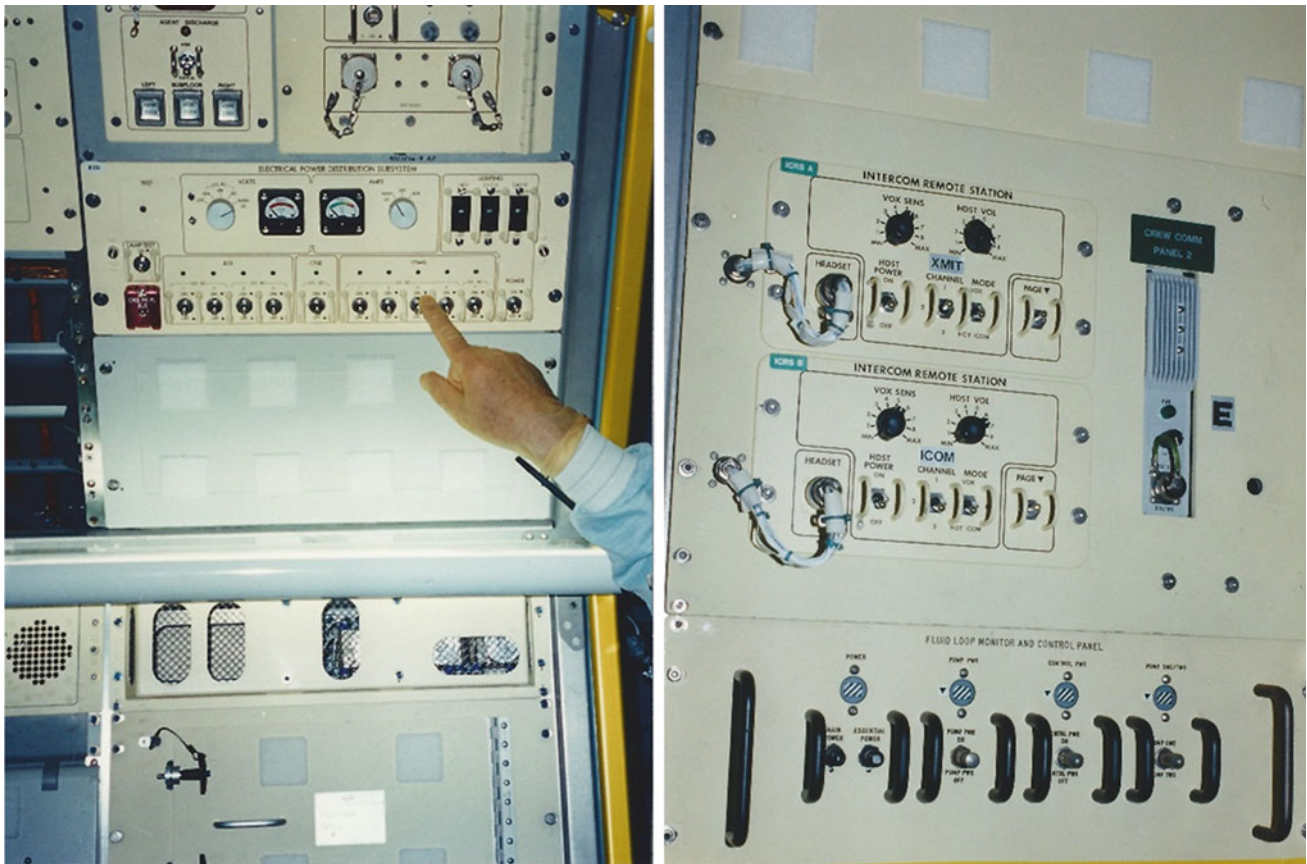


Fig. 8.53 The switches in the left photograph are inadequately protected against accidental contact by an astronaut working under micro-gravity conditions (see also Fig. 3.1). Covers are necessary, on the right-hand rack location protection is given by *bars* that protrude above the switches themselves

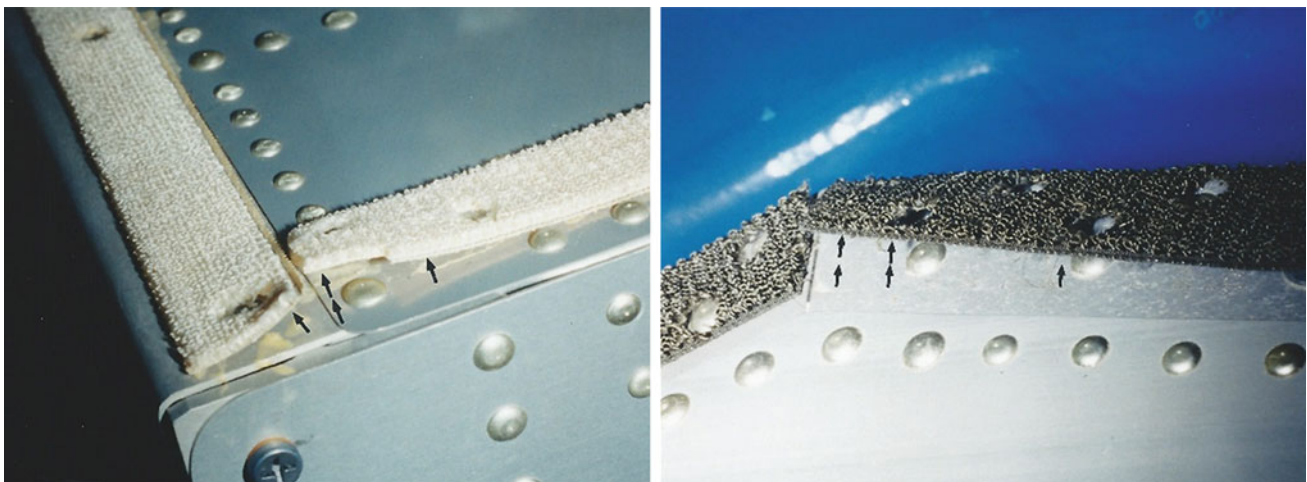
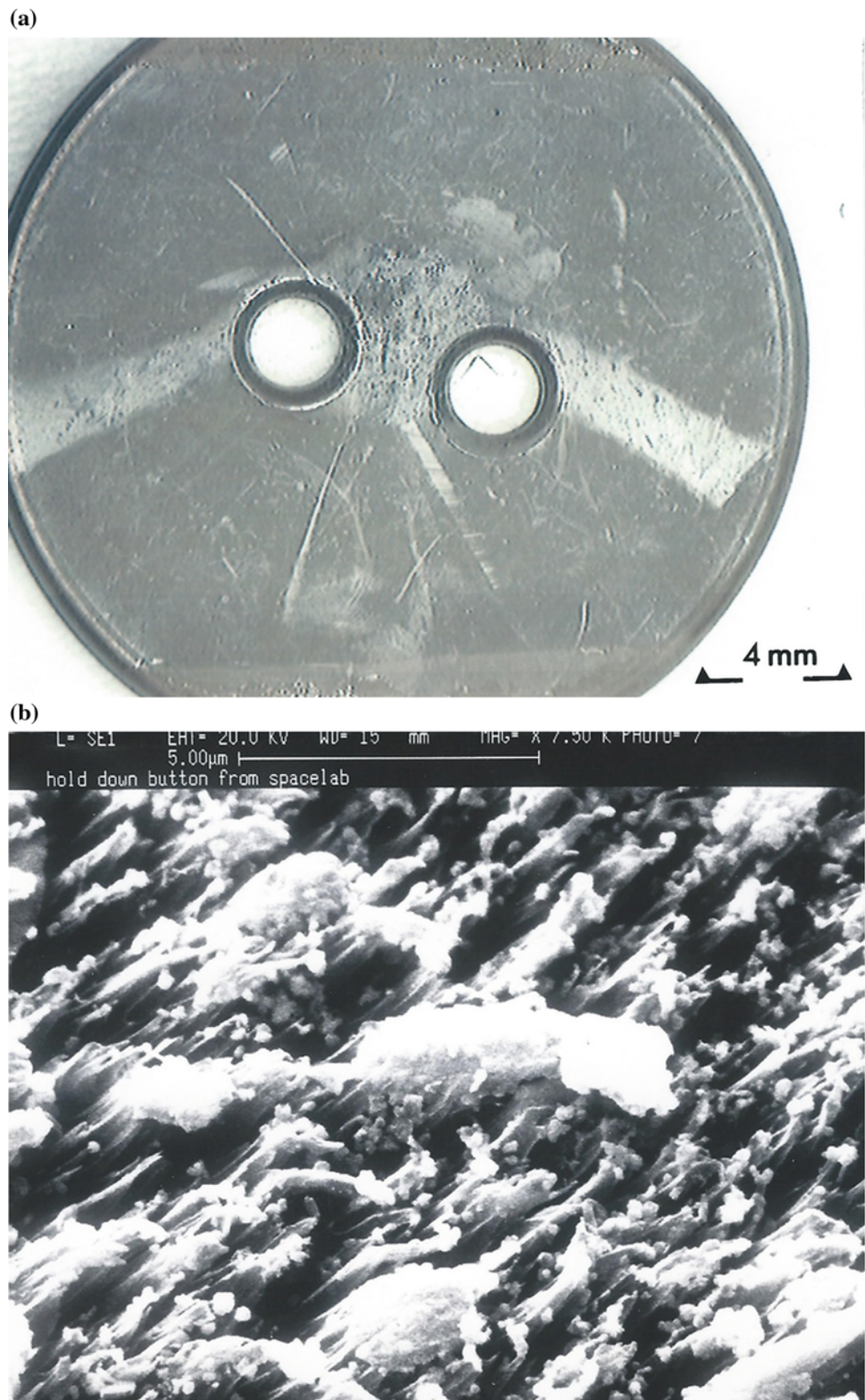


Fig. 8.54 General views of de-bonded Velcro tape. These defects were frequently seen. They result from an inadequate amount of adhesive—a continuous film might be preferable

Fig. 8.55 **a** This post-flight hold-down button for the external multilayer insulation is severely attacked by atomic oxygen, the white bands show location of lacing tape (masking the button's surface). **b** SEM image at $\times 7500$ showing the typical cone-shaped features of ATOX attack on a polymer, some inorganic additives are left as white non-conducting residues on the surface



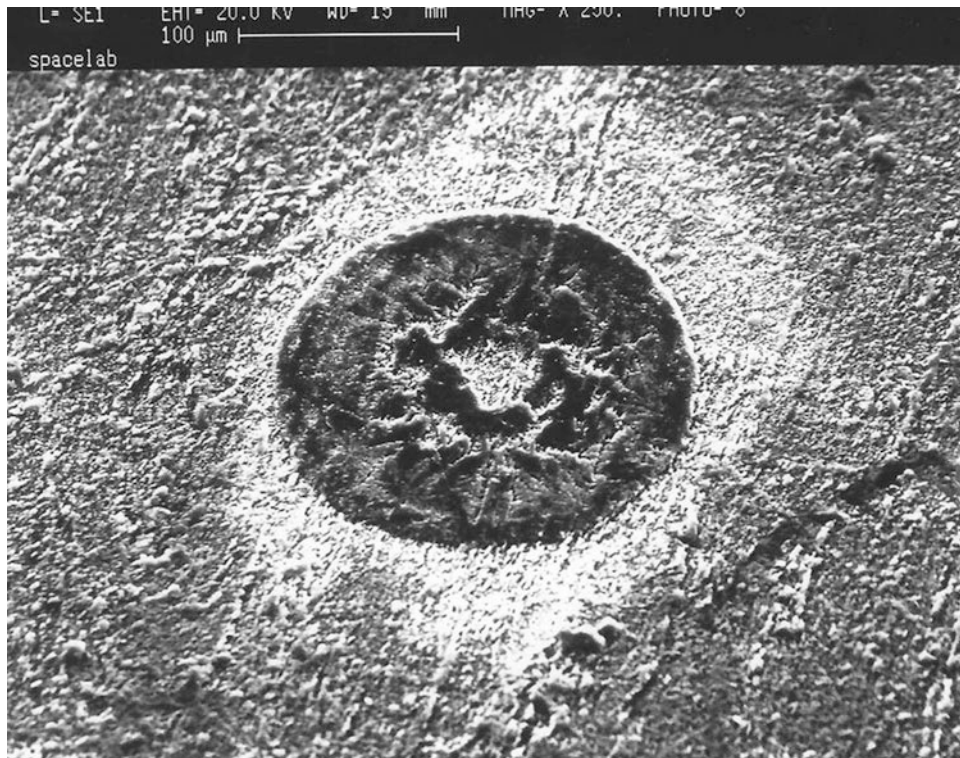


Fig. 8.56 Another hold down button from Spacelab; here a micrometeoroid hit is displayed. This remarkably small impact crater has a diameter of about 180 μm